

Copyright

by

Michelle A. Parsley

1998

Push-Out Behavior of Concrete-Filled Steel Tubes

by

Michelle Ann Parsley, B.S.

Thesis

Presented to the Faculty of the Graduate School

of The University of Texas at Austin

in Partial Fulfillment

of the Requirements

for the Degree of

Master of Science in Engineering

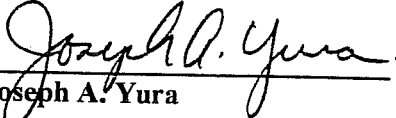
The University of Texas at Austin

August 1998


Push-Out Behavior of Concrete-Filled Steel Tubes

APPROVED BY

SUPERVISING COMMITTEE:



Joseph A. Yura



James O. Jirsa

ACKNOWLEDGMENTS

The experimental portion of the research on concrete-filled steel tubes was conducted at the Phil M. Ferguson Structural Engineering Laboratory of The University of Texas at Austin. This research was part of the U.S. – Japan Cooperative Earthquake Research Program, Phase 5 – Composite and Hybrid Structures, and was sponsored by the National Science Foundation.

Without the help of Dr. Joseph A. Yura and Dr. James O. Jirsa, this thesis would not exist. I express special thanks to Dr. Yura for his guidance and insight, and to Dr. Jirsa for numerous suggestions to improve the clarity of this text.

I am indebted to the students of Ferguson Laboratory who assisted with this research. In particular, I thank Heather Jobson, Chris Gilchrist, Reagan Herman, Zach Kates, Brian Chen, Bo Jaquess, Pete Schönwetter, and Brad Koester for their contributions to the construction of the concrete-filled tubes. I also wish to thank Bo Jaquess, Robbie Barnes, and Brad Koester for assistance in performing materials tests. Finally, the instrumentation and testing of the experimental specimens were carried out with the help of Pete Schönwetter and Brad Koester, to whom I am grateful.

I wish to thank the staff of Ferguson Laboratory for their contributions to this project. I appreciate the efforts of Mike Bell in welding the shear tab connections, and I thank Wayne Fontenot for machining various fixtures used in the testing of the concrete-filled tubes. Laurie Golding is especially appreciated for her coordination of purchase orders.

I express special thanks to visiting scholars Kazuhiro Uchida and Hiroshi Noguchi, who spent several months at Ferguson Laboratory as part of the U.S. – Japan Cooperative Research Program. They provided beneficial suggestions and information, and contributed several photographs of the construction of the specimens included in this thesis.

Since 1995, my graduate studies have been supported by the James and Marie McNeil Endowed Graduate Fellowship in Engineering and the National Defense Science and Engineering Graduate Fellowship. I am grateful to Dr. and Mrs. McNeil and to the U.S. Department of Defense for this assistance.

I wish to express special thanks to my family and friends, whose support and encouragement allowed me to complete this research.

August 10, 1998

Push-Out Behavior of Concrete-Filled Steel Tubes

by

Michelle Ann Parsley, M.S.E.

The University of Texas at Austin, 1998

Supervisor: Joseph A. Yura

This thesis presents the results of a series of push-out tests of rectangular concrete-filled steel tubes (CFT's) performed at the Ferguson Structural Engineering Laboratory of the University of Texas at Austin. These CFT push-out tests were conducted to study the mechanisms of shear transfer along the steel-concrete interface, including adhesion, friction, and wedging of the concrete core. The parameters investigated were the wall stiffnesses of the steel tubes and the effect of loading the steel tube through shear tab connections. The behavior of the shear-tab specimens is compared to that of tubes supported evenly on their bases. A model for the shear transfer mechanism in CFT's is developed based on the experimentally-determined peak and effective bond stresses, the load-slip behavior of the concrete core, and the distribution of longitudinal shearing stresses along the length of the interface. Finally, a design example is presented which incorporates the results of this test series.

CONTENTS

CHAPTER 1: INTRODUCTION	1
INTRODUCTION TO CONCRETE FILLED TUBE (CFT) CONSTRUCTION	1
ADVANTAGES OFFERED BY CFT COLUMNS	2
RESEARCH NEEDS INVOLVING CFT COLUMNS	3
PREVIOUS RELATED RESEARCH	4
SELECTION OF EXPERIMENTAL VARIABLES	5
VARIABLES NOT CONSIDERED IN THESE EXPERIMENTS	6
SELECTION OF EXPERIMENTAL DESIGN	7
ORGANIZATION OF MANUSCRIPT	8
CHAPTER 2: TEST METHODS	9
DESCRIPTION OF TEST SERIES	9
<i>CFT's Without Shear Tabs</i>	9
<i>CFT's With Shear Tabs</i>	10
CONSTRUCTION OF SPECIMENS	14
<i>Materials Used</i>	14
<i>Construction Technique</i>	19
INSTRUMENTATION OF SPECIMENS	26
<i>Displacement Measurements</i>	27
<i>Strain Measurements</i>	28
VALIDITY AND RELIABILITY OF THE MEASUREMENTS	29
<i>Strains Inside the Concrete Core</i>	29
<i>Strains on the Surface of the Steel Tube</i>	30
<i>Displacement of the Concrete Core</i>	33
TEST SETUP AND PROCEDURE	35

CHAPTER 3: EVALUATION OF TEST DATA	37
DETERMINATION OF STRESSES FROM STRAIN DATA	37
EFFECT OF CONFINEMENT OF CONCRETE	37
SELECTION OF E_c USED IN THE ANALYSIS OF TEST DATA	39
VALIDATION OF THE CONSTITUTIVE RELATIONSHIPS USED IN THE ANALYSIS OF DATA	44
CHAPTER 4: EXPERIMENTAL RESULTS	47
EXPERIMENTAL BEHAVIOR OF 8-IN. CFT'S WITHOUT SHEAR TABS	47
<i>Load - Slip Response</i>	<i>47</i>
<i>Distribution of Longitudinal Shearing Stresses</i>	<i>50</i>
<i>Distribution of Bond Slip</i>	<i>55</i>
EXPERIMENTAL BEHAVIOR OF 8-IN. CFT'S WITH SHEAR TABS	59
<i>Load - Slip Response</i>	<i>59</i>
<i>Distribution of Longitudinal Shearing Stresses</i>	<i>60</i>
<i>Distribution of Bond Slip</i>	<i>65</i>
<i>Photographic Evidence of Shear Tab Deformation</i>	<i>67</i>
EXPERIMENTAL BEHAVIOR OF 10-IN. CFT'S WITHOUT SHEAR TABS	69
<i>Load - Slip Response</i>	<i>69</i>
<i>Distribution of Longitudinal Shearing Stresses</i>	<i>70</i>
<i>Distribution of Bond Slip</i>	<i>74</i>
EXPERIMENTAL BEHAVIOR OF 10-IN. CFT'S WITH SHEAR TABS	77
<i>Load - Slip Response</i>	<i>77</i>
<i>Distribution of Longitudinal Shearing Stresses</i>	<i>78</i>
<i>Distribution of Bond Slip</i>	<i>84</i>
<i>Photographic Evidence of Shear Tab Deformation</i>	<i>87</i>

CHAPTER 5: INTERPRETATION OF RESULTS	88
INTERPRETATION OF 8-IN. CFT'S WITHOUT SHEAR TABS	88
INTERPRETATION OF 8-IN. CFT'S WITH SHEAR TABS	91
INTERPRETATION OF 10-IN. CFT'S WITHOUT SHEAR TABS	92
INTERPRETATION OF 10-IN. CFT'S WITH SHEAR TABS	93
COMPARISON OF BOND STRENGTHS	94
COMPARISON OF INITIAL AND RELOADING STIFFNESSES	97
RELATION TO OTHERS' RESEARCH RESULTS	99
<i>Load – Slip Behavior</i>	99
<i>Bond Strengths</i>	100
CHAPTER 6: A MODEL FOR THE SHEAR TRANSFER MECHANISM	101
ADHESION	101
<i>Definitions Accepted by Previous Researchers</i>	101
<i>Application to Current Research Results</i>	101
FRICTION	102
<i>Definitions Accepted by Previous Researchers</i>	102
<i>Application to Current Research Results</i>	102
WEDGING OF THE CONCRETE CORE	103
<i>Definitions Accepted by Previous Researchers</i>	103
<i>Application to Current Research Results</i>	103
MODEL FOR SHEAR TRANSFER IN CFT'S	104
<i>Shear Transfer in CFT Push-Out Tests</i>	104
<i>Effect of Shear Tabs on Shear Transfer</i>	105
<i>Effect of Wall Stiffness on Shear Transfer</i>	105
APPLICATION OF THE MODEL TO CFT COLUMN DESIGN	106
<i>Effect of Shear Tabs on Bond Strength</i>	106
<i>Effect of Wall Stiffness on Bond Strength</i>	106
<i>Design Bond Strength and Associated Strength Reduction Factor</i>	114
DESIGN EXAMPLE	115

CHAPTER 7: SUMMARY AND CONCLUSIONS	117
RESEARCH APPROACH	117
BOND STRENGTH	118
LOAD - SLIP BEHAVIOR	118
DISTRIBUTION OF LONGITUDINAL SHEARING STRESSES	119
SHEAR TRANSFER MECHANISMS	120
MODEL FOR SHEAR TRANSFER IN CFT PUSH-OUT SPECIMENS	120
APPLICATION TO CFT COLUMN DESIGN	121
RECOMMENDATIONS FOR FUTURE RESEARCH	121
APPENDIX	123
BIBLIOGRAPHY	144
VITA	146

CHAPTER 1

INTRODUCTION

INTRODUCTION TO CONCRETE-FILLED TUBE (CFT) CONSTRUCTION

An important innovation of the past thirty years in the structural design of buildings has been the use of composite columns. Composite construction is defined herein as the combination of structural steel and structural concrete in an individual element, which interact to resist the loads imposed on the element. The interaction of steel and concrete in a composite member generally results in a more efficient, and thereby cost-effective, system for resisting the applied loads. One type of composite compression member that has gained popularity in recent years is the filled composite column.

The filled composite column is also known as the concrete-filled steel tube (CFT). The steel encasement of a CFT is typically a pipe or a hollow section fabricated from a steel plate that is folded into shape and welded. The infilled concrete may have normal to high strength characteristics.

Designs of moment-resisting connections of steel girders to a CFT column have not been standardized. Various details have been considered in the design of these connections to enhance the transfer of load from the girders to the column. These include direct welding of the girders to the surface of the steel tube, plate diaphragms welded inside the steel tube, and studs welded to the inside surface of the steel tube. Research in the area of moment-resisting connections to CFT columns is ongoing.

In contrast, many of the designs of shear connections in CFT construction are adaptations of standard bolted and welded connections in simple frame (non-moment-resisting) steel construction. For example, a common shear connection is the shear tab, which consists of a steel plate that is shop welded to the column along one edge and bolted in the field to the web of the beam. The primary use of a shear tab is to transfer a

reaction from the framed beam to the column. Figure 1.1 shows a typical shear tab connection.

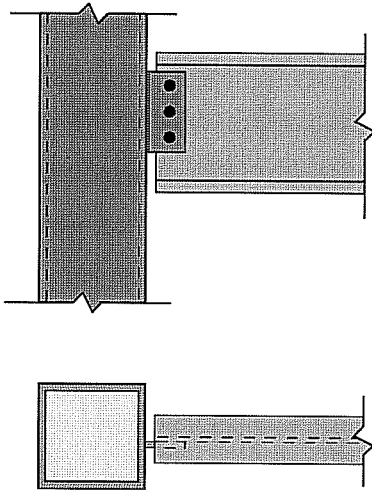


Figure 1.1. A typical shear tab connection to a CFT column.

ADVANTAGES OFFERED BY CFT COLUMNS

CFT columns are structurally efficient for several reasons. From a fabrication perspective, the hollow steel tubes provide the formwork for the concrete core, so no additional costs for formwork are incurred. Furthermore, infilling the concrete is simple to perform, and much of the fabrication can be standardized and carried out in the shop. In addition, compared to reinforced concrete columns, CFT columns simplify construction since the need for longitudinal and transverse reinforcement is eliminated.

Another advantage of CFT columns is the transverse confinement provided by the steel shell for the concrete core. It is well known that concrete under a triaxial state of stress experiences an increase in strain capacity and strength. In a round CFT, the concrete is completely confined and is able to sustain increased stresses and strains. However, there is some debate as to whether the increased strength offered by confinement applies to rectangular filled composite columns. This issue is discussed in more detail in Chapter 3.

Infilling a hollow tube with concrete also results in increased stability. First, the flexural stiffness added by the concrete core increases the buckling capacity of the column under axial loads relative to a hollow steel tube. Additionally, the concrete core provides increased stability against local buckling of the steel tube since it forces all buckling modes outward.

Other advantages offered by CFT columns include increased fire resistance of the steel and improved aesthetics because of the more slender columns permitted in CFT construction. The interested reader is referred to the following sources for further discussion of the advantages provided by CFT columns: Viest et. al. (1997), Iyengar (1977), Furlong (1967), Gardner and Jacobson (1967), Zhong and Maio (1988), and Cai (1988).

RESEARCH NEEDS INVOLVING CFT COLUMNS

In recent years, composite and hybrid structures have received more attention in the United States and Japan following the poor performance of steel frames in the Northridge and Kobe earthquakes. A cooperative research effort has been undertaken to develop standardized design procedures and codes for these structures. In particular, Phase 5 of the U.S.-Japan Cooperative Earthquake Research Program is focused on a joint research program involving composite and hybrid structures. The document edited by Goel and Yamanouchi (1993) presents the results of a Joint Planning Workshop held in September of 1992.

Some of the unanswered questions in CFT construction that are discussed in Goel and Yamanouchi (1993) focus on the interface between the infilled concrete and the steel tube. Specifically, the report expresses the need for research to define the bond stress that can be achieved between the steel and the concrete. A related research recommendation in the report suggests investigating the basic mechanisms used by CFT columns to transfer shear forces from the steel tube to the concrete. Conversations with U.S. designers also have indicated the importance of understanding load transfer mechanisms from steel to concrete in the design of beam-column connections.

Ultimately, models are needed that will predict the behavior and strength of CFT columns, including the beam-column connections, under a variety of loading conditions.

In this study, the shear transfer mechanism between the infilled concrete and steel hollow tubes is examined. To that end, eight push-out tests were conducted on rectangular CFT columns.

PREVIOUS RELATED RESEARCH

In developing a model of the shear transfer mechanism in CFT columns, the results of this study are compared with the results of earlier investigations into the bond between steel and concrete. Studies of the bond between concrete and steel have been conducted in the areas of pullout tests on steel reinforcing bars embedded in concrete, push-off tests between flat plates and cast-in-place concrete, and push-out tests of concrete-filled tubes.

Pullout tests on plain reinforcing bars embedded in concrete were thoroughly researched about fifty years ago. In these tests, the bar was pulled out from a concrete cylinder or prism while the concrete was restrained by a reaction pressure. Because the concrete was in compression and the steel bar was in tension, differential strains along the interface resulted in the bar's slipping or "pulling out" of the concrete. Mains (1951) conducted pullout tests on many specimens, including plain reinforcing bars. The maximum bond stresses achieved on the steel-concrete interface and the distribution of bond stresses along the bar were studied.

In 1985, Rabbat and Russell conducted experiments on the steel-concrete interface. They performed several push-off tests between rolled steel plate and cast-in-place concrete. An in-plane shear force was applied between the concrete and the steel to determine the coefficient of static friction between the two materials. In these push-off tests, the investigators measured maximum and effective bond stresses and relative bond slip between the steel and the concrete.

Other investigators have conducted push-out tests on CFT's. In 1980, Virdi and Dowling measured the bond strength at the interface between concrete and circular seamless steel tubes. Similarly, Shakir-Khalil (1993a) presents results of investigations

into the bond strength between the concrete core and the steel tube in CFT's. In this publication, results are reported on push-out tests of rectangular and circular CFT's having interface lengths of 200 mm (7.9 in.), 400 mm (15.7 in.), and 600 mm (23.6 in.). A separate publication by the same author (Shakir-Khalil 1993b) also includes results on push-out tests of rectangular and circular CFT's with a 400-mm (15.7-in.) interface. In general, previous research involving push-out tests of CFT's has been more commonly conducted on circular sections than rectangular, and only short columns have been studied.

SELECTION OF EXPERIMENTAL VARIABLES

The results of previous investigations on bond were applied to the selection of experimental variables in the current series of push-out tests. In 1988, Lamport conducted tests to determine the ultimate axial strength of grouted pile-to-sleeve connections of steel jacket platforms, which will be occasionally referred to throughout this manuscript as "grouted connections." The variables he identified as important in determining the ultimate capacity of these connections include the tube and grout geometries. In a similar investigation of the strength of grouted connections, Billington and Lewis (1978) report that "[u]ltimate strength is shown to depend on the geometry of the connection. . . . Tests on plain pipes indicate that the reduction in radial stiffness which accompanies increases in pile diameter can lead to unacceptable reductions in ultimate strength." Just as radial stiffness, expressed as the ratio of tube thickness to diameter of the section (t/d), influences the strength of grouted connections, wall stiffness (t/b) likely influences the strength of the steel-concrete interface in CFT's. Shakir-Khalil (1993a) suggests that a smaller CFT section would provide increased resistance to slip of the infilled concrete in a push-out test because of the stiffer walls. Thus, to determine the effect of wall stiffness on the push-out behavior of rectangular CFT's, it was included as a variable in this experiment. Wall stiffness will be accounted for in this series of tests by varying the width of the specimen (b), while maintaining a constant thickness of the steel tube (t).

The second variable chosen for this experiment was the method of applying the axial force to the steel tube during the push-out test. Load was applied to the steel tube through shear tabs welded to the outer surface of the tube to simulate conditions present in the common shear tab connection of a beam to a CFT column. In contrast to the specimens loaded through shear tabs, the remaining specimens in this test series were tested by resting the steel tube on its base, thereby applying the axial force to the entire steel cross-section. Similar tests on specimens loaded through brackets were attempted by Shakir-Khalil (1993b), but in those experiments some of the specimens experienced failure of the brackets instead of the steel-concrete interface. Loading of the steel tube through shear tabs was expected to increase the capacity of the steel-concrete interface because of deformations imposed on the steel tube as the flexible connections rotate during testing.

VARIABLES NOT CONSIDERED IN THESE EXPERIMENTS

To limit the scope of these tests, certain experimental variables were not considered. For example, the properties of the concrete were not varied from specimen to specimen to reduce the influence of concrete strength and concrete shrinkage on the results. It is well known that concrete gains strength with age. However, the rate of gain decreases over time and is significantly less after the cured concrete has reached an age of 28 days. By conducting the experiments several months after casting of the infilled concrete, the concrete strength did not change appreciably between tests. Thus, the influence of concrete strength on the results was reduced. Furthermore, previous research indicated that bond strength in CFT's is not affected to any measurable extent by the concrete strength (Virdi and Dowling 1980).

Shrinkage of the concrete is a major concern in reinforced concrete construction, but its effects on CFT construction have not been confirmed. In tests of grouted pile-to-sleeve connections, Billington and Lewis (1978) report a 42% reduction in bond strength attributable to the shrinkage that occurred in their specimens over a 28-day period. On the other hand, Hajjar and Gourley (1996) suggest that shrinkage "has a smaller influence on the behavior of CFT's" than in reinforced concrete construction and may be neglected

in CFT's. Therefore, in this series of tests, the effects of shrinkage will not be considered as an experimental variable. Although some shrinkage is likely to occur at the ends of the specimens, testing of the CFT's at nearly the same age will result in consistent amounts of shrinkage, thereby reducing the dependency of the results on shrinkage.

Another variable not included in this study is the length-to-width ratio of the steel tubes (l/b). Both Lamport (1988) and Billington and Lewis (1978) indicate the importance of the length-to-diameter ratio of grouted connections to the ultimate bond strength of the grout-steel interface. However, to reduce the number of variables in this study, all specimens will have the same (l/b) ratio.

Variations in the surface roughness of the steel have also been shown to contribute to bond strength. Research conducted on grouted connections has shown that the surface condition of steel tubular members was an essential parameter in the ultimate capacity of the connections (Lamport 1988; Billington and Lewis 1978). Similarly, Virdi and Dowling (1980) suggest that for CFT's "the most important factor [in determining bond strength] is the mechanical keying of the concrete core with the irregularities in the steel tube." To reduce the dependency of the results of the current series of tests on surface roughness of the steel shell, all specimens received the same treatment to the inside surface of the steel tube.

SELECTION OF EXPERIMENTAL DESIGN

After the experimental variables were chosen, a design of the experiments was selected which would be most likely to determine a solution to the research problem. For instance, no investigation of the shear transfer mechanism in CFT's would be complete without a measure of the bond strength. Bond strength is directly related to the push-out resistance of CFT's. It provides a basis for the comparison of experimental variables, and may be used to compare the experimental data to the results of others' related research. Furthermore, knowledge of bond strength is necessary to develop design guidelines for CFT construction. Therefore, bond strength was recorded in all push-out tests of the current investigation.

Another characteristic of the shear transfer mechanism in CFT's is the load-slip behavior of the concrete core. The relationship of the applied load to the slip of the infilled concrete can be used to define failure of the bond between the steel and the concrete. An experimental load-slip response can also be compared to results obtained in previous studies involving a steel-concrete interface. For these reasons, the current investigation measured the applied axial load and displacement of the infilled concrete.

Finally, the distribution of longitudinal shearing stresses along the length of the interface was determined. From the distribution of shearing stresses, the proportion of axial load carried by the steel and concrete was found. This information was used to indicate which portion of the steel tube was contributing to the transfer of load from the steel to the concrete, and was necessary to developing a model of the shear transfer mechanism.

ORGANIZATION OF MANUSCRIPT

In the introduction, an investigation of the shear transfer mechanism between the steel tube and the infilled concrete in CFT columns has been defined, and the selection of the experimental variables has been explained. In Chapter 2, the construction, instrumentation, and testing of the CFT specimens are described. In Chapter 3, the accuracy of the test data is evaluated. In Chapter 4, the results of the experiments are presented, and in Chapter 5, the results are interpreted, and the behavior of the CFT specimens is generalized. In Chapter 6, a model of the shear transfer mechanism in CFT's is developed based on these results, and an application to the design of CFT columns is presented. Finally, the investigation is summarized in Chapter 7. The appendix of this manuscript provides a collection of figures that pertain to material discussed in Chapter 3.

CHAPTER 2

TEST METHODS

The construction, instrumentation, and testing procedure of the eight specimens included in the test series are presented in this chapter. The number and types of specimens are described. In addition, the validity and reliability of the proposed instrumentation scheme are discussed.

DESCRIPTION OF TEST SERIES

Eight specimens were tested in this series of push-out tests. Four prototype designs were developed: a square CFT of 8-in. width *without* shear tabs, 10-in. width *without* shear tabs, 8-in. width *with* shear tabs, and 10-in. width *with* shear tabs. Two CFT's were constructed of each of the four designs. Table 2.1 summarizes the design geometric properties of the test specimens.

Table 2.1. Design geometric properties of the test specimens.

Specimen Label	Width of Steel Tube (In.)	Wall Slenderness Ratio of Steel Tube (b/t)	Length of Steel Tube (In.)	Length of Steel-Concrete Interface (In.)	Shear Tabs?
CFT4	8	32	48	47.0	n
CFT3	8	32	48	47.0	n
CFT2	8	32	48	47.0	y
CFT5	8	32	48	47.0	y
CFT7	10	40	60	58.5	n
CFT1	10	40	60	58.5	n
CFT8	10	40	60	60.0	y
CFT6	10	40	60	60.0	y

CFT's Without Shear Tabs

Four of the eight specimens did not have shear tabs welded to the steel tubes, and instead were supported on their bases during testing. These include CFT3 and CFT4,

both of 8-in. widths, in addition to CFT1 and CFT7, both of 10-in. widths. CFT3 and CFT4 were made according to the design illustrated in Figure 2.1, while CFT1 and CFT7 were constructed as shown in Figure 2.2. Both the 8-in. and the 10-in. square tubes had a length-to-width ratio of six, and all tubes had a nominal $\frac{1}{4}$ -in. wall thickness. The main distinguishing variable between the 8-in. and the 10-in. specimens was the width-to-thickness (b/t) ratio of the tubes.

These specimens were designed so that the controlling failure mode would likely be slip of the concrete core along the steel-concrete interface. The other failure modes accounted for in the design of the specimens were crushing of the exposed portion of the concrete core, yielding of the gross area of the steel tube adjacent to the air gap, and local buckling of the steel tube adjacent to the air gap.

CFT's With Shear Tabs

Four of the eight specimens had shear tabs welded to the surface of the steel tube. Two of these shear-tab specimens, CFT2 and CFT5, were constructed from tubes of 8-inch width, as shown in Figure 2.3, and specimens CFT6 and CFT8 were constructed using 10-in. tubes, as shown in Figure 2.4. Again, the variable that distinguished the 8-in. and 10-in. specimens was the (b/t) ratio of the steel tube.

Similar to the previous specimens, the shear-tab specimens were designed so that failure would likely occur in the steel-concrete bond. The shear tabs and the loading fixture shown in Figures 2.3 and 2.4 were designed to safely support the expected bond failure load. The design of the shear tabs was based on the procedure described in Astaneh, Call, and McMullin (1989). The possible failures considered in the design were shear in the bolts, yielding of the gross area of the steel plate, fracture of the net area of the plate, fracture of the welds, and bearing failure of the plate. The "loading fixture" consists of the two WT's and the steel plate that connects them. The loading fixture was designed to preclude bearing failure of the web, yielding of the gross area of the tension member, and fracture of the welds connecting the tension member to the web. In addition, the loading fixture had to provide enough clearance to accommodate the displacements of the concrete core.

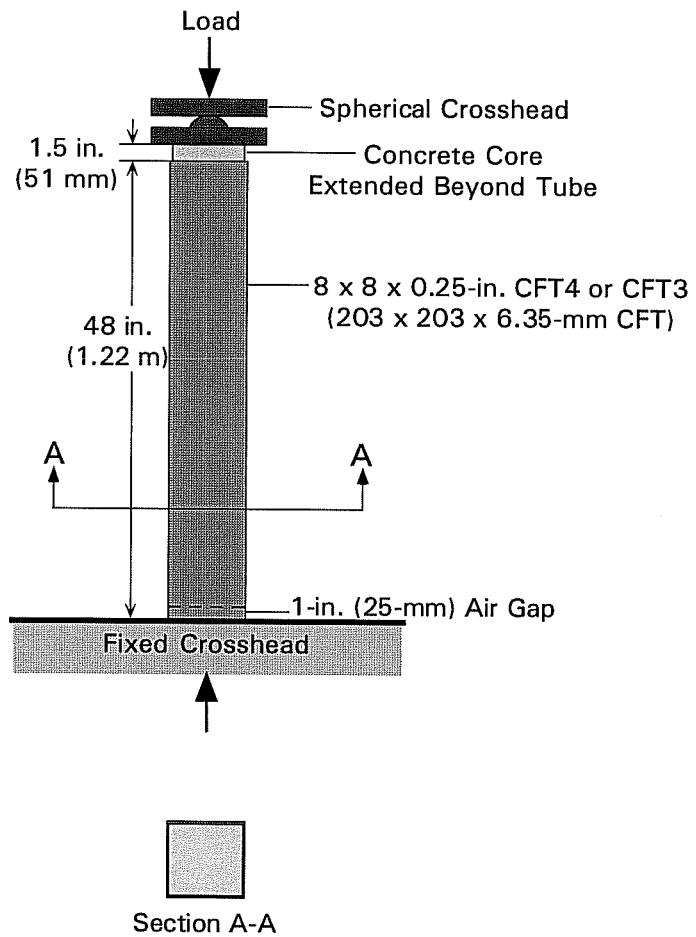


Figure 2.1. Schematic diagram of the 8 x 8 x 1/4-in. CFT *without* shear tabs.

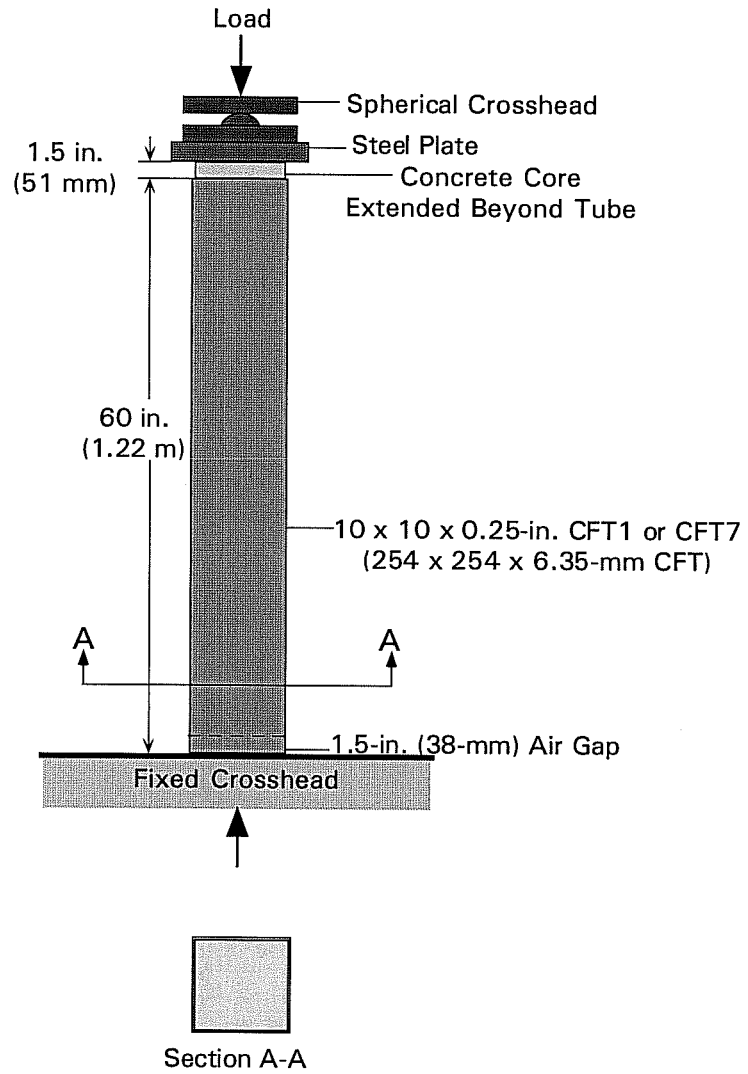


Figure 2.2. Schematic diagram of the 10 x 10 x 1/4-in. CFT *without* shear tabs.

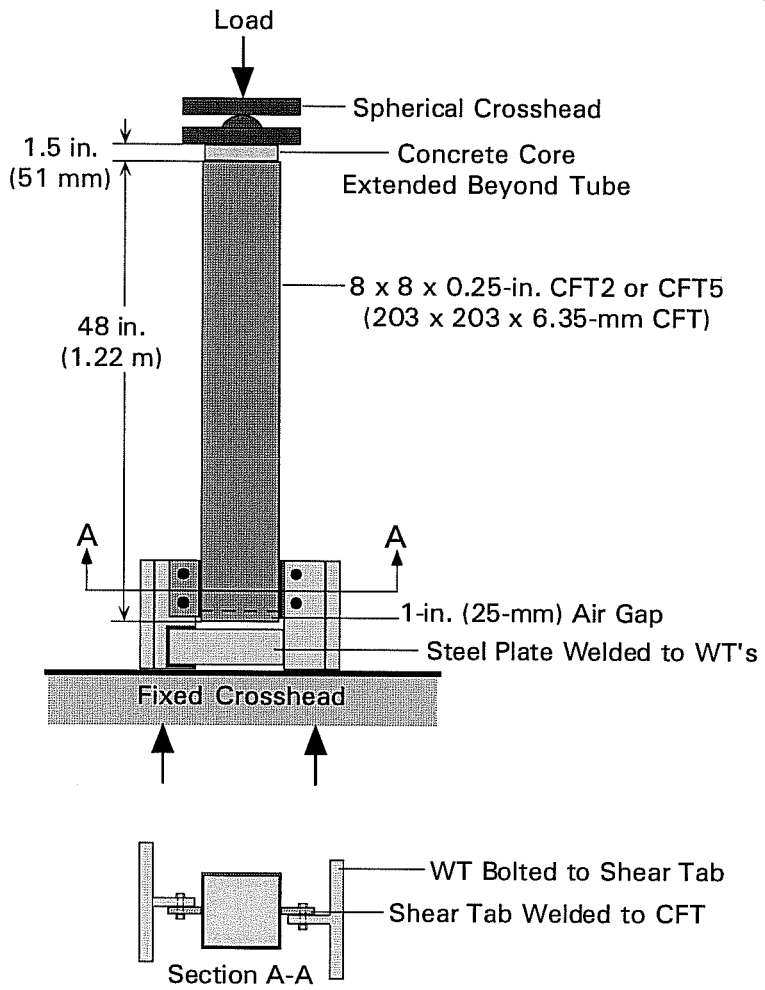


Figure 2.3. Schematic diagram of the 8 x 8 x 1/4-in. CFT *with* shear tabs.

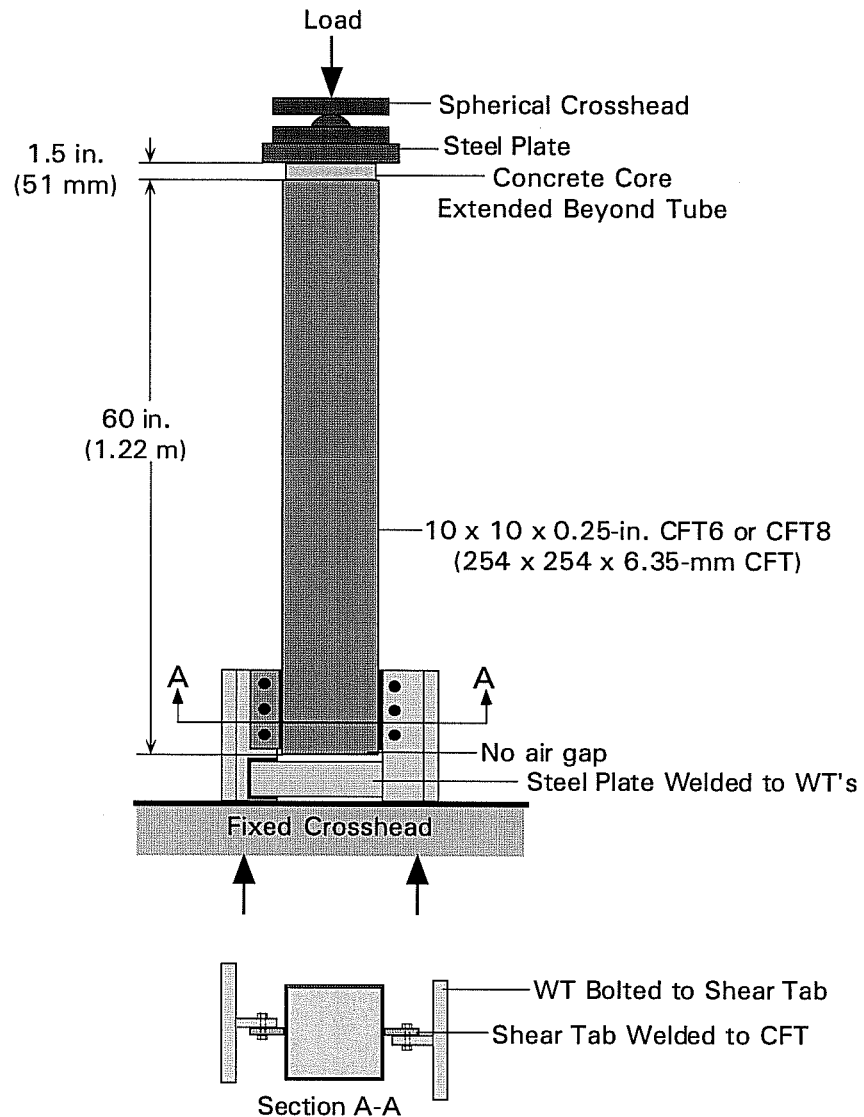


Figure 2.4. Schematic diagram of the 10 x 10 x 1/4-in. CFT *with* shear tabs.

CONSTRUCTION OF SPECIMENS

Materials Used

The steel tubes used in the construction of the four 8-in. CFT's were cut from one 20-ft length of tubing to eliminate variables in material and geometric properties. Similarly, all four 10-in. CFT's were fabricated using steel tubes cut from the same length of tubing. The sections of square tubing specified were TS 8 x 8 x 1/4 and TS 10

x 10 x 1/4. The nominal areas as tabulated in the LRFD Specifications (AISC 1993) are given in Table 2.2.

The average area of each steel tube was determined for comparison with the nominal areas. Before the concrete was cast inside each steel tube, measurements were taken of their lengths, and the weight of each segment of tubing was determined. Since the density of steel is a known, constant value, the weight of each tube divided by the density of steel indicated the average cross-sectional area of the tube. The measured areas, rather than the nominal values, were selected for later use in the data analysis of the CFT's. The calculated areas summarized in Table 2.2 are 91-93% of the nominal values.

Other geometric properties of the specimen were also determined. The wall thicknesses of the steel tubes were measured with a micrometer. As shown in Table 2.3, all of the measured wall thicknesses were less than the nominal values of 0.25 inches. After the infilled concrete had been cast, the depth of the air gap in each specimen was measured in several locations. Mean and median depths are summarized in Table 2.3.

Table 2.2. Cross-sectional areas of the steel tubes.

Specimen	Measured Length of Steel Tube (In.)	Measured Weight of Steel Tube (Lbs.)	Measured Average Cross-Sectional Area of Steel Tube (In.²)	Nominal Area of Steel Tube (In.²)	Measured Area / Nominal Area (%)
CFT4	48.1	93.92	6.89	7.59	91
CFT3	48.1	94.02	6.90	7.59	91
CFT2	48.1	94.20	6.90	7.59	91
CFT5	48.1	94.00	6.90	7.59	91
CFT7	60.0	151.30	8.90	9.59	93
CFT1	60.0	151.26	8.89	9.59	93
CFT8	60.0	150.86	8.87	9.59	92
CFT6	60.0	151.20	8.89	9.59	93

Table 2.3. Other measured geometric properties of the steel tubing.

Specimen	Measured Wall Thickness of Steel Tube, Side A (In.)	Measured Wall Thickness of Steel Tube, Side B (In.)	Measured Wall Thickness of Steel Tube, Side C (In.)	Measured Wall Thickness of Steel Tube, Side D (In.)	Median Depth of Air Gap (In.)	Mean Depth of Air Gap (In.)
CFT4	0.229	0.230	0.227	0.235	1.00	1.03
CFT3	0.228	0.228	0.226	0.229	1.00	0.94
CFT2	0.228	0.229	0.227	0.229	1.19	1.22
CFT5	0.228	0.229	0.227	0.230	1.13	1.09
CFT7	0.234	0.232	0.235	0.232	1.73	1.73
CFT1	0.234	0.234	0.234	0.235	1.50	1.52
CFT8	0.231	0.233	0.232	0.233	0	0
CFT6	0.235	0.234	0.233	0.233	0	0

The specified yield strength of the steel tubing was 46 ksi. Static tension tests of two coupons from the TS 8 x 8 x 1/4 indicated a yield strength of 48 ksi, as determined by the 0.2% offset method. A typical plot of the stress-strain diagrams for this steel tubing is in Figure 2.5. Tension tests of two coupons taken from the TS 10 x 10 x 1/4 tubing gave the average yield strength of this steel as 48 ksi also. Figures 2.6 shows a typical stress-strain curve for a coupon from the 10-in. tubing.

No mechanical connectors were affixed to the inside surface of the steel tubes prior to casting of the concrete. The only surface treatment applied to the steel interface was wire brushing that was necessary to remove any rust.

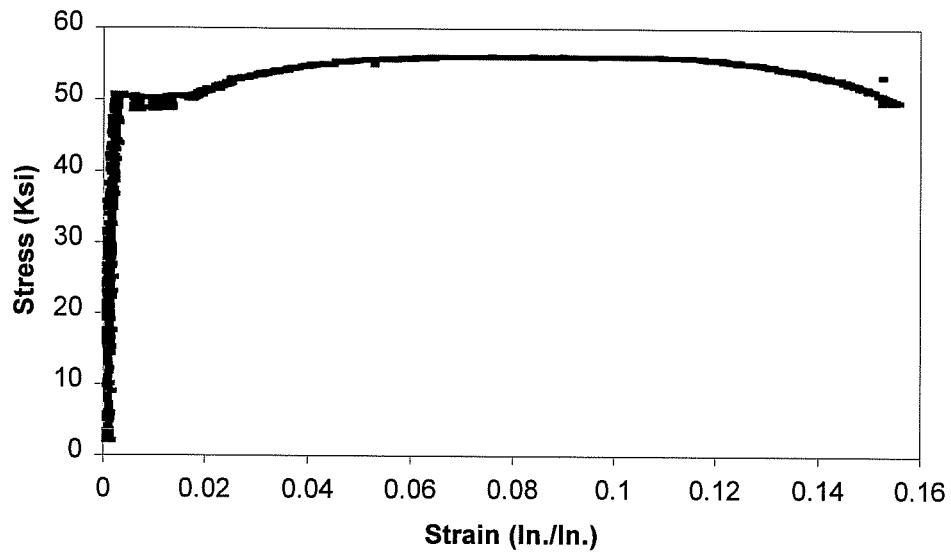


Figure 2.5. Typical stress-strain diagram from the TS 8 x 8 x 1/4.

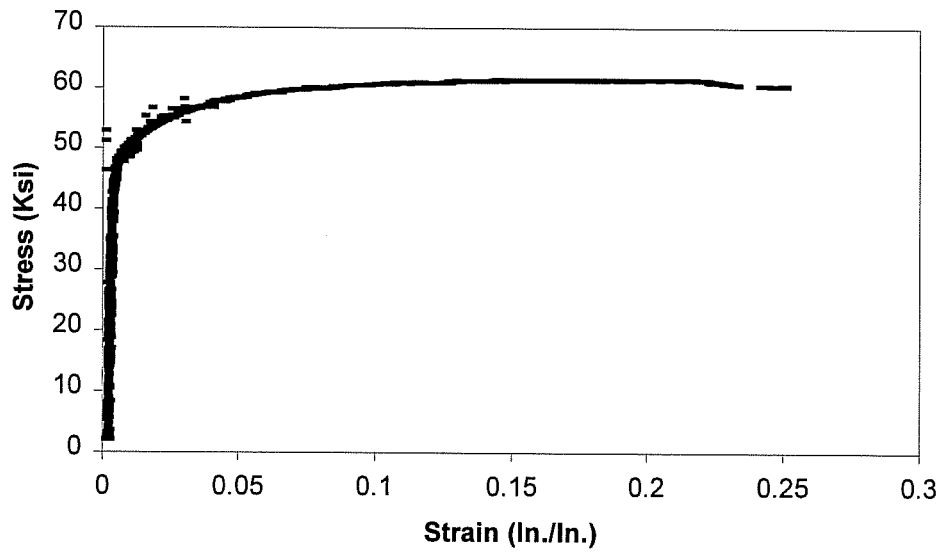


Figure 2.6. Typical stress-strain diagram from the TS 10 x 10 x 1/4.

For consistency, the design compressive strength of the infilled concrete for all specimens was 6000 psi. To simplify the construction process, all CFT's of the same size were cast using the same batch of concrete. The 8-in. CFT's were cast with the first batch of concrete, on February 28, 1997. The 10-in. CFT's were cast on September 4, 1997. In all specimens, the exposed surface of the concrete was covered with a plastic sheet for curing during a minimum of 28 days after casting.

For each batch of concrete, several cylinders were cast and cured under similar conditions. These cylinders were used to determine the compressive strength of the concrete mixes. Figure 2.7 shows the variation of the compressive strength of the concrete cast used in the 8-in. CFT's with age and the age at testing of each specimen. In Figure 2.8, a similar plot shows the compressive strength of the concrete used in the 10-in. specimens. All four 10-in. CFT's were tested around 190 days. At 28 days, the compressive strengths of the concrete were 6550 psi for the 8-in. CFT's and 5860 psi for the 10-in. specimens.

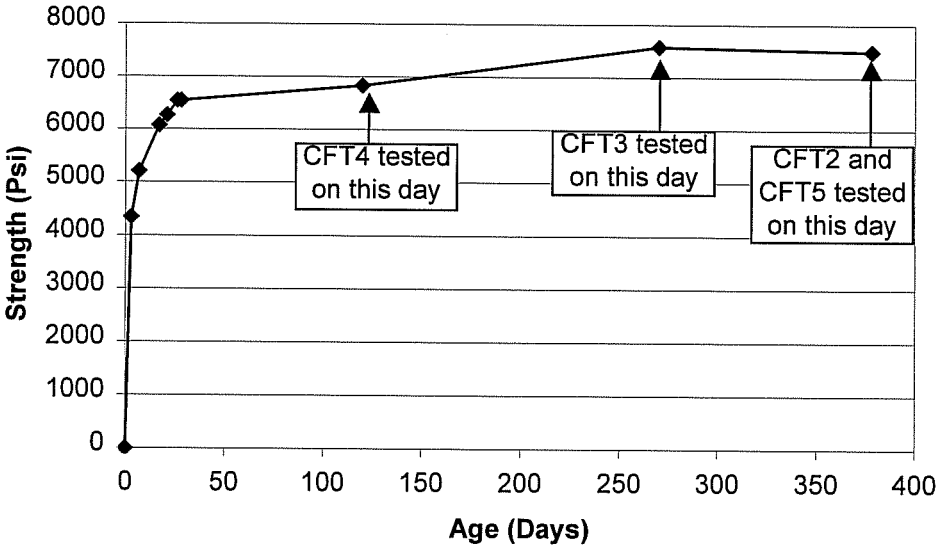


Figure 2.7. Compressive strength of the concrete cast on February 28 and used in the 8 x 8 x 1/4-in. CFT's.

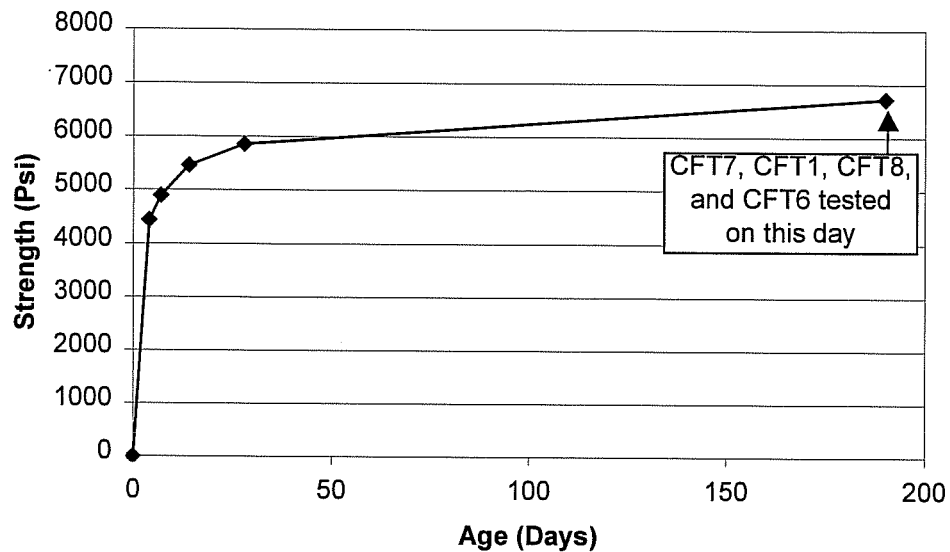


Figure 2.8. Compressive strength of the concrete cast on September 4 and used in the 10 x 10 x ¼-in. CFT’s.

Construction Technique

The construction setup for the CFT columns is shown in Figure 2.9. The setup was designed so that the concrete could be placed into the vertical hollow tube through the open end at the top. The bottom end of the steel tube was enclosed in a wooden form for the portion of the concrete core that extended 1.5 inches beyond the edge of the steel tube. At the upper end of the steel tube, a wooden centering apparatus was used to align a PVC pipe that protected the concrete embedment gages during concrete placement. To maintain the embedment strain gages at their desired locations within the plastic concrete, they were fastened to a long piece of fishing line which was held tautly in place during casting. Two knots along the length of the embedment gage held the gage securely to the fishing line; at opposite ends of the inch-long gage were a square knot and a half-knot. Each embedment gage was fastened to the fishing line at a location determined by the desired center-to-center spacings. Figure 2.10 shows two gages used in a 10-in. CFT specimen that are tied to a piece of fishing line at a spacing of 7.5 inches.

To fasten the line securely to the construction setup, the fishing line was threaded through a small hole in the center of the plywood form at the bottom of the tube, as shown in Figure 2.9. Several knots and then glue were used to ensure that the line would not slip through the hole when a tensile force was applied to it. Additionally, notches were provided in the sides of the formwork to allow the lead wires from the embedment gages to exit the concrete core. Figure 2.11 shows one of the wooden forms with the attached fishing line and embedment gages prior to casting of the infilled concrete.

After a coating of form oil had been applied to the inside surface of the wood formwork, the steel tubes were placed upright atop the forms. An important part of the construction process was protecting the embedment gages while the concrete was being placed and vibrated. The fishing line was threaded through a 1-in. diameter PVC pipe several feet long to encase most of the gages during construction. While the fishing line at one end was securely fastened at the centroid of the formwork, the wooden centering device shown in Figure 2.9 was designed to maintain the location of the protective PVC pipe at the centroid of the section at the opposite end of the tube. The centering device rested firmly atop the hollow tube, and the PVC pipe was threaded through holes in the apparatus slightly larger in diameter than the pipe to minimize the movement of the flexible pipe away from the centroid of the tube section.

After the centering device and PVC pipe had been positioned, casting of the concrete began. As seen in Figure 2.12, shovels were used to place the concrete from the top of the tube in 12-in. lifts. After a lift of concrete had been deposited, an internal vibrator was lowered into the newly-placed layer and immersed for about 30 seconds. Once a layer of concrete had been vibrated, the protective PVC pipe was lifted 12 inches, and the semifluid concrete filled the hole surrounding the fishing line and attached gages. Meanwhile, the free end of the fishing line that extended through the top of the PVC pipe was continuously held taut to keep the gages in place during construction.

The casting of the concrete continued to the level of the desired air gap at the upper edge of the steel tube. The PVC pipe was removed from the centering device, and the fishing line was tied off as shown in Figure 2.13 to keep the line taut during

hardening of the concrete. The exposed end of the tube was then covered with a plastic sheet during curing of the concrete.

An important concern in casting concrete is thorough consolidation of the concrete. Some researchers have indicated difficulties in ensuring that no voids occur when placing concrete in tubes of small diameter (Neogi, Sen, and Chapman 1969). To assess the construction practices used for the CFT's in the current series of tests, the concrete core of one specimen was inspected for voids after testing. One side of a steel tube was cut and removed from a CFT after testing of the specimen. As shown in Figure 2.14, few voids are visible in the concrete.

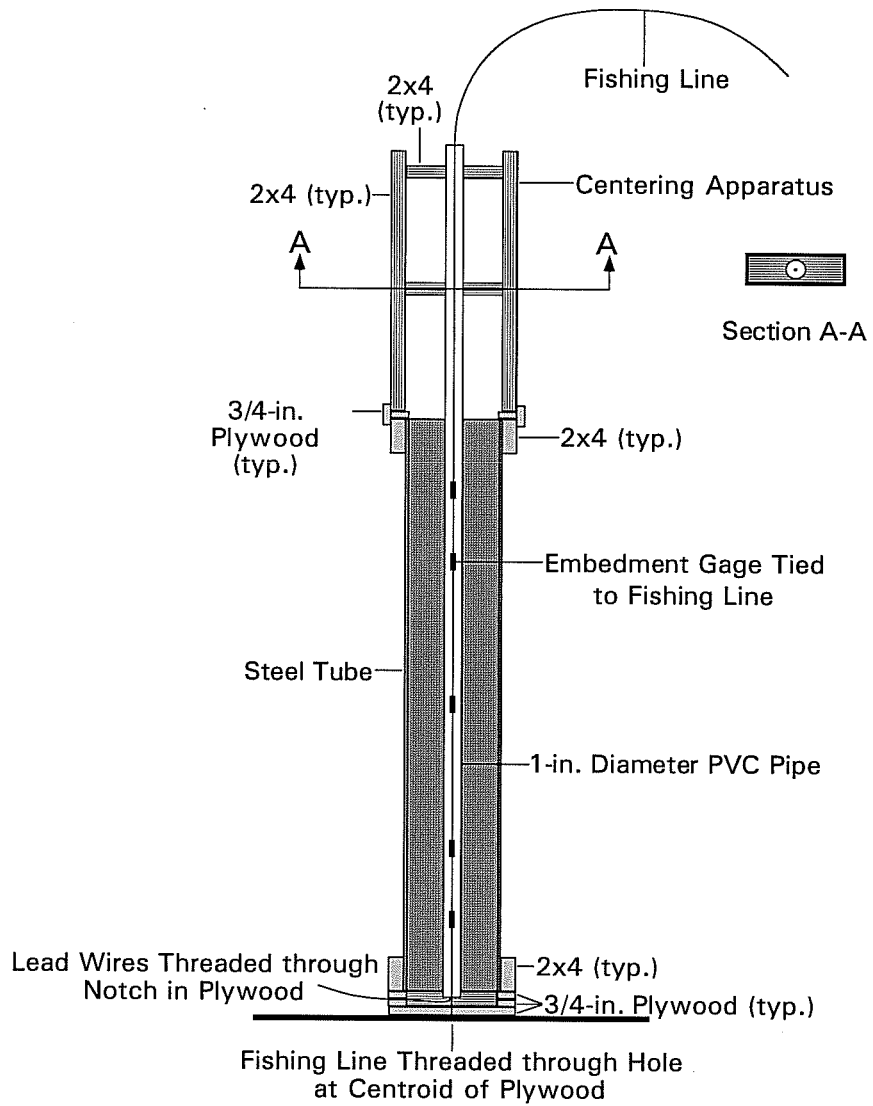


Figure 2.9. Elevation view of a CFT column during construction.



Figure 2.10. Two embedment gages tied in place to a fishing line.

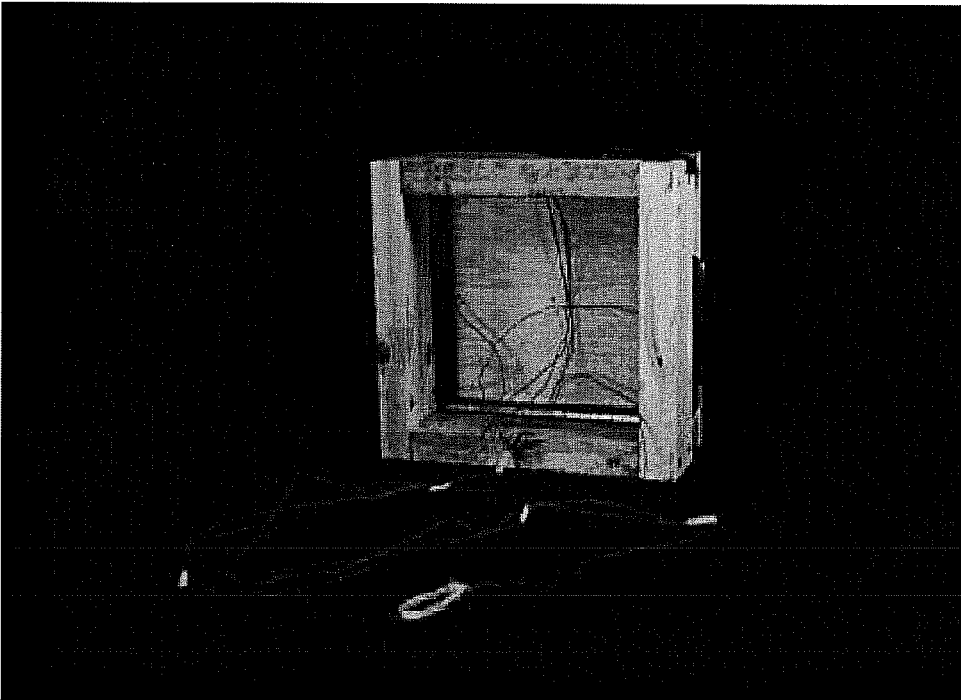


Figure 2.11. The formwork for the extended portion of the concrete core with the attached fishing line and embedment gages.

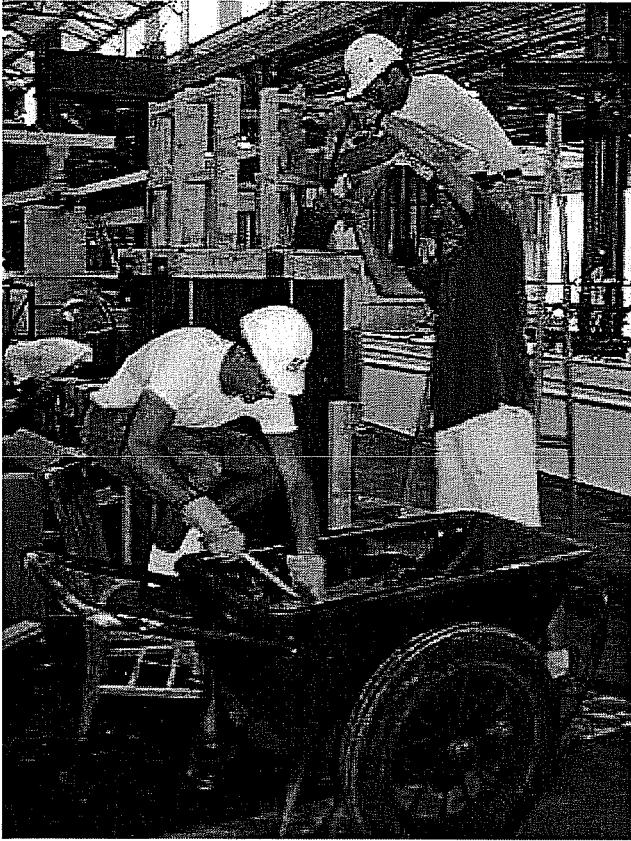


Figure 2.12. Depositing the concrete inside the hollow steel tubes.

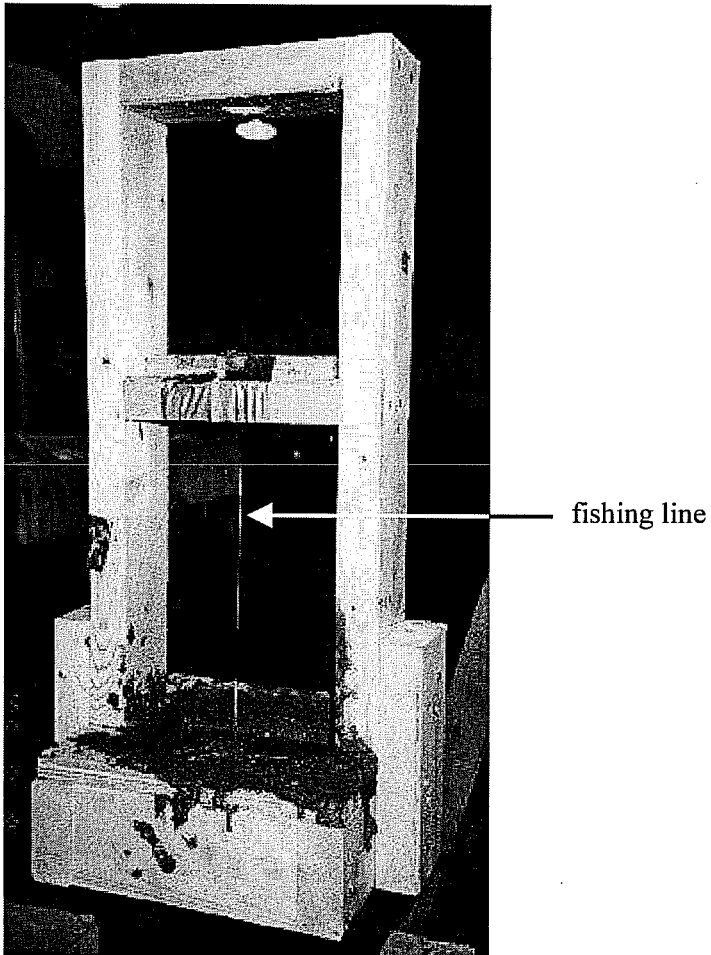


Figure 2.13. CFT specimen after casting of the concrete had been completed.

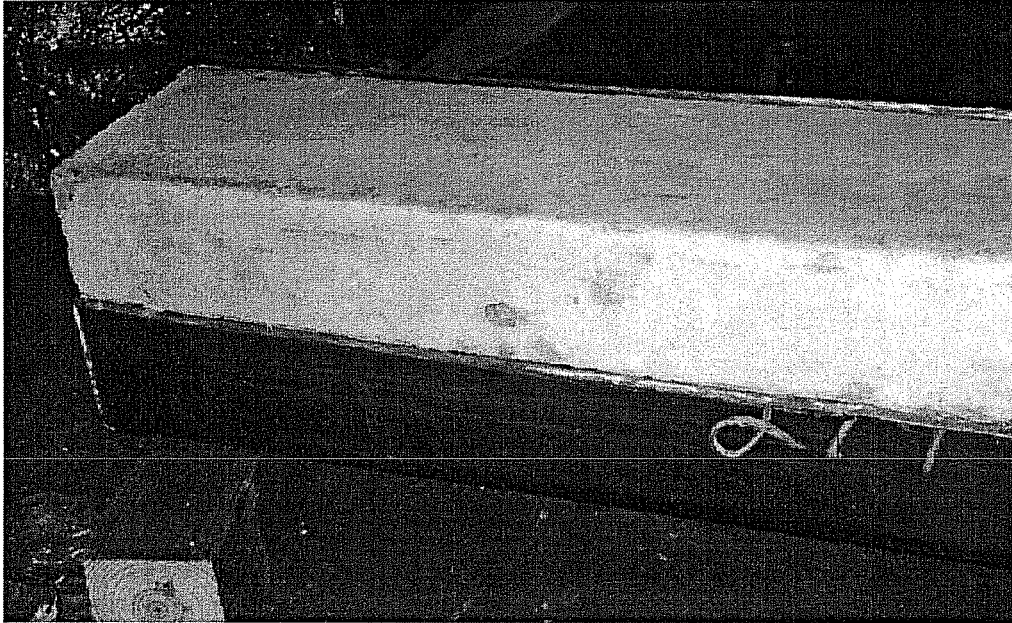


Figure 2.14. The concrete core of a specimen after removal of one side of the steel tube.

INSTRUMENTATION OF SPECIMENS

The instrumentation of the specimens was designed to provide insight into the shear transfer mechanism during a push-out test of a CFT column. For instance, to determine an experimental bond strength, the load on the specimen at failure must be measured. In these tests, the applied load was measured by the testing machine load cell and stored by the data acquisition system. In addition to load measurement, data were collected from strain and deflection gages attached directly to each specimen. Figure 2.15 shows a diagram of a typical instrumentation scheme used in these tests.

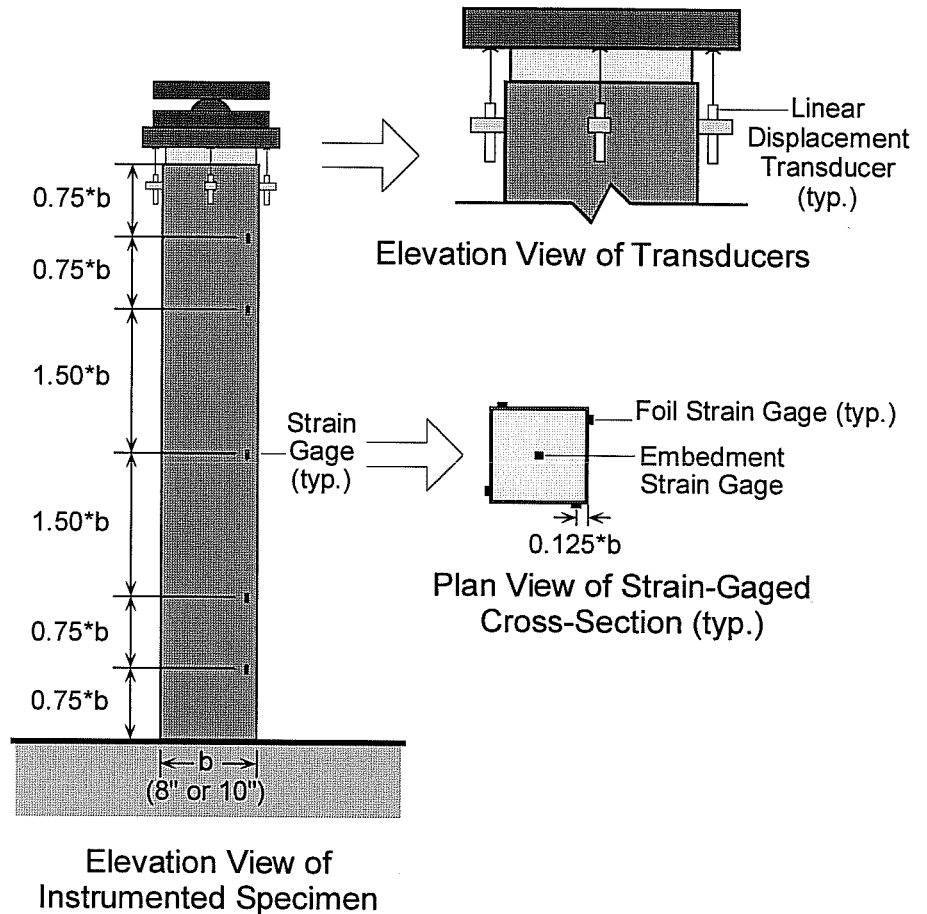


Figure 2.15. Diagram of the typical instrumentation scheme for a CFT specimen.

Displacement Measurements

Displacement measurements were needed to characterize the load-slip behavior of the concrete core during testing. As shown in Figure 2.15, linear displacement transducers with a 2-in. stroke were attached to the steel tube near the concrete-loaded end of the specimen. They measured the relative displacement between the upper crosshead and the top of the steel tube, essentially the slip of the concrete core. In most cases, four transducers were each fastened to a small aluminum block, and the blocks were securely attached to the steel tube with epoxy, one on each side of a specimen. Slip of the concrete core was taken as the average of these four values.

Strain Measurements

Strain gages were placed along the length of the specimen to provide information on the distribution of axial load to the steel tube and to the concrete core at a particular transverse plane. Comparing the load distributions at various cross-sections indicated which portion of the interface was contributing to the shear transfer. As shown in Figure 2.15, five planes were selected for instrumentation with strain gages. The instrumented cross-sections were concentrated at the ends of the specimen, where most of the load transfer was expected to occur.

At each instrumented cross-section, strain gages were placed in the concrete core and on the outer surface of the steel tube. The gages at the centroid of the concrete core measured the longitudinal strains at the instrumented plane. The embedment gages used were type PMLS-10, manufactured by Tokyo Sokki Kenkyujo Co. According to the manufacturer, these strain gages were made from a standard wire gage hermetically sealed between thin resin plates for waterproofing. A coarse grit coating enhanced the bond between the gage and the concrete in which it was embedded. The strain gage itself had a length of 12 mm, a width of 1 mm, and a nominal resistance of 120 Ω . The total length of the gage including the resin plates and the grit coating was 1 in.

At the same cross-sections where the concrete strains were measured, strains in the steel tube were also recorded. To avoid interference with the steel-concrete bond, only gages on the outer steel surface were used. Four strain gages were placed on the steel tube at each instrumented cross-section, one on each corner of the rectangular tube. The gages were attached at the corners because the increased stiffness there resulted in smaller local bending strains of the tube wall. Therefore, the longitudinal strains measured could be attributed solely to the axial load in the steel tube, neglecting the contribution of the much smaller strains due to bending. The 3-mm long, 1.7-mm wide, 120- Ω strain gages used on the steel surface were type FLA-3-11, manufactured by Tokyo Sokki Kenkyujo Co.

VALIDITY AND RELIABILITY OF THE MEASUREMENTS

Strains Inside the Concrete Core

Prior to testing of CFT specimens, an investigation into the accuracy and reliability of the concrete embedment gages was performed. Several concrete cylinders 6 inches in diameter were instrumented and tested in axial compression. Like the CFT specimens, these cylinders had embedment gages attached to a fishing line that followed the centroidal axis of the cylinder. Five cylinders were instrumented with a total of 11 gages fastened to fishing line. One cylinder had only one embedded gage, two cylinders had two gages in series, and the remaining two cylinders had three gages in series.

A compressive load was applied to the specimens. The strains in the concrete were measured by the embedment gages, while the centerline displacement of the cylinder was determined with a compressometer. After the compressometer measurements were converted into equivalent strains in the concrete, a comparison of the compressometer-determined strains and the gage-measured strains could be made. The differences between the two methods of determining strains ranged from 2 to 21% for any of the 11 gages. The average error for the strain measured by any gage was 9%.

A possible source of error in the measurement of longitudinal strains by an embedment gage is misalignment of the gage within the concrete. The two knots tied in the fishing line at either end of a gage are intended to align the gage with the fishing line when a tensile force is applied to the line during hardening of the concrete. The effectiveness of this technique may be established by comparing the intended placement of the gages with their actual locations. For this purpose, a saw cut was made in one of the instrumented cylinders. In Figure 2.16, two embedment gages can be seen attached in series to the fishing line at the centroidal axis of the cylinder. These gages are both in their intended locations and have a nearly perfect vertical alignment.

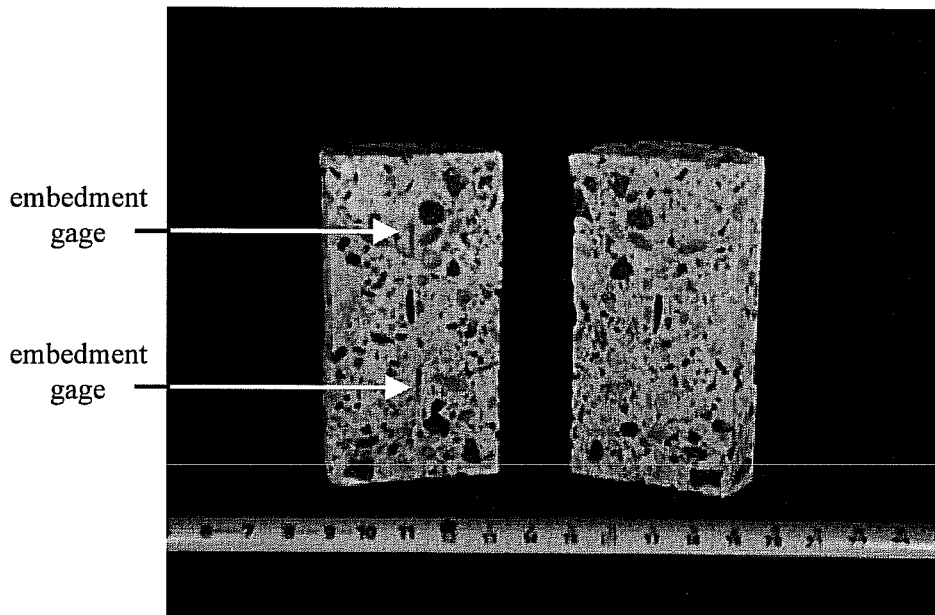


Figure 2.16. A concrete cylinder instrumented with two embedment gages along the centroidal axis.

Strains on the Surface of the Steel Tube

The placement of the strain gages at the corners of the steel tube was selected to minimize the longitudinal strains produced by local bending of the tube wall. However, an estimate of the relative magnitude of the bending strains as compared to the axial strains is desired to assess the accuracy with which a gage on the surface can indicate the strains at the neutral axis of a wall of the tube. The longitudinal strains measured at the neutral axis would be the strains due solely to the axial force in the steel tube.

Four special “one-sided” strain gages were attached to the surface of CFT4 to determine both axial strain and bending strain. Each “one-sided” gage consisted of two strain gages mounted on a 3-mm thick resin strip. On the surface of the thick resin strip attached to the steel tube was one strain gage, and another gage was located on the opposite surface, at a distance of 3 mm away from the outer steel surface. Since the strains at two locations in a transverse plane were known, the strain at the neutral axis of the tube, or centerline, could then be calculated. The primary advantage of this type of strain gage is the ability to measure bending strains without attaching a strain gage to the

inner surface of the steel tube and disrupting the steel-concrete bond. On the other hand, these gages typically cost 10 times the price of a standard foil gage used to measure steel strains.

In Figures 2.17 through 2.20, the measured and calculated strains for each of the “one-sided” gages are presented. The strains measured by a surface and an upper gage, in addition to the strain calculated at the neutral axis, are shown. The difference between the surface and centerline strains ranged from 5 to 17% for the four instruments, with an average error of 10% or a strain of 0.000006. Thus, it can be assumed that bending strains contributed about 10% of the longitudinal strains measured on the surface of the steel tube. A possible error of 10% in the strains measured by the strain gages on the surface of the steel tube seemed acceptable when compared to the prohibitive costs of instrumenting eight CFT’s with 20 “one-sided” gages for each.

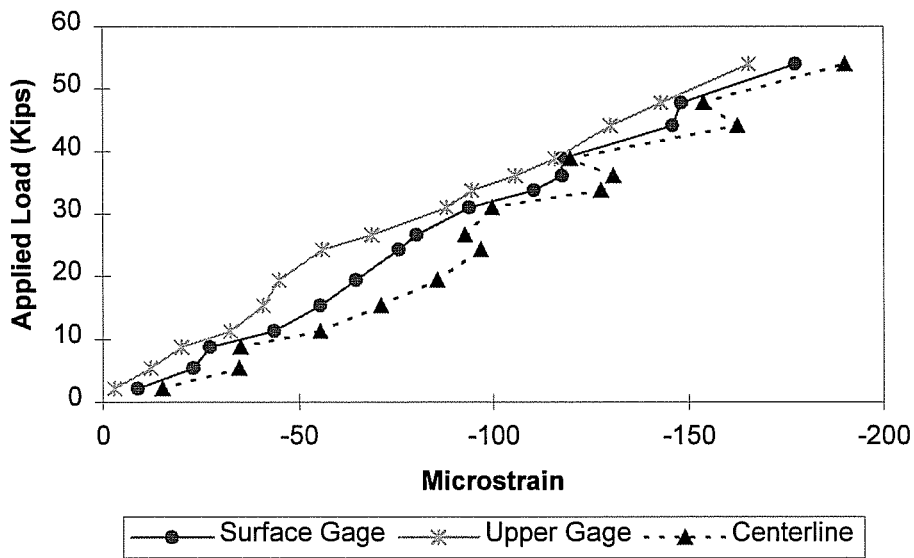


Figure 2.17. Longitudinal centerline and surface strains measured by one-sided Gage “A” of CFT4.

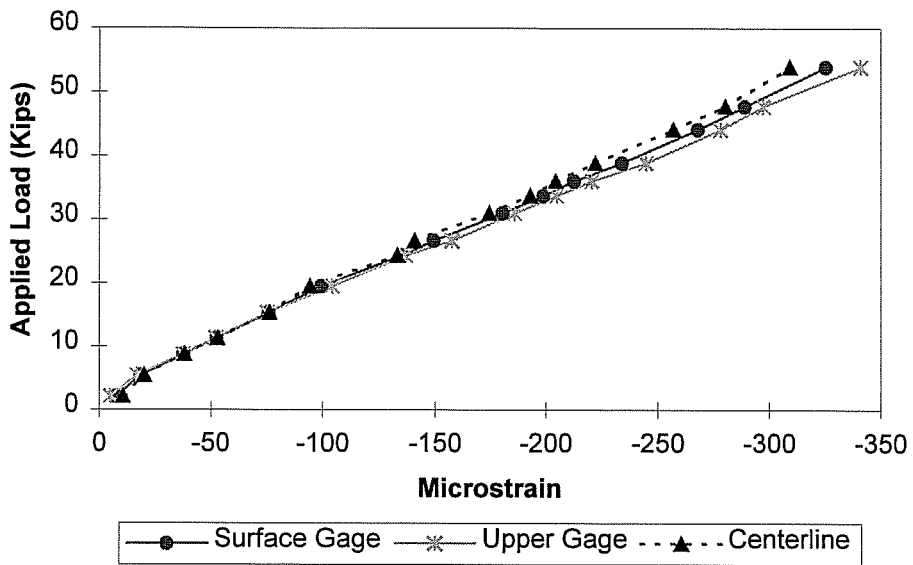


Figure 2.18. Longitudinal centerline and surface strains measured by one-sided Gage “B” of CFT4.

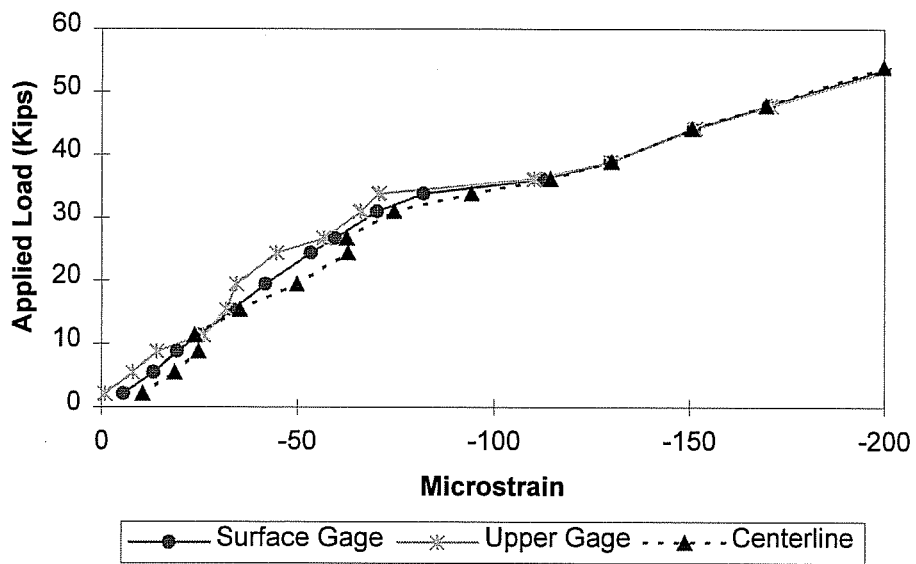


Figure 2.19. Longitudinal centerline and surface strains measured by one-sided Gage “C” of CFT4.

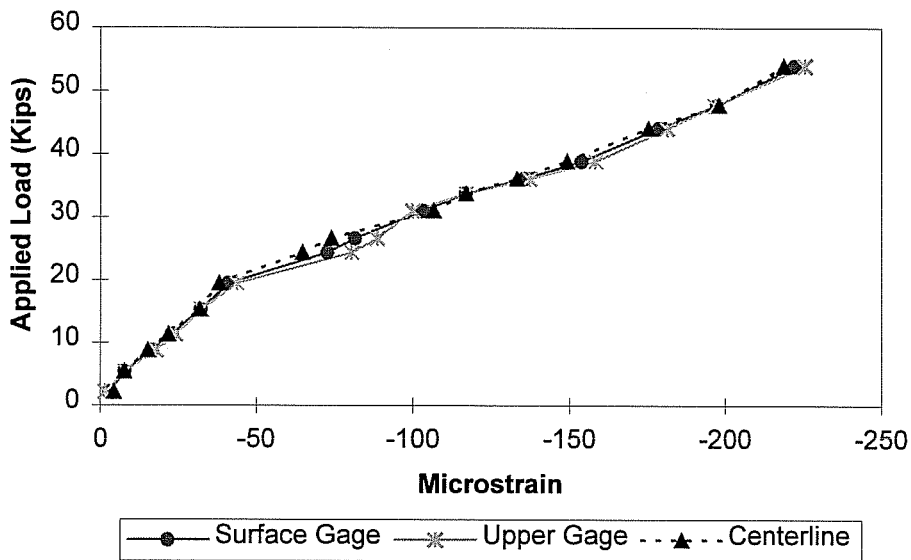


Figure 2.20. Longitudinal centerline and surface strains measured by one-sided Gage “D” of CFT4.

Displacement of the Concrete Core

The instrumentation of a typical specimen with displacement transducers at the concrete-loaded end was based on the assumption that the concrete core moved as a whole. In other words, slip of the core at any plane along the length of the interface was assumed the same as the slip of the concrete core measured at the end of the specimen. An investigation into the distribution of slip of the concrete core was performed with specimen CFT3. Like all specimens, CFT3 was instrumented with displacement transducers attached to the top of the steel tube to record displacement of the upper crosshead relative to the steel tube. However, CFT3 also had a displacement transducer which recorded the displacement of the concrete core relative to the lower (fixed) crosshead. Measuring slip of the concrete core from the bottom side of the specimen was accomplished by supporting the tube on steel blocks. These blocks were 4 inches in height and arranged along the perimeter of the rectangular tube, creating ample space underneath the center of the specimen for a transducer.

Figure 2.21 compares the displacements measured for CFT3 during the initial stages of loading. One curve shows the displacement of the concrete core as determined by the average displacement of the transducers located at the top of the steel tube. The second curve on the same plot is the displacement of the concrete core as measured by the transducer located beneath the specimen. Initially, the data indicated a reduction in slip of the concrete core from the top to the bottom. This difference can likely be attributed to localized wedging of the concrete core inside the steel tube at various points along the interface. On the other hand, at an applied load of 35 kips, the displacements were seen to be nearly equal, indicating movement of the concrete core as a rigid body. In fact, as testing of CFT3 was carried out to completion, both displacements were approximately the same (Figure 2.22). In remaining experiments, only the displacement of the concrete core as measured by the transducers attached to the top of the steel tube was recorded.

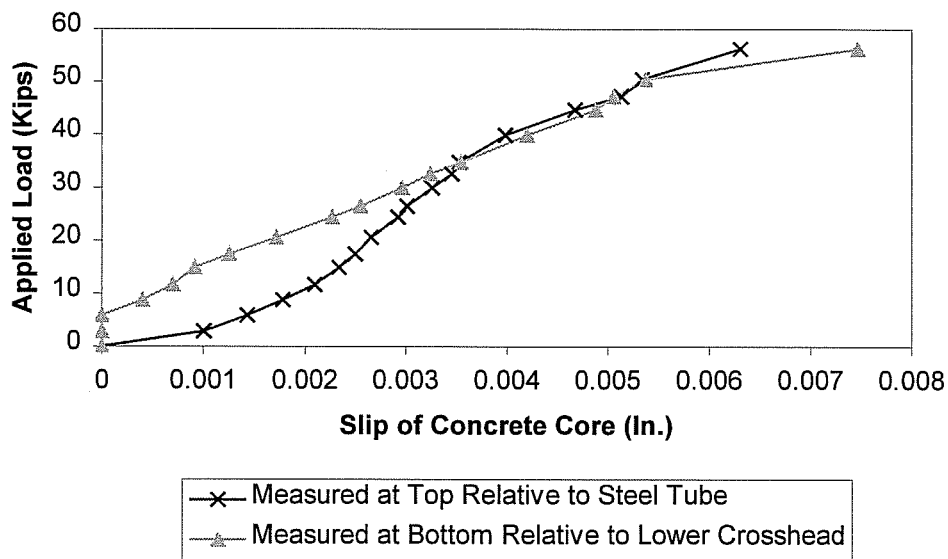


Figure 2.21. Slip of the concrete core of CFT3 in the initial stages of loading.

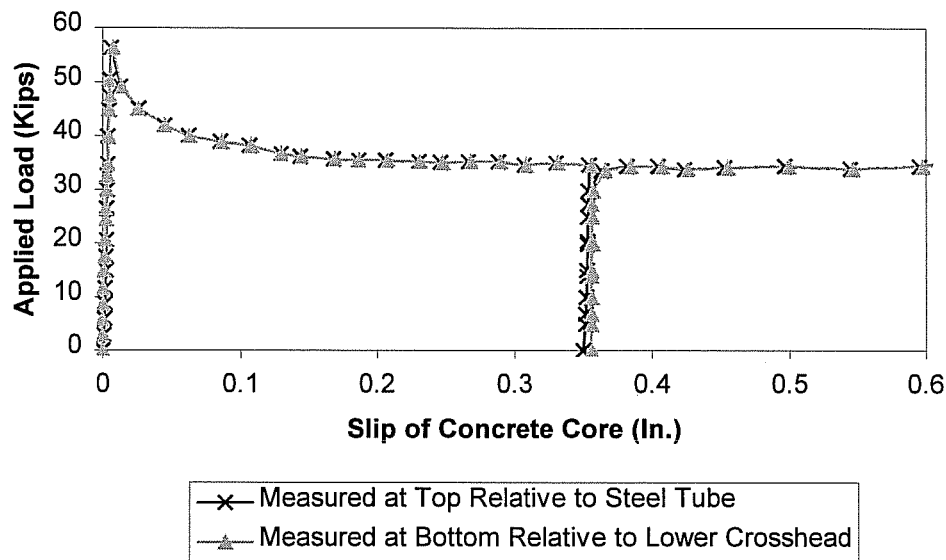


Figure 2.22. Slip of the concrete core of CFT3 from the beginning to the end of the test.

TEST SETUP AND PROCEDURE

All push-out test specimens were tested in a 600-kip screw-type universal testing machine. As shown in Figures 2.1 through 2.4, the lower crosshead was fixed, and the compressive load was applied by the movable spherical crosshead. Before loading, the specimen was centered horizontally between the crossheads. Figure 2.23 is a photograph of a shear-tab specimen in the testing machine before loading. Because the ends of the specimens were not machined, hydrostone was used to create a plane surface for loading. Hydrostone was applied as needed to fill in any gaps either between the tube end and the fixed crosshead or between the shear tab loading fixture and the crosshead.

An initial compressive load of about five kips was applied to each specimen to allow any initial settlement due to irregular surface conditions to occur before data were collected. This load was removed before the zero readings were taken. During testing, load was applied at a rate of about 4 kips per minute. Data were initially recorded after increments of 3 to 5 kips of load were applied. When the load-slip curve began to show a decrease in stiffness, the data collection was then determined by the magnitude of the slip of the infilled concrete. Recordings were taken after every 0.03 to 0.05 inches of

displacement. Loading of the specimens continued until further displacement of the concrete core was impeded by the test setup.

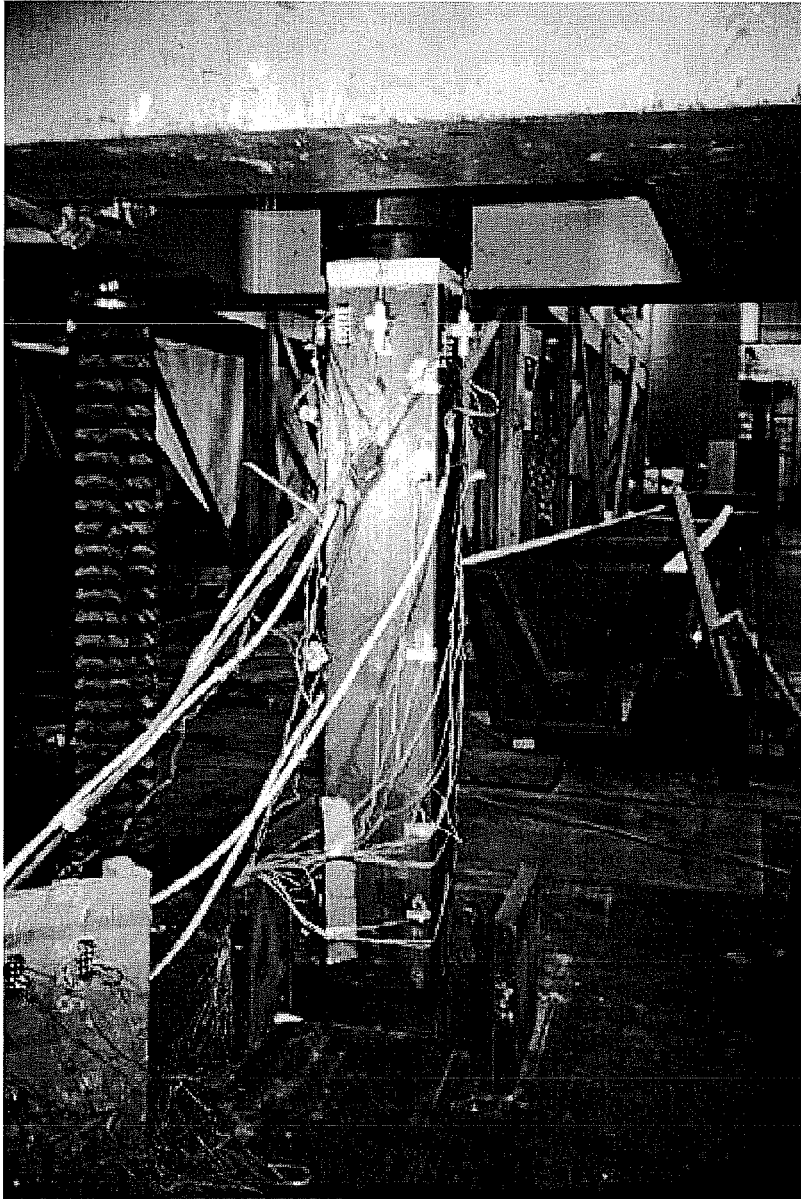


Figure 2.23. The shear-tab specimen in the testing machine at the start of loading.

CHAPTER 3

EVALUATION OF TEST DATA

Before an analysis of the strain gage data can be performed, the data must be evaluated for the accuracy with which they reflect the behavior of the specimen. For instance, the measured strains are useful in analysis insofar as the corresponding stresses can be accurately predicted. Once the average strains in the steel and in the concrete at a cross-section are known, then the stress in the steel and the stress in the concrete can be determined from the stress-strain relationship of each material.

DETERMINATION OF STRESSES FROM STRAIN DATA

The stress-strain behavior of the steel tube is not affected by the presence of the concrete core. Most structural steels behave as an elastic material until strains of 0.0012 to 0.0017 are reached. A constant relationship between stress and strain characterizes elastic behavior of steel. The modulus of elasticity, or the constant of proportionality that relates stress to strain, is typically accepted as 29,000 kips/in² for steel. Since all measured steel strains in the CFT push-out specimens were in the elastic range, this value has been selected for use in all stress calculations involving the steel strain data.

The stress-strain behavior of the infilled concrete, however, may be changed by transverse confining pressure imposed by the steel tube. In the following section, various opinions on the effect of confinement on the behavior of concrete are summarized.

EFFECT OF CONFINEMENT OF CONCRETE

Most research on the confinement of concrete involves the effect it has on longitudinal compressive strength. According to Knowles and Park (1969), "One of the main advantages claimed for a column constructed from a steel tube filled with concrete is that the concrete core of the column is subjected to a confining stress and as a result can carry a considerably larger axial stress than similar unconfined concrete." Gardner

and Jacobson (1967) agree that “[a]s the steel tube restrains the concrete at failure then the longitudinal compressive strength of the concrete will be augmented.” Neogi, Sen, and Chapman (1969) explain the mechanism of confinement in a CFT.

As the longitudinal strain increases, . . . the lateral expansion of unconfined concrete gradually becomes greater than that of steel. A radial pressure therefore develops at the steel-concrete interface, thereby restraining the concrete core and setting up a hoop tension in the tube.

Past experiments involving triaxial tests of concrete have shown that concrete cylinders under an axial compressive stress and a transverse confining pressure support higher axial loads than similar unconfined concrete cylinders.

However, do the benefits of confinement apply to square CFT’s since the confinement acts only at the corners? The opinions vary on the effectiveness of confinement in the square tubes. Nevertheless, most researchers agree that confinement is not effective in square CFT’s. Knowles and Park (1969) tested short square tubes and found no significant increase in concrete strength. According to Furlong (1967),

Any transverse confinement of concrete provided by steel encasement should be more effective in round cross sections than in sections with flat sides. Round sections can develop an effective hoop tension to provide lateral confinement, but flat sides are not very stiff against pressure perpendicular to the flat face. . . . Consequently, no effective lateral confinement seems justified for tubing with flat sides.

Although no definite conclusion has been reached on whether concrete contained in square tubes experiences an increase in strength, a more pertinent issue to the current series of experiments is how confinement of the concrete affects its elastic modulus. On one hand, the empirical equation presented in the ACI Building Code (1995) suggests that the modulus of concrete (E_c) is a function of the concrete compressive strength. On

the other hand, Klöppel and Goder (1957) concluded that the modulus of elasticity of concrete contained in a steel tube is accurately predicted by the modulus of similar concrete under uniaxial stress. Thus, many questions regarding the effectiveness of confinement in square CFT's remain unanswered.

SELECTION OF E_c USED IN THE ANALYSIS OF TEST DATA

With so many unanswered questions on the modulus of elasticity of confined concrete, it was decided to determine E_c experimentally. Two short columns, one each of 8-in. and 10-in. widths, were constructed for these experiments. The steel tubes used for the short columns were cut from the same lengths of tubing as the larger specimens. Similarly, the concrete was cast from the same batches used in the construction of the full-size CFT's. The length of the 8 x 8 x ¼-in. short specimen was 12 inches, while the short specimen constructed from a 10 x 10 x ¼-in. tube had a length of 15 inches, thereby maintaining the same length-to-width ratio. At the centroid of the concrete core was an embedment gage that would measure longitudinal strains in the concrete. Figure 3.1 shows a short tube before casting of the concrete. The embedment gage can be seen tied to a piece of fishing line that would hold the gage in its desired position in the plastic concrete.

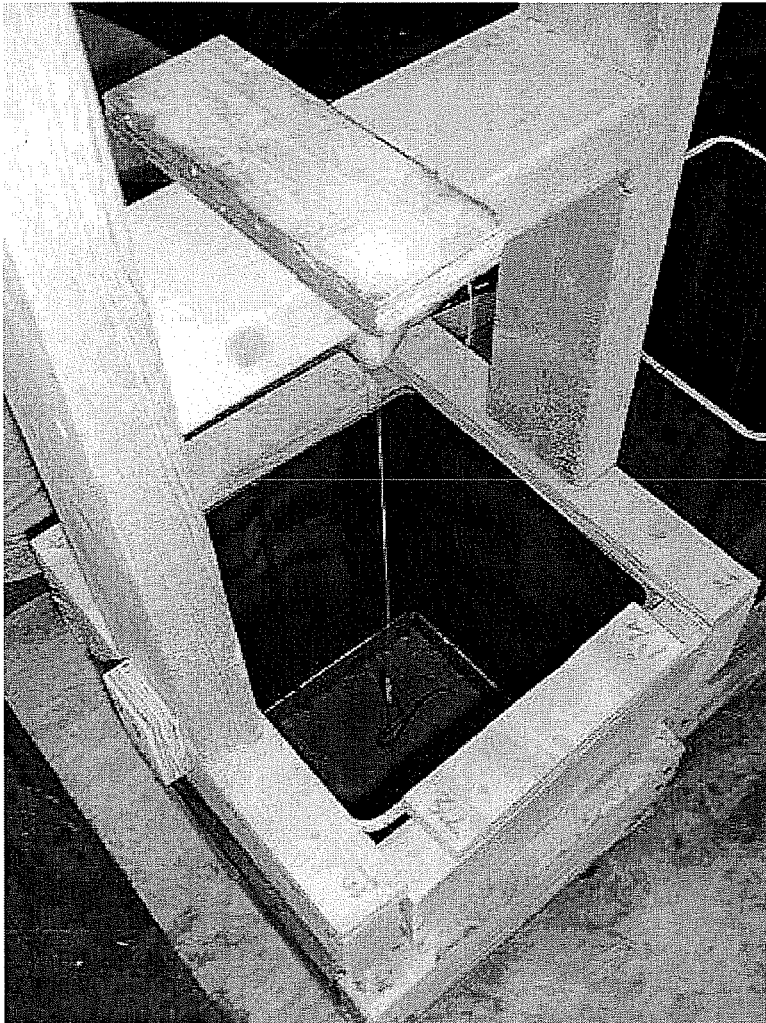


Figure 3.1. Short column specimen prior to casting of the infilled concrete.

The infilled concrete was cast to a depth flush with the edges of the steel tube at both ends. During testing, an axial compressive load was applied directly to the concrete core at each end of the short columns. The longitudinal strain in the concrete at midheight of each specimen was recorded. Although the steel tube was not loaded directly, a small percentage of the axial load applied to the concrete at the ends was expected to be transferred to the steel tube by the interface. To determine the magnitude of the axial load supported by the steel tube at midheight, a strain gage was placed on

each corner of the steel tube. Additionally, the testing machine load cell measured the applied load.

The purpose of these tests was to study the stress-strain behavior of the contained concrete. The data were analyzed as follows. The amount of axial load supported by the steel tube at midheight was calculated by first multiplying the average strain in the steel at that plane by the elastic modulus for steel to obtain the average stress in the steel tube. Then the stresses were converted into forces by multiplication with the average cross-sectional area of the steel. The difference between the applied load and the load supported by the steel tube at midheight was considered to have been supported by the infilled concrete. The longitudinal stress in the concrete was obtained by dividing the load in the concrete by the area of the concrete core. From this information, a plot of the relationship between the calculated stress and the strain measured by the embedment gage in the concrete core could be developed. The maximum axial load applied during the tests of the short columns was that load which would cause strains in the concrete of similar magnitude to the strains recorded in the concrete during the push-out tests of the full-size specimens.

Three tests of the short columns were performed. The 8-in. short column was tested at approximately the time CFT4 and CFT3 were tested. Since this test was nondestructive for the specimen at the low loads applied, it was repeated later when CFT2 and CFT5 were tested. The 10-in. short column was tested at the same time as the push-out tests of specimens of 10-in. width.

Figures 3.2, 3.3, and 3.4 show the stress-strain plots generated from the three tests. The associated modulus of elasticity was obtained from the slope of the best-fit line through each of these curves. E_c for the column of 8-in. width, as determined during the first test, was 6040 ksi. This is the value for E_c that was used in the data analyses of CFT4 and CFT3. Testing of the same short column at a later date indicated E_c was 6120 ksi, the value used in the analyses of specimens CFT2 and CFT5. The 10-in. short column indicated E_c was 6000 ksi. Analyses of all 10-in. CFT's were based on this modulus for the calculation of stresses.

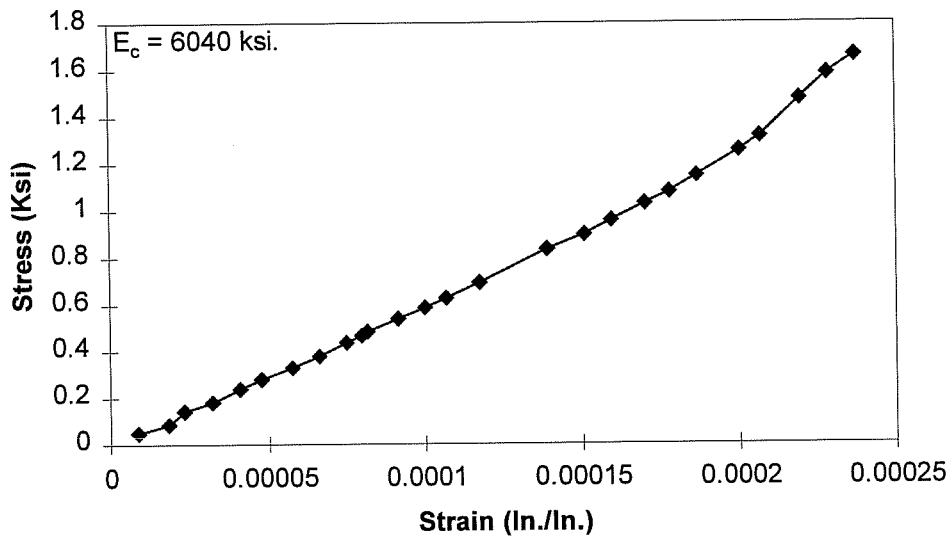


Figure 3.2. Stress-strain relationship for the concrete contained in the CFT's of 8-in. width, as determined at 120 days.

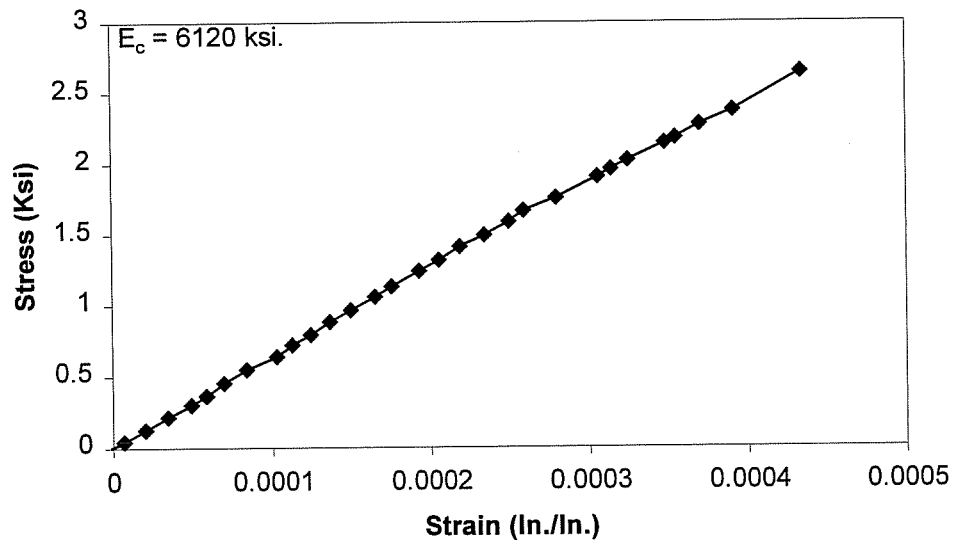


Figure 3.3. Stress-strain relationship for the concrete contained in the CFT's of 8-in. width, as determined at 380 days.

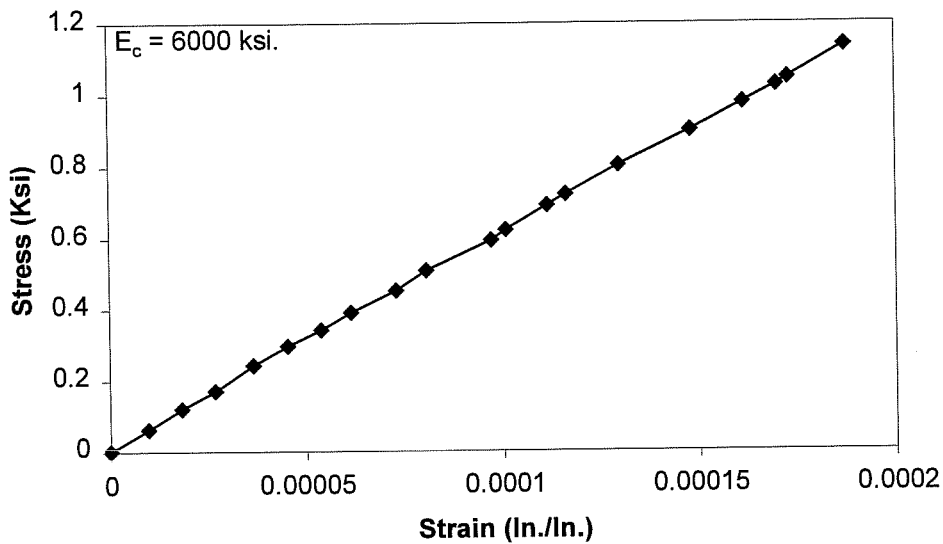


Figure 3.4. Stress-strain relationship for the concrete contained in the CFT's of 10-in. width, as determined at 190 days.

For comparison, E_c for the same concrete in an unconfined state was determined at the same time that the short columns were tested. Compression tests of 6-in. diameter concrete cylinders were performed using a compressometer to measure axial displacements of the centerline of the cylinder under the applied load. Values for E_c of the unconfined cylinders are presented along with the moduli of the tube-contained concrete in Table 3.1. Table 3.1 also includes values for E_c as predicted by the empirical equation given for normal weight concrete in Section 8.5 of the ACI Building Code (1995): $E_c = 57,000 \sqrt{f'_c}$, where f'_c is the compressive strength of the concrete in psi.

Table 3.1. A comparison of methods used to calculate E_c of the contained concrete.

Concrete Batch	Age of Concrete (Days)	Concrete Compressive Strength (Psi)	Method of Determining E_c		
			E_c by Short Column Tests (Ksi)	E_c by Unconfined Cylinder Tests (Ksi)	E_c by Empirical Equation (Ksi)
8" CFT's	120	7580	6040	6310	4960
8" CFT's	380	7500	6120	5700	4940
10" CFT's	190	6720	6000	5240	4670

VALIDATION OF THE CONSTITUTIVE RELATIONSHIPS USED IN THE ANALYSIS OF DATA

The constitutive relationships selected in the previous section were applied to the analysis of the push-out test specimens. Using the values for E_c obtained experimentally for the contained concrete, the strains in the concrete core were converted into stresses. Similarly, the strains in the steel multiplied by the elastic modulus of the steel gave stresses, which were averaged at a cross-section. From the average stress in the steel and the stress in the concrete at a section, the corresponding axial loads were calculated by multiplying the stresses by the area of the steel or the concrete. In an ideal analysis, the sum of the axial load in the steel and in the concrete at an instrumented cross-section would be equal to the load applied by the testing machine. A comparison of the load predicted by the strain gage data at a section to the actual applied load indicates the accuracy of the constitutive relationships used in the analysis.

A typical plot of the axial loads predicted from the strain gage data for an instrumented cross-section of one push-out test specimen is shown in Figure 3.5. The appendix provides similar plots for all instrumented cross-sections of all eight specimens. The slope of the best-fit line drawn through the predicted axial loads from zero up to the maximum load that the CFT supported is compared to the slope of the same line in an ideal analysis, i.e., that in which the strain gage data predict the applied loads exactly. The difference between the slope of the experimental best-fit line and the slope of the line representing ideal conditions, which is given as a percentage on each figure, indicates the amount of error in the strain gage data analysis at a cross-section.

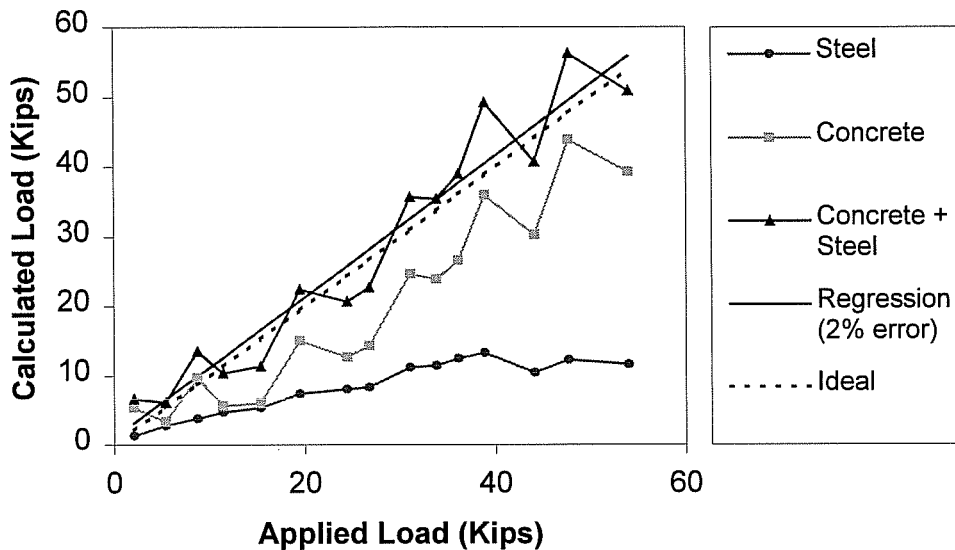


Figure 3.5. A typical plot of axial load as calculated using strain data. This figure corresponds to a cross-section located 6 inches from the concrete-loaded end of CFT4.

Examination of the strain gage data revealed that in the course of testing some of the gages did not provide reliable measurements. When a gage was found suspicious, changes to the analysis technique were made. If the reliable gage for this cross-section was the embedment gage in the concrete, the concrete stresses and axial loads were calculated by the usual method. The load in the steel at that section was then given by the difference between the applied load and the load in the concrete. On the other hand, if the embedment gage in the concrete was the instrument providing unreliable data, then the load in the concrete at that section became the difference between the applied load and the calculated load in the steel. In all, gages on 8 of the 40 instrumented cross-sections seemed unreliable. Cross-sections in which unreliable gages were located and the affected gages are identified in Figures A8, A10, A11, A14, A16, A25, A28, and A36.

Where the presence of the shear tabs prevented the axial load from being evenly distributed over the entire cross-sectional area of steel, the location of strain gages at the

corners of the steel tube was not adequate to determine the axial load in the steel at that section. Therefore, the set of data from these strain gages was considered incomplete, and the analysis was altered as though the gages were defective. The four affected cross-sections are identified in Figures A15, A20, A35, and A40.

Of the 28 cross-sections in which all of the gages provided useful and reliable strain information, the average error between the axial loads predicted by the strains and the actual applied load was 6% when the moduli of elasticity of the steel and the concrete were selected as described in this section.

CHAPTER 4

EXPERIMENTAL RESULTS

The results of the push-out tests are presented in the form of the load-slip response, the distribution of longitudinal shearing stresses, and the bond slip distribution. Important observations about the analyzed data are introduced, and related photographs have been included. Where the results of two replicate specimens are nearly the same, a complete set of results from only one of the two specimens is included in this chapter.

EXPERIMENTAL BEHAVIOR OF 8-IN. CFT'S WITHOUT SHEAR TABS

Load - Slip Response

Figure 4.1 shows the applied load-slip relationships for CFT4 and CFT3. In the early stages of loading, prior to gross slip of the infilled concrete, the stiffnesses shown by the load-displacement curves were high. In this thesis, the term “gross slip” is used to describe rigid body movement of the entire concrete core. After a peak axial load (P_{max}) was reached for a specimen, large slips were observed at incrementally decreasing loads. The values of P_{max} for CFT4 and CFT3 were 61 kips and 56 kips, respectively. The loads decreased from the peak values until the load-slip curves eventually flattened out. Displacements continued at a relatively constant load until the concrete cores had completely pushed through the steel tubes. For CFT4 and CFT3, these constant loads were 32 kips and 31 kips, respectively. Thus, many similarities can be seen in the comparison of the load-slip behaviors of replicate specimens CFT4 and CFT3.

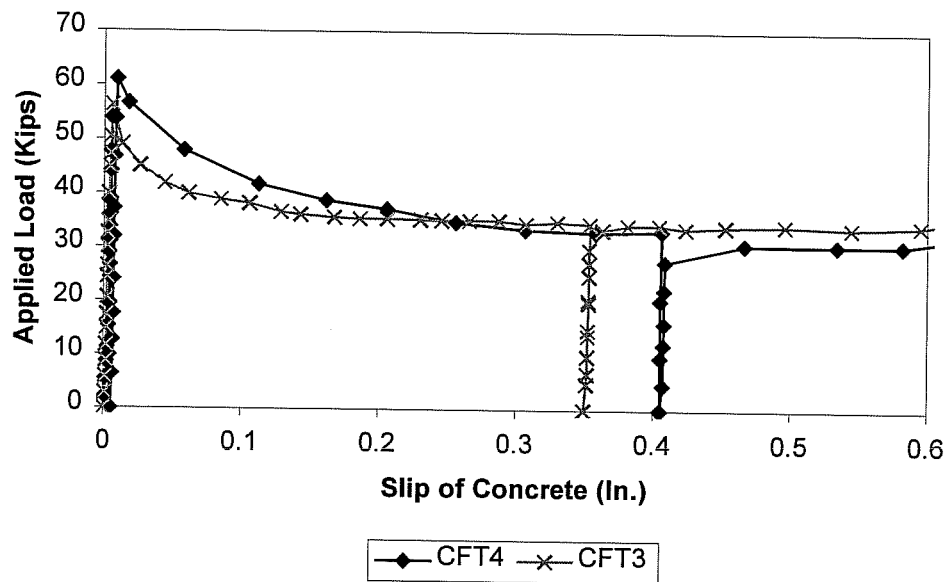


Figure 4.1. Applied axial load vs. slip of the infilled concrete for CFT4 and CFT3.

Specimen CFT4 was unloaded and reloaded twice to investigate the differences between initial and reloading stiffnesses. The first unloading occurred prior to the peak load, while the second unloading occurred after the concrete core had slipped approximately 0.4 inches. Figure 4.2 shows both the initial load-slip response and the first cycle of unloading and reloading. Generally, initial stiffness of a push-out specimen is difficult to determine. In this case, the initial load-slip response was essentially bilinear, exhibiting an increase in stiffness at a load of 20 kips. A possible explanation for this stiffening is that the specimen initially experienced localized slip of the infilled concrete until the concrete core was wedged into a position that enabled it to better resist slip. At loads from 20 kips to 54 kips, an initial stiffness of 26,000 kips/inch was calculated using linear regression techniques. On the other hand, the reloading behavior of CFT4 was relatively linear from the initial reapplication of load to the peak load. A stiffness of 18,200 kips/inch was estimated for this reloading.

The reloading stiffness after large slip of the concrete core had occurred was 14,600 kips/inch from the linear load-displacement response in Figure 4.3.

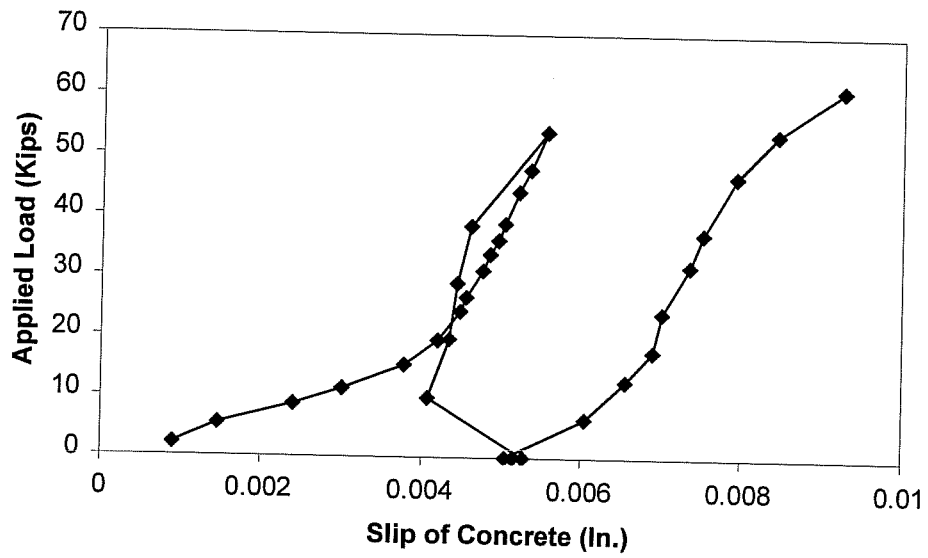


Figure 4.2. Load-slip response of CFT4 during initial loading and the first reloading.

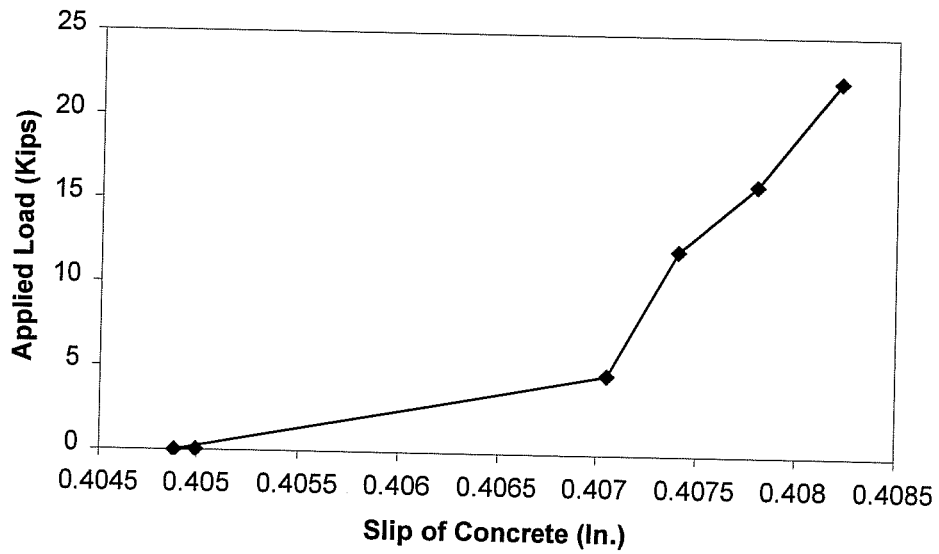


Figure 4.3. Load-slip response of CFT4 during the second reloading.

For comparison, the initial stiffness of CFT3 was 11,100 kips/inch. The load on CFT3 was removed and reapplied only once during the experiment for the measurement of a reloading stiffness. This reloading occurred after the peak load, at a point associated with the plateau region of the load-slip curve. Similar to the reloading curve of in CFT4, this curve was relatively linear, and a stiffness of 14,500 kips/inch was determined for the reloading of CFT3.

Distribution of Longitudinal Shearing Stresses

Because the results of specimens CFT4 and CFT3 were nearly identical, CFT4 may be considered typical of 8-in. CFT's without shear tabs. Therefore, only the results of CFT4 are shown here. Where the results of CFT4 and CFT3 differ, CFT3 is also discussed.

From the stresses in the concrete and steel determined in Chapter 3, the proportion of axial load resisted by the steel and concrete at a transverse plane can be found at the five cross-section locations where strains were measured. Additionally, it is known that concrete alone and steel alone supported the load at each end. Longitudinal shearing stresses along a portion of the CFT are proportional to the rate of change (slope) of the steel or concrete load distribution curve between two instrumented cross-sections. In regions between the cross-sections where strains were measured, the distribution of load was interpolated from the proportions at instrumented cross-sections assuming constant bond stresses (slope) between those planes.

Figure 4.4 shows the distribution of load along the length of CFT4 at an applied load of $0.25 P_{max}$. On the x-axis of the plot, zero (inches) refers to the end of the steel tube at which the load is applied to the concrete, while 48 (inches) refers to the steel-loaded end of the tube. This figure shows that the rate of change of load in the steel was greatest along portions of the interface located at distances from zero to 6 inches and from 36 to 48 inches relative to the concrete-loaded end. Thus, bond stresses were largest at the ends of the CFT, and most of the load transfer at an applied load of $0.25 P_{max}$ occurred there.

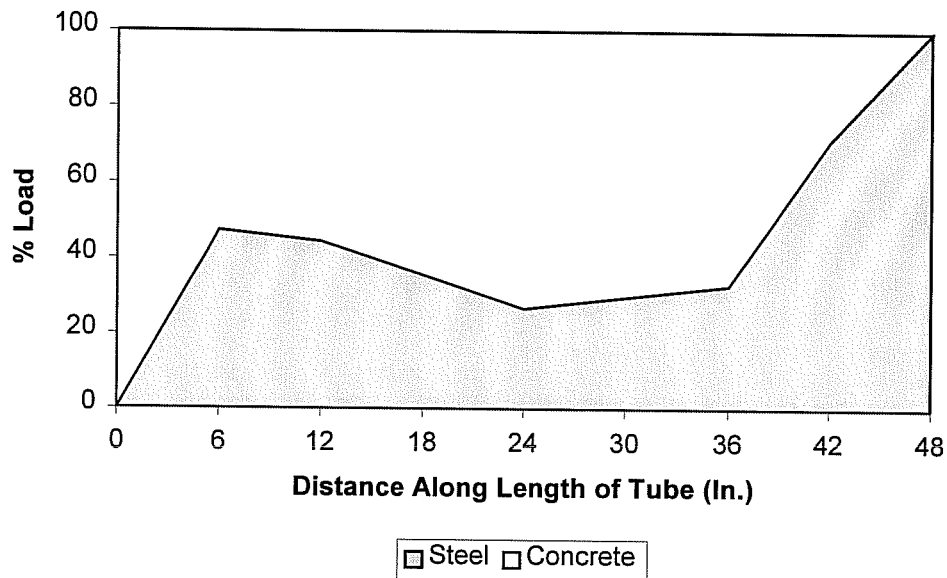


Figure 4.4. Percentage of applied axial load resisted by the steel tube and the concrete core along the length of CFT4 at $P = 0.25 P_{max}$.

As the applied loads were increased, a longer portion of the interface was called upon to resist the shear. The progression of load transfer along the length of CFT4 as the loads were increased can be seen in the sequence of Figures 4.5, 4.6, and 4.7. These figures present the distribution of load between the steel and concrete at applied loads of $0.51 P_{max}$, $0.72 P_{max}$, and $0.88 P_{max}$, respectively. At 51% of the peak load, the ends of the CFT still provided most of the load transfer from the steel to the concrete. At an applied load of $0.72 P_{max}$, the proportion of load resisted by the steel tube increased along a length of interface located 24 to 42 inches from the concrete-loaded end. The nearly constant rate of change of load resisted by the steel along the entire length of the CFT indicates that when the load reached $0.88 P_{max}$, the load transfer was evenly distributed (Figure 4.7).

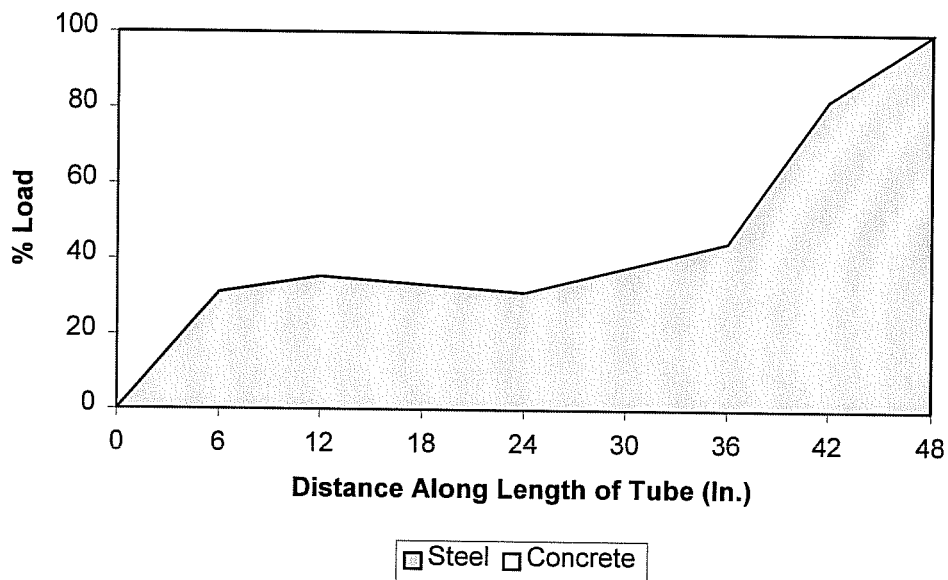


Figure 4.5. Percentage of applied axial load resisted by the steel tube and the concrete core along the length of CFT4 at $P = 0.51 P_{max}$.

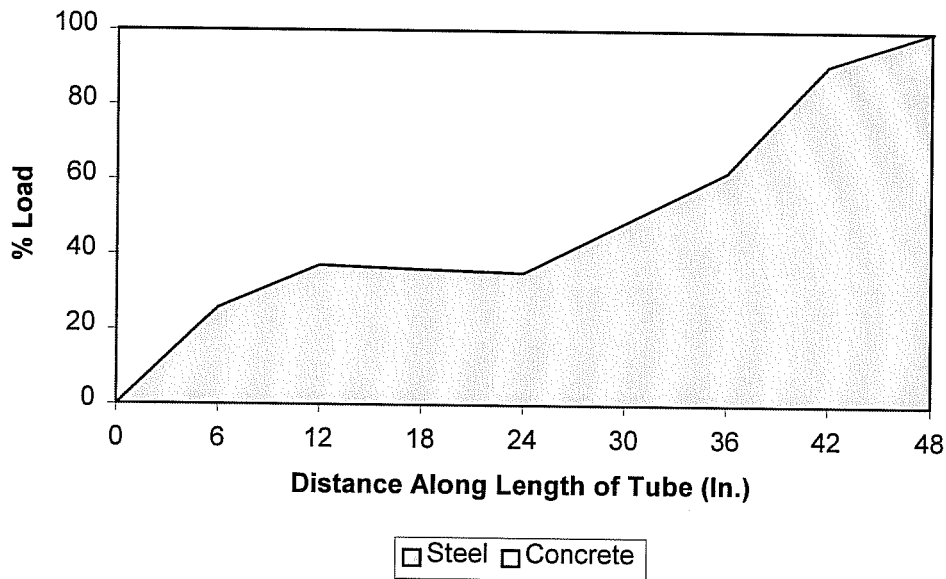


Figure 4.6. Percentage of applied axial load resisted by the steel tube and the concrete core along the length of CFT4 at $P = 0.72 P_{max}$.

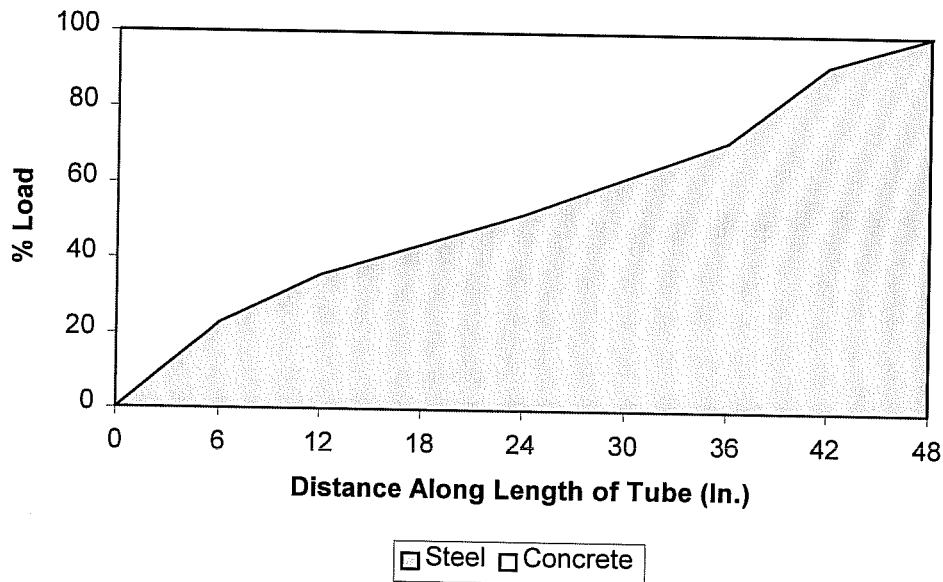


Figure 4.7. Percentage of applied axial load resisted by the steel tube and the concrete core along the length of CFT4 at $P = 0.88 P_{max}$.

Immediately preceding the peak load, the behavior of CFT3 differed somewhat from that of CFT4. As seen in Figure 4.8, the steel tube picked up load that had been previously supported by the concrete core, resulting in a more rounded load distribution curve and shifting more of the load transfer toward the concrete-loaded end of the CFT. A possible explanation for this observation is that as the steel tube separated from the concrete core at the steel-loaded end, the bond between the two materials was broken and load transfer became more effective along the interface near the center of the CFT. This region of bond slip in CFT3 corresponds to the same location where bond stresses had increased in previous increments of load.

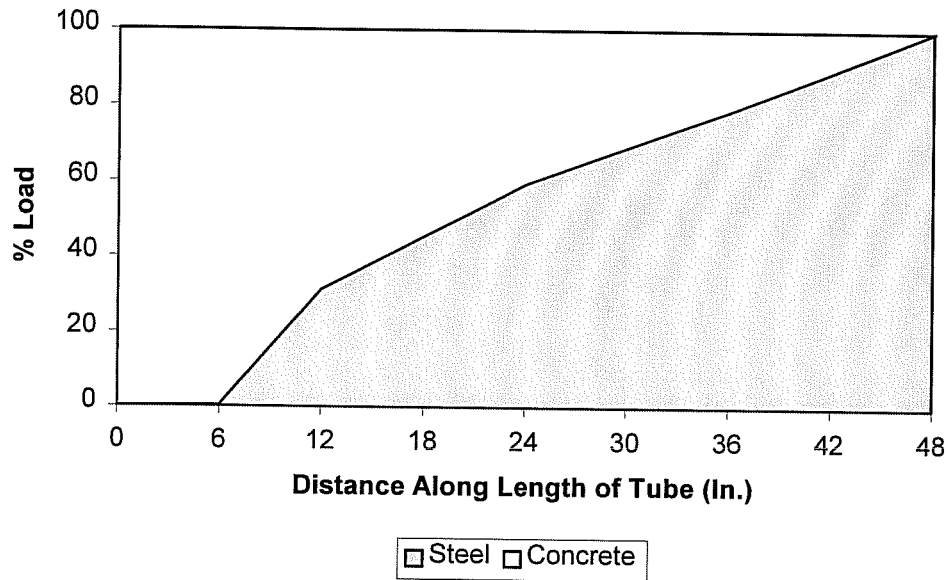


Figure 4.8. Percentage of applied axial load resisted by the steel tube and the concrete core along the length of CFT3 at $P = 1.00 P_{max}$.

The proportion of load resisted by the steel and the concrete after gross slip of the infilled concrete had commenced can provide insight into the load transfer mechanism of the CFT. Figure 4.9 shows the instantaneous distribution of load along the length of CFT4 subsequent to the peak load. This plot represents conditions at a point on the load-slip curve which was located on the plateau of nearly constant load. Similar to the behavior before the peak indicated in Figure 4.7, the load transfer after the peak was evenly distributed along the length of the specimen. However, the jagged distribution of load reveals some localized variation that may be attributed to wedging of the concrete core at steel irregularities inside the steel tube.

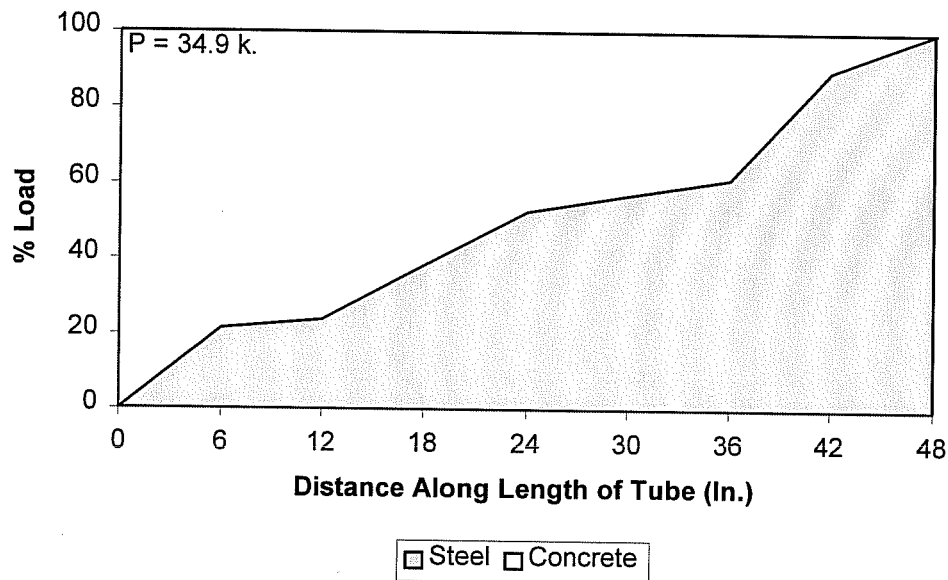


Figure 4.9. Percentage of applied axial load resisted by the steel tube and the concrete core along the length of CFT4 after the peak.

Distribution of Bond Slip

Bond slip can be indirectly determined at any transverse plane along the length of the interface by taking the difference in the displacement between the steel and the concrete at the desired plane relative to some reference plane. This displacement may be expressed as the differential elastic shortening of the steel and the concrete. The first step in calculating bond slip is to select a reference plane of zero slip and the plane at which measurement of bond slip is desired. Next, integration of the steel and concrete strain functions provides the relative elastic shortening of each CFT component. (The strain distribution functions are the same as the load distribution functions presented in the previous section divided by the area and the elastic modulus of each steel or concrete component.) The difference between these displacements, or the differential elastic shortening, is thus a measure of the bond slip between the reference location and the given plane. Since the distribution of load within a specimen is constantly changing, a load-slip analysis must be performed using incremental loads. Cumulative bond slips are obtained by summing incremental values.

The reference plane should represent a location along the length of the specimen where the steel-concrete bond remains intact. As seen in the previous section, the transfer of load initiated at the ends of CFT4 and progressed towards the center of the interface. A logical choice for the plane of zero slip would be a central location that maintained bond until gross slip of the concrete occurred at the peak load. Examination of strains measured at a cross-section located 24 inches from either end as the load increased from zero to the peak value indicated that the steel strains and the concrete strain were approximately equal over this interval. Concrete and steel strains that were nearly equal imply good bond at this location. Therefore, a plane 24 inches from the either end was selected as the reference plane of zero slip for CFT4.

The elastic shortening of the steel tube and concrete core for CFT4 are presented in Figures 4.10 through 4.13. Figure 4.10 shows the distribution of cumulative elastic shortening along the length of the CFT up to an applied load of $0.25 P_{max}$. As in Figures 4.4 through 4.7, the distances plotted on the x-axis are measured relative to the concrete-loaded end. In this figure, little bond slip is evident, as the shortening of the steel and the concrete are nearly equal.

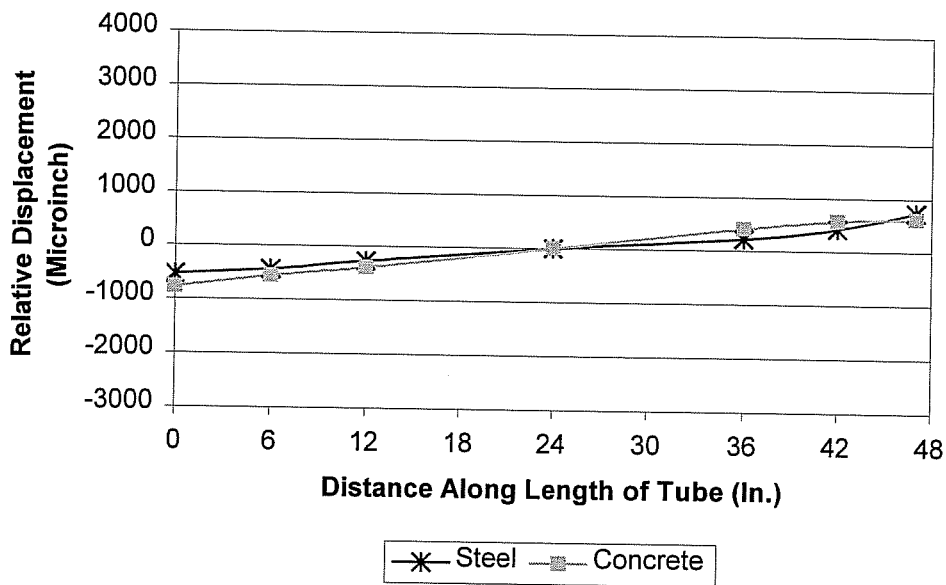


Figure 4.10. Elastic shortening of steel and concrete in CFT4 at $P = 0.25 P_{max}$.

In Figure 4.11, the cumulative elastic shortenings of the steel and the concrete are shown at an applied load of $0.51 P_{max}$. The diverging steel and concrete curves indicate differential shortening along lengths of interface between planes located from zero to 6 inches and from 41 to 48 inches relative to the concrete-loaded end. A comparison of Figure 4.11 to Figure 4.5 (the plot of load distribution at the same applied load) indicates that the region where most of the load transfer occurred generally corresponds to the region of greatest bond slip for the same load. It is likely that high bond stresses led to bond slip at these locations.

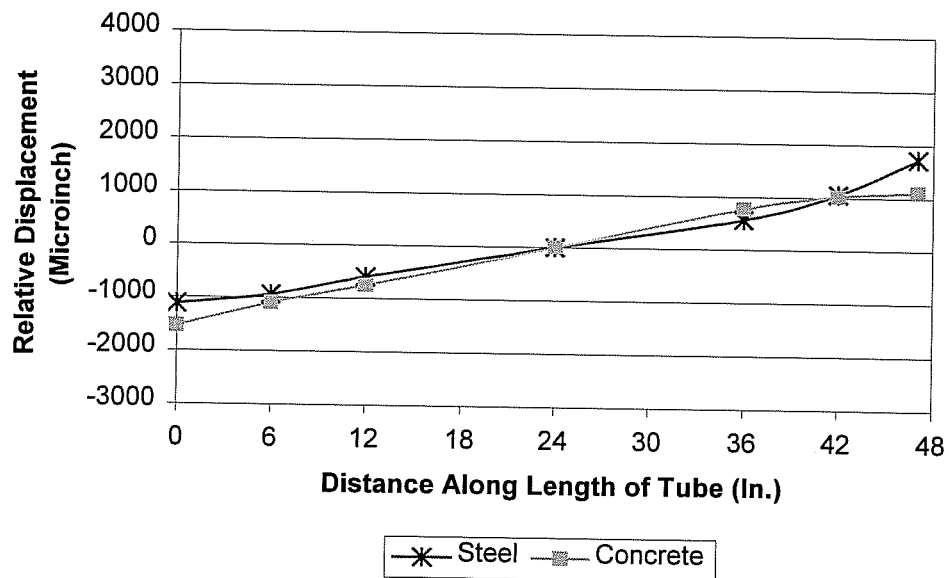


Figure 4.11. Elastic shortening of steel and concrete in CFT4 at $P = 0.51 P_{max}$.

Figure 4.12 shows cumulative elastic shortening of the steel and concrete at an applied load of $0.72 P_{max}$. Bond slip can be observed over the lengths of the interface from zero to 6 inches and from 38 to 48 inches. Thus, as the load transfer expanded toward the center of the tube, the area of bond slip did also.

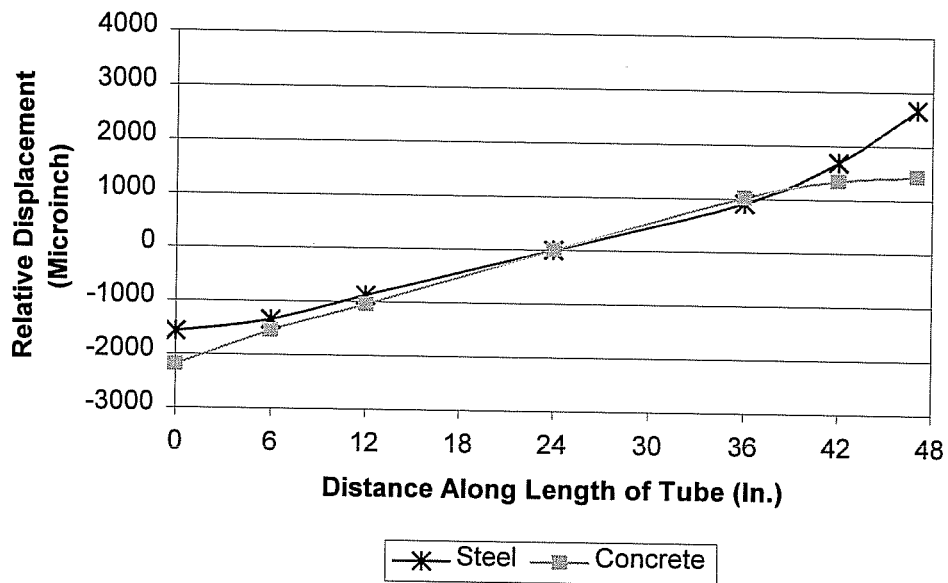


Figure 4.12. Elastic shortening of steel and concrete in CFT4 at $P = 0.72 P_{max}$.

At an applied load of $0.88 P_{max}$ (Figure 4.13), bond slip occurred in CFT4 from zero to 6 inches and from 35 to 48 inches relative to the concrete-loaded end. The sequence of events represented by Figures 4.10 to 4.13 shows the progress of bond slip from the ends toward the center of the CFT until slip became general at P_{max} .

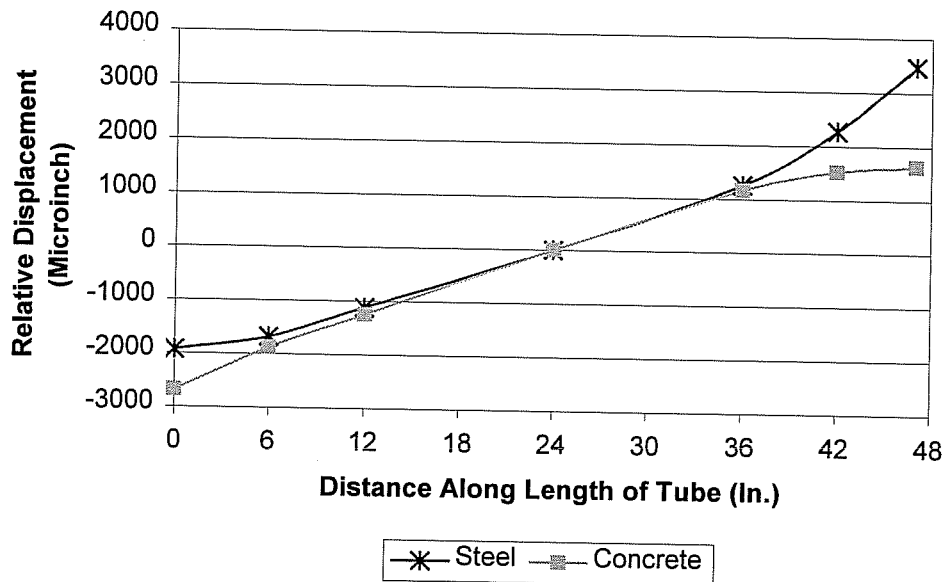


Figure 4.13. Elastic shortening of steel and concrete in CFT4 at $P = 0.88 P_{max}$.

EXPERIMENTAL BEHAVIOR OF 8-IN. CFT'S WITH SHEAR TABS

Load - Slip Response

The load-slip responses of CFT2 and CFT5 (Figure 4.14) resembled those of specimens CFT3 and CFT4, also 8-in. CFT's. The initial stiffnesses of CFT2 and CFT5 were 5650 kips/inch and 10,000 kips/inch, respectively. CFT2 attained a peak load of 98 kips (P_{max}) before initiation of gross slip of the concrete core, while P_{max} for CFT5 was 101 kips. After the peak, the reduction in the loads supported by these CFT's was gradual, similar to the responses of CFT3 and CFT4. However, unlike the behavior of those specimens, the load-slip responses of CFT2 and CFT5 did not approach a plateau of large slips at a nearly constant load. Rather, the loads on the specimens decreased from the peak, reached some minimum value, and began to increase steadily through about an inch of further displacement. It is likely that deformations of the steel tubes caused by rotation of the shear tabs contributed to increased wedging of the concrete cores, and, consequently, to the increased loads supported by the CFT's as the concrete cores were pushed through the tubes. The effective load ranges during slip of the infilled concrete core were 67 to 73 kips for CFT2 and 60 to 71 kips for CFT5.

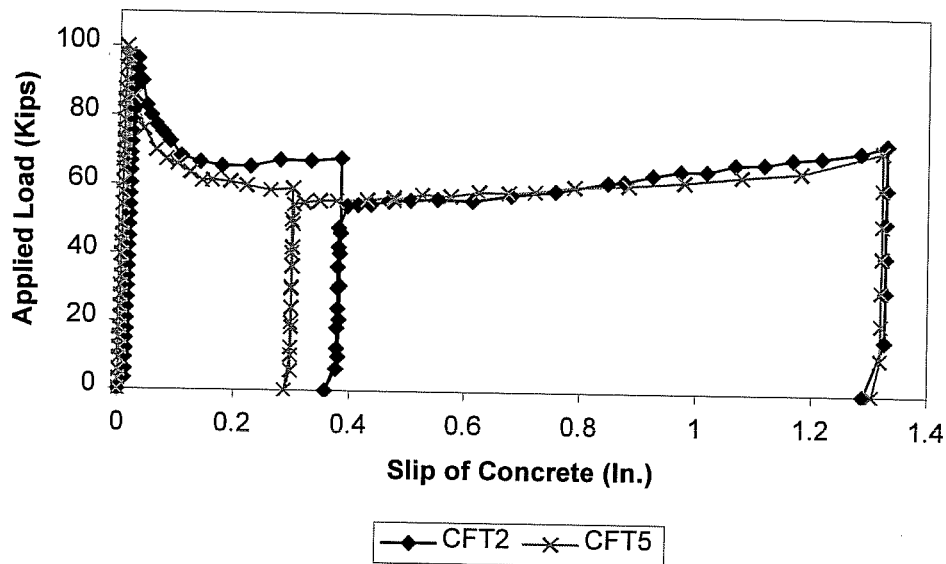


Figure 4.14. Applied axial load vs. slip of the infilled concrete for CFT2 and CFT5.

Specimens CFT2 and CFT5 were also unloaded and reloaded after experiencing some measurable displacement of the concrete core. The reloading stiffness was 12,500 kips/inch for CFT2, or 220% of the initial stiffness. Similarly, CFT5 had a high reloading stiffness, at 16,600 kips/inch. It is likely that rotation of the shear tabs had a pinching effect on the infilled concrete, offering increased resistance to slip during reloading.

Distribution of Longitudinal Shearing Stresses

Again, due to similarities in the behavior of CFT2 and CFT5, only the results of CFT2 are presented here.

Figures 4.15 through 4.18 show the load distributions to the steel and the concrete at applied loads ranging from $0.24 P_{max}$ to $0.95 P_{max}$. In Figure 4.15, at a load of $0.24 P_{max}$, the load transfer occurred primarily at the ends of the specimen, from zero to 12 inches and from 36 to 48 inches relative to the concrete-loaded end. In Figure 4.16, which shows the load distribution at an applied load of $0.49 P_{max}$, the transfer of some load shifted toward the center of the tube. About 50% of the load transfer occurred on an

interface located between 36 and 48 inches, near the shear tabs. At an applied load of $0.74 P_{max}$ (Figure 4.17), the region near the shear tabs still accounted for about 50% of the load transfer from the steel to the concrete. The remainder of the load was transferred at a location 6 to 24 inches relative to the concrete-loaded end. At a load near the peak (Figure 4.18), the load transfer was approximately uniform over an interface length from zero to 42 inches. In other words, all areas of the interface away from the shear tabs contributed equally to the transfer of shear forces. Still, 50 percent of the applied load was transmitted in the six inches of the CFT nearest the steel-loaded end.

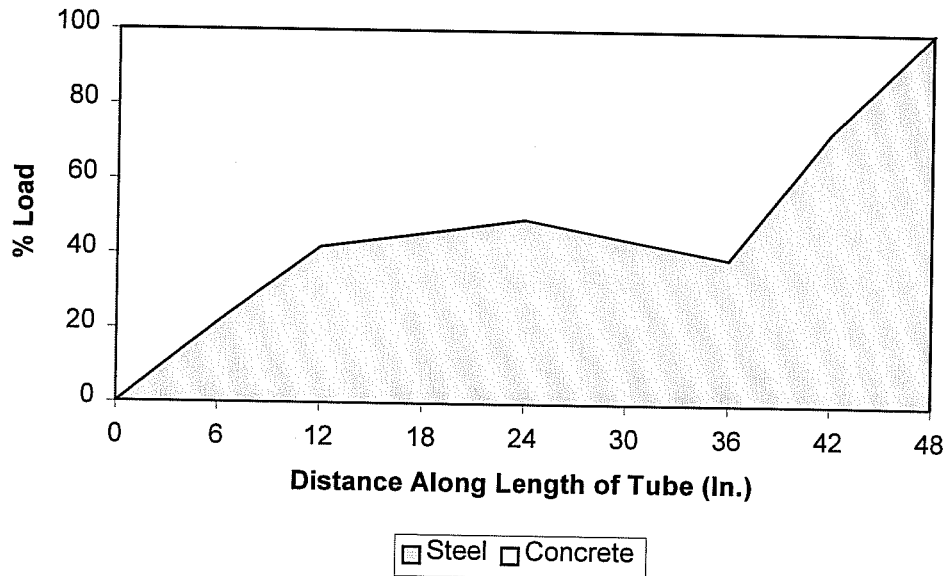


Figure 4.15. Percentage of applied axial load resisted by the steel tube and the concrete core along the length of CFT2 at $P = 0.24 P_{max}$.

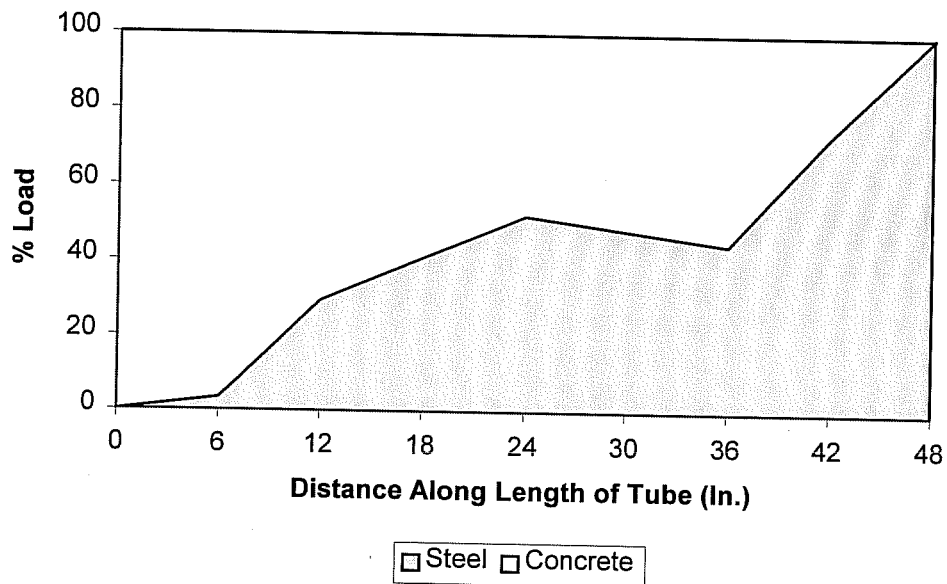


Figure 4.16. Percentage of applied axial load resisted by the steel tube and the concrete core along the length of CFT2 at $P = 0.49 P_{max}$.

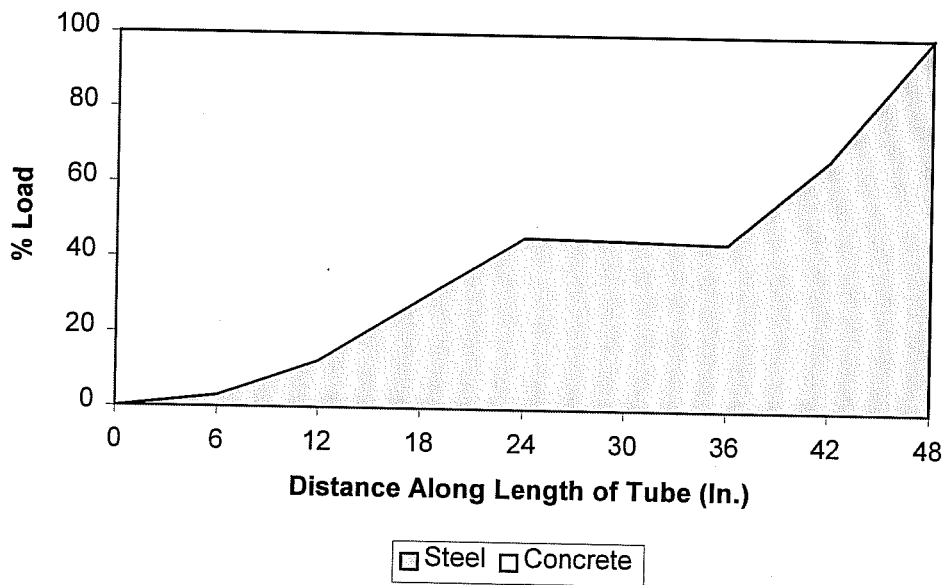


Figure 4.17. Percentage of applied axial load resisted by the steel tube and the concrete core along the length of CFT2 at $P = 0.74 P_{max}$.

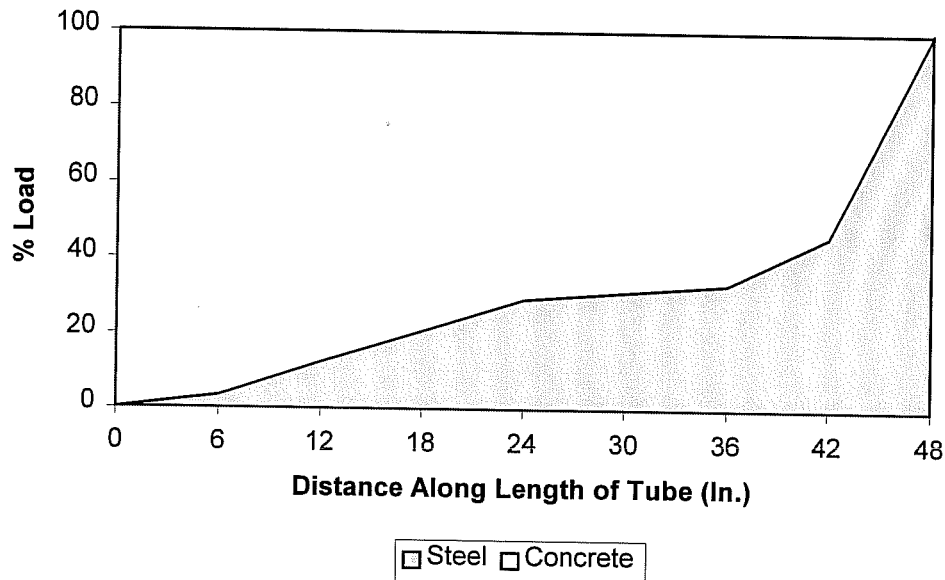


Figure 4.18. Percentage of applied axial load resisted by the steel tube and the concrete core along the length of CFT2 at $P = 0.95 P_{\max}$.

The load distribution curve for CFT2 after the peak load was reached appears similar to that of Figure 4.18, which represents conditions immediately preceding the peak. Figure 4.19 shows the applied load resisted by the steel and the concrete after the peak, at a point on the load-slip curve where the load was decreasing from the peak value. About 70% of the load was transferred along an interface between 36 and 48 inches, near the location of the shear tabs. The load transfer was approximately uniform from zero to 24 inches. The steel load distribution curve shows a localized peak at 24 inches, likely the effect of wedging of the infilled concrete near that location. Wedging action after the peak load is more noticeable in the load distribution curve for CFT5 (Figure 4.20), which also indicates that wedging occurred near a transverse plane located 24 inches from either end.

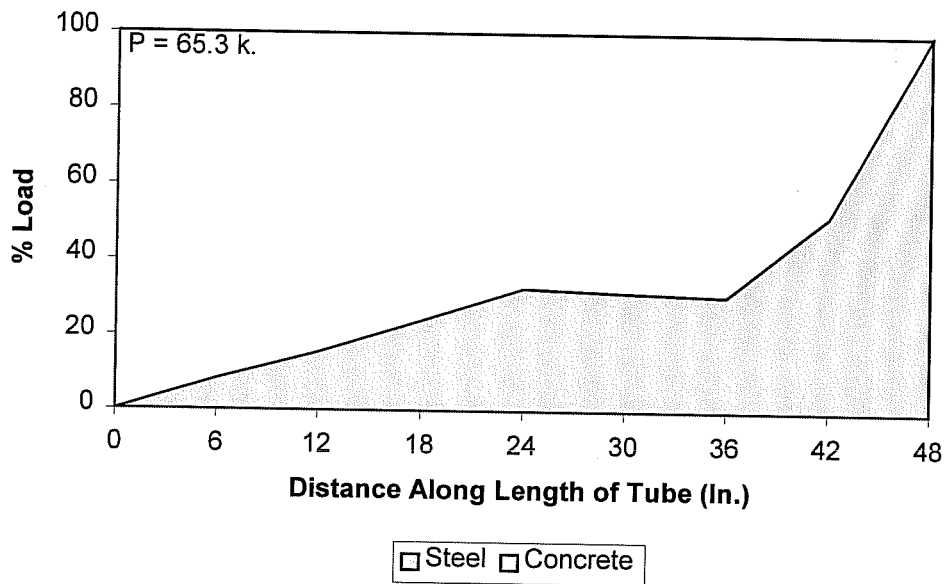


Figure 4.19. Percentage of applied axial load resisted by the steel tube and the concrete core along the length of CFT2 after the peak.

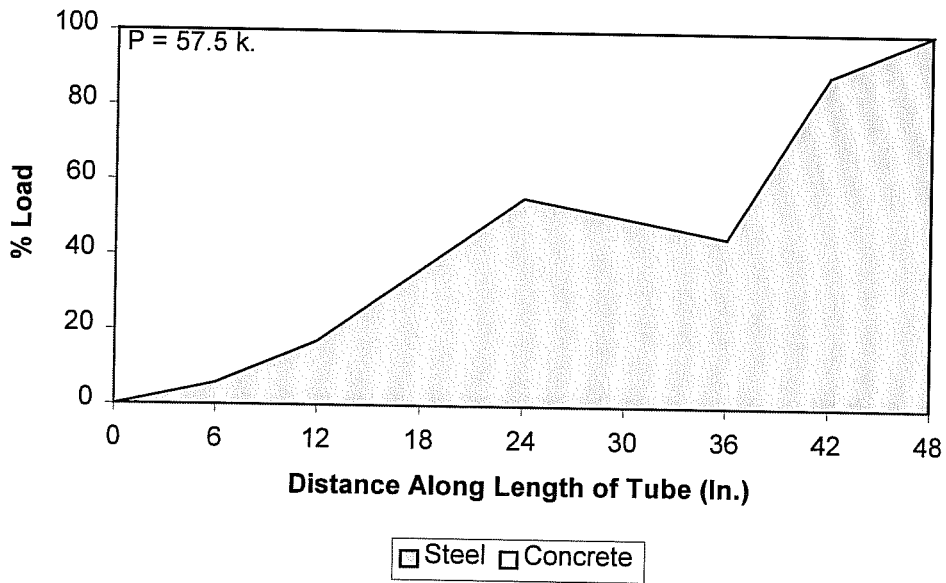


Figure 4.20. Percentage of applied axial load resisted by the steel tube and the concrete core along the length of CFT5 after the peak.

Distribution of Bond Slip

Figures 4.21 through 4.24 in sequence show the progression of bond slip as the load on CFT2 was increased. As in previous specimens, the plane of zero slip was selected as that plane located 24 inches from either end. In Figure 4.21, at an applied load of $0.24 P_{max}$, little elastic shortening of the steel or concrete is evident. At an applied load of $0.49 P_{max}$ (Figure 4.22), differential shortening of the steel and concrete can be seen between planes located at 36 and 48 inches relative to the concrete-loaded end. At an applied load of $0.74 P_{max}$, the areas of bond slip had expanded to include a length of interface from zero to 6 inches at the concrete-loaded end (Figure 4.23). Immediately preceding slip, most of the interface had experienced some bond slip (Figure 4.24). Differential shortening is apparent from zero to 9 inches and from 30 to 48 inches. As in the previous specimens, the area of bond slip moved from the ends of the CFT at low loads towards the midpoint of the interface as the applied load was increased.

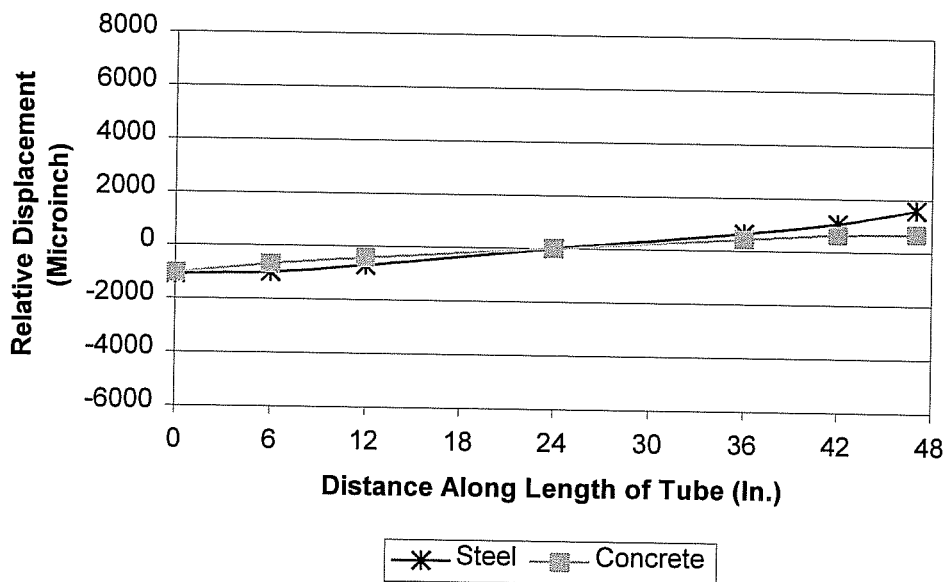


Figure 4.21. Elastic shortening of steel and concrete in CFT2 at $P = 0.24 P_{max}$.

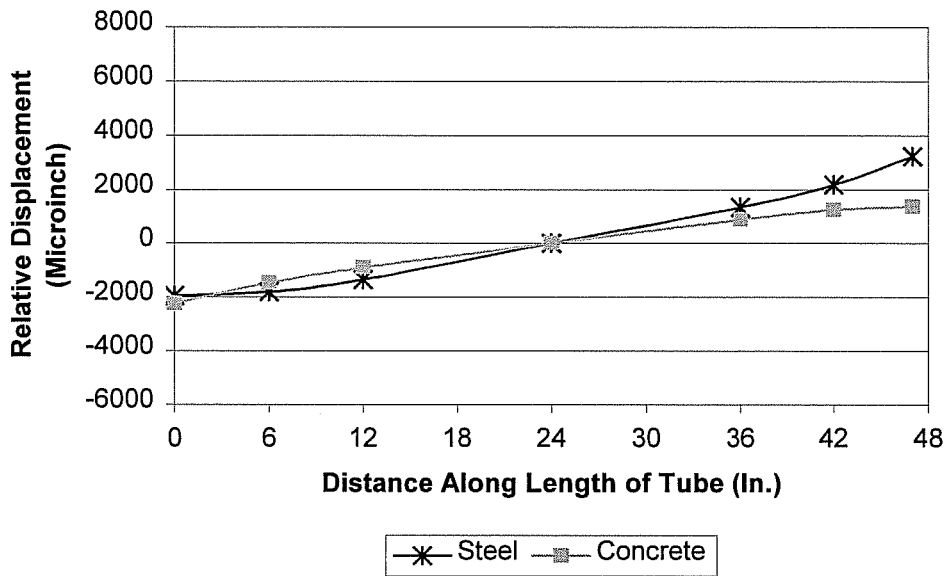


Figure 4.22. Elastic shortening of steel and concrete in CFT2 at P = 0.49 P_{max}.

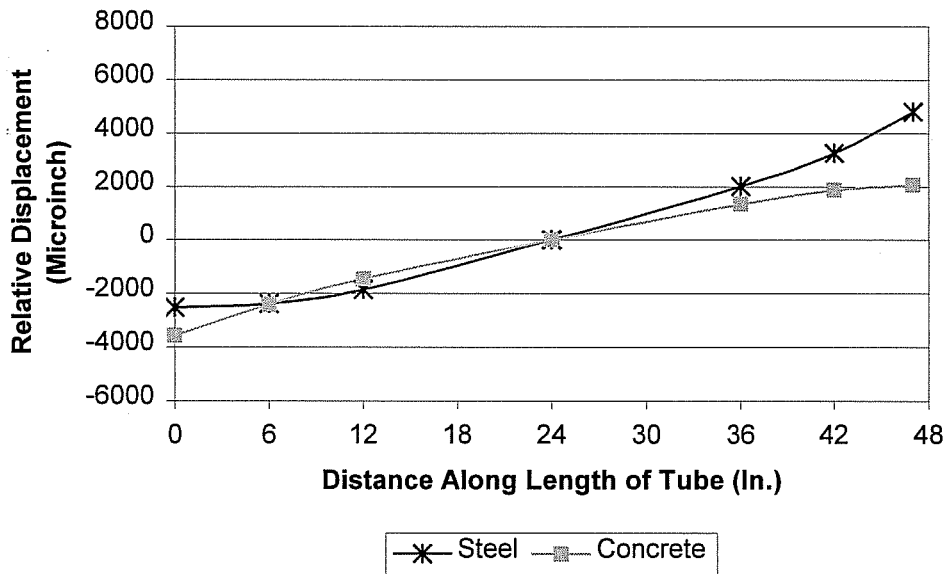


Figure 4.23. Elastic shortening of steel and concrete in CFT2 at P = 0.74 P_{max}.

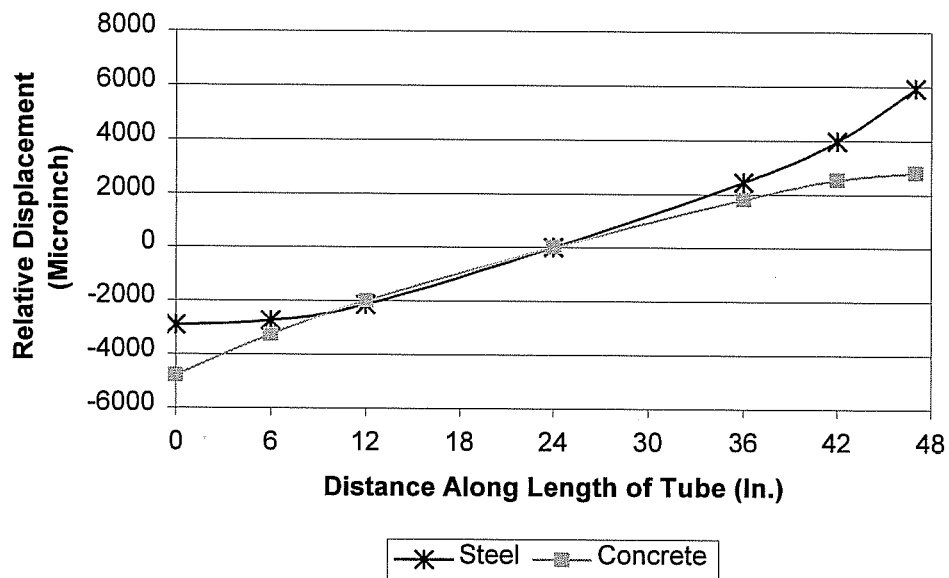


Figure 4.24. Elastic shortening of steel and concrete in CFT2 at $P = 0.95 P_{max}$.

Photographic Evidence of Shear Tab Deformation

Photographs taken before and after testing provide some insight into the deformations of the steel tube that occurred near the shear tabs. Figure 4.25 shows an 8-in. CFT with shear tabs prior to the experiment. Heat-related deformations due to the welding process can be seen in the out-of-straightness of the tube walls near the shear tabs. In Figure 4.26, the gap that had formed between the steel tube and the concrete offers evidence of the effects of shear tab rotation in the 8-in. specimens during testing. In contrast, in Figure 4.27 less deformation is visible in an 8-in. steel tube without shear tabs after testing.

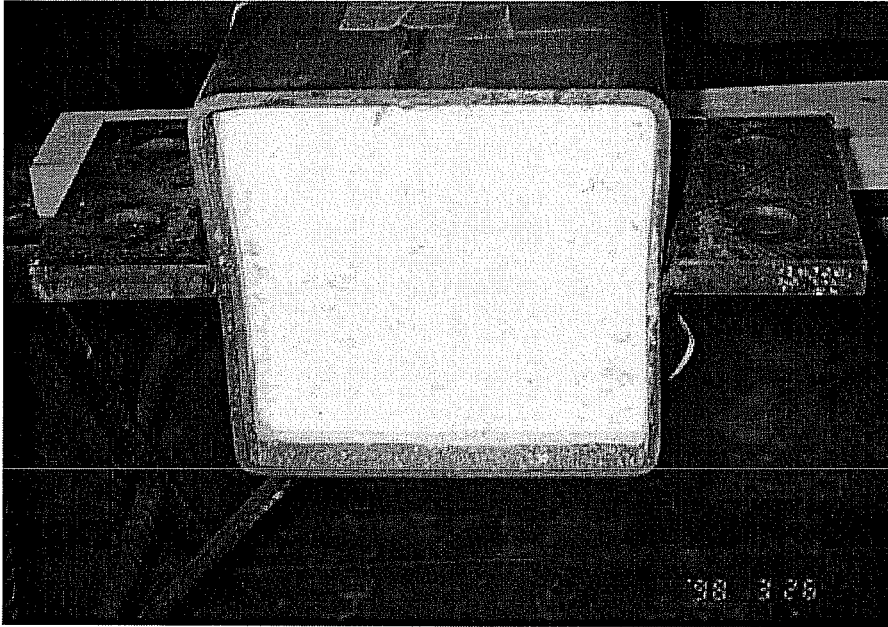


Figure 4.25. 8-in. CFT with shear tabs before testing.

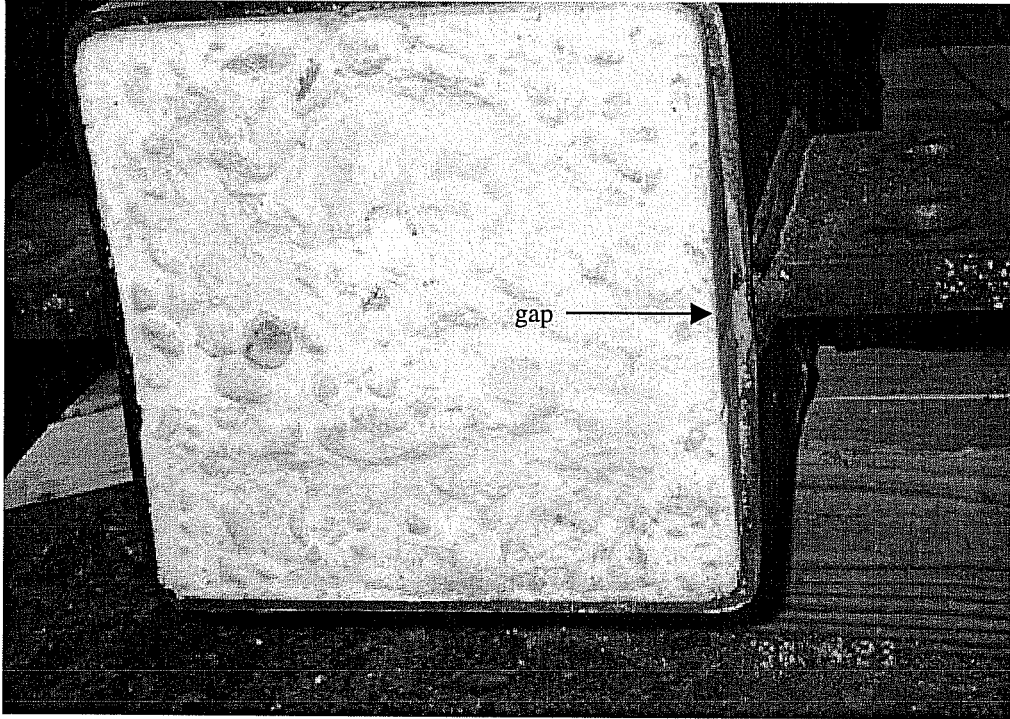


Figure 4.26. 8-in. CFT with shear tabs after testing.

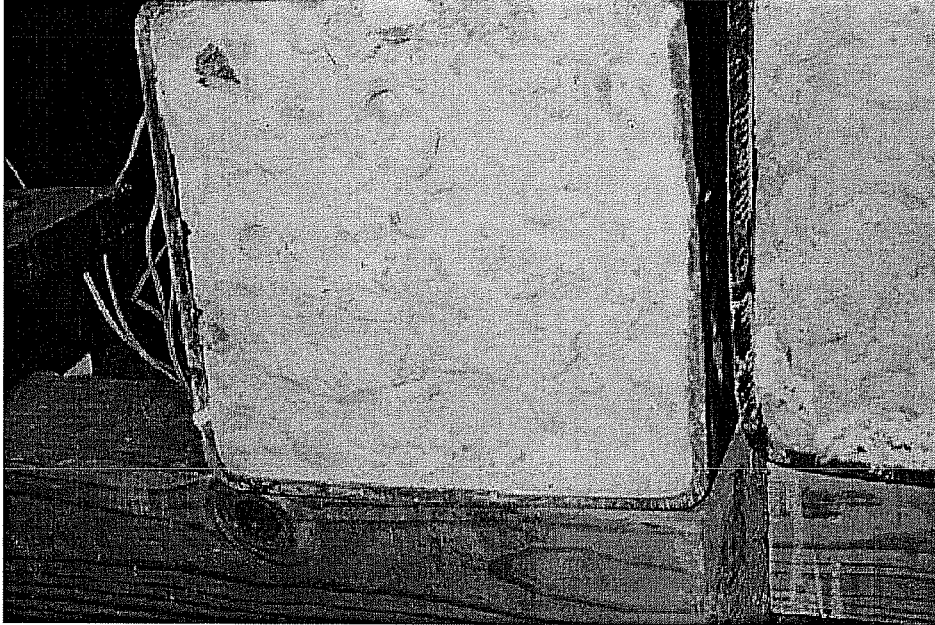


Figure 4.27. 8-in. CFT without shear tabs after testing.

EXPERIMENTAL BEHAVIOR OF 10-IN. CFT'S WITHOUT SHEAR TABS

Load - Slip Response

Although most of the behavioral characteristics of the 10-in. CFT's resemble those of the smaller specimens, the load-slip responses of CFT7 and CFT1 show some attributes that pertain to the larger CFT's only. CFT7 had an initial stiffness of 13,100 kips/inch, while for CFT1 the stiffness was 37,000 kips/inch. After the peak load was reached, CFT7 and CFT1 experienced rather large reductions in the load supported by the interface (Figure 4.28). For CFT7, the applied load dropped suddenly from 61 kips at the peak (P_{max}) to 40 kips thereafter. In CFT1, the applied load dropped from a peak load of 57 kips (P_{max}) to 41 kips. These reductions in load were also accompanied by loud "bang" sounds as the CFT's released some energy that had previously been stored in the steel-concrete bond.

After the peaks, the displacements along the steel-concrete interface began to increase. The loads that the CFT's were able to support increased slightly, by as much as 6 kips, before settling into a relatively constant load of 41 kips for both specimens. Most of the slip of the infilled concrete occurred along this plateau of nearly constant load.

When the load-slip responses reached this plateau, the load was removed and reapplied. The reloading stiffness of CFT7 was 11,100 kips/inch. For CFT1, the reloading stiffness was calculated as 22,500 kips/inch, or 61% of the initial stiffness. This loss in stiffness after the peak load can be attributed to the loss of adhesion along the interface and to separation of the steel from the concrete near the steel-loaded end.

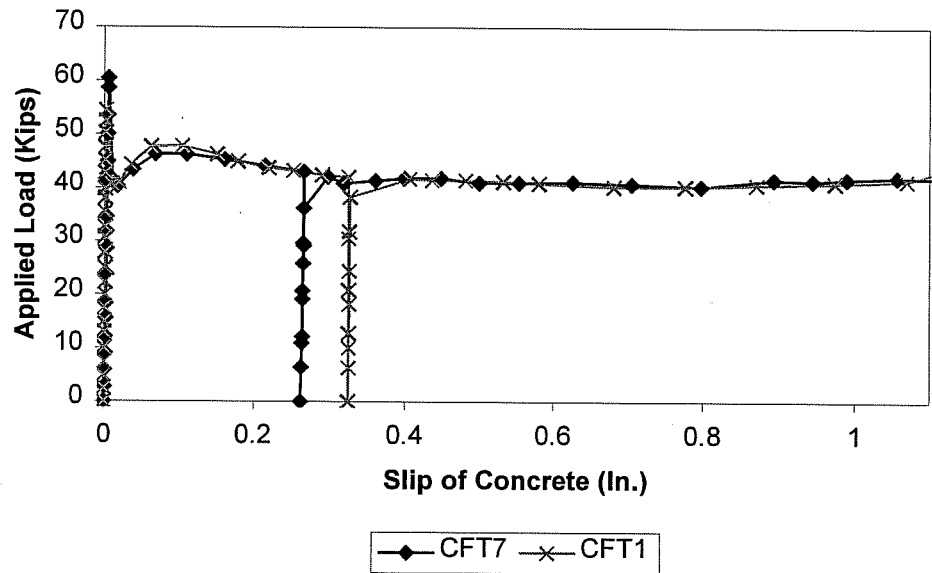


Figure 4.28. Applied axial load vs. slip of the infilled concrete for CFT7 and CFT1.

Distribution of Longitudinal Shearing Stresses

In the following sections, only the behavior of CFT7 is discussed since it is typical of both 10-in. CFT's without shear tabs.

Figure 4.29 shows the percentage of applied load resisted by the steel and by the concrete at an applied load of $0.26 P_{max}$. Like the four 8-in. specimens, CFT7 transferred most of the load from the steel to the concrete at the ends of the specimen, from zero to 7.5 inches and from 45 to 60 inches relative to the concrete-loaded end. On the other hand, the behavior of CFT7 began to vary from those of the previous specimens as the load increased. In particular, Figures 4.30 through 4.32 show that the steel tube supported more load relative to the concrete as the applied load increased. In Figure

4.30, at an applied load of $0.52 P_{max}$, the length of steel tube located 30 to 60 inches relative to the concrete-loaded end resisted an increased percentage of load. A likely cause of this behavior was the breaking of bond near the steel-loaded end that made the transfer of load to concrete at this location more difficult. Therefore, the transfer of load moved toward the concrete-loaded end. Figure 4.31 shows that at an applied load of $0.74 P_{max}$, the steel tube along the entire length of the specimen continued to pick up load from the concrete. Just prior to the peak, most of the load transfer in CFT7 occurred along the interface consisting of the 15 inches nearest the concrete-loaded end (Figure 4.32).

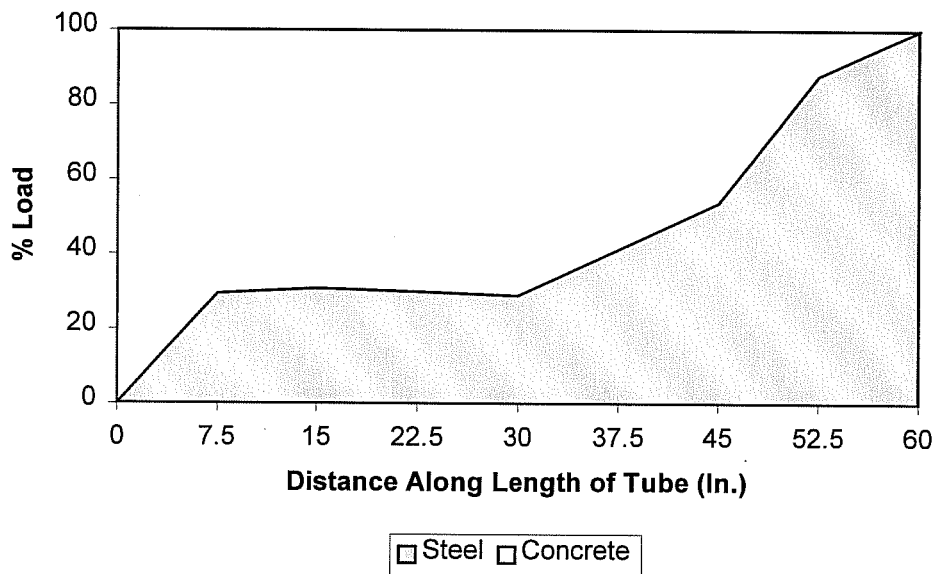


Figure 4.29. Percentage of applied axial load resisted by the steel tube and the concrete core along the length of CFT7 at $P = 0.26 P_{max}$.

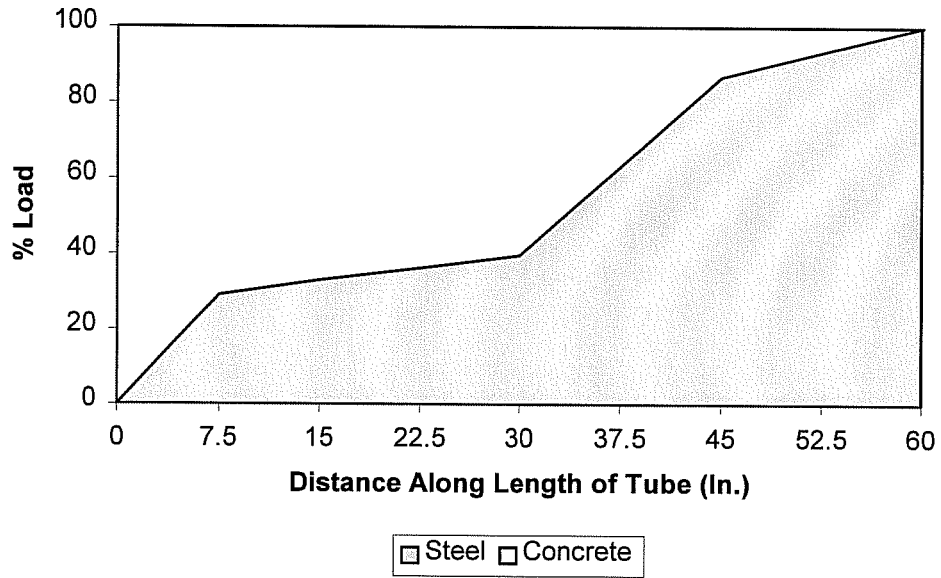


Figure 4.30. Percentage of applied axial load resisted by the steel tube and the concrete core along the length of CFT7 at $P = 0.52 P_{max}$.

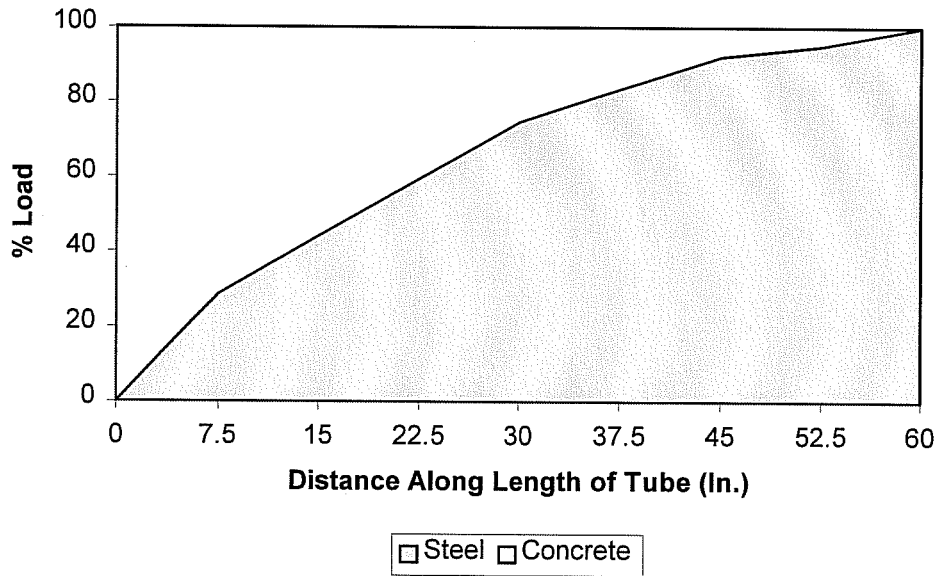


Figure 4.31. Percentage of applied axial load resisted by the steel tube and the concrete core along the length of CFT7 at $P = 0.74 P_{max}$.

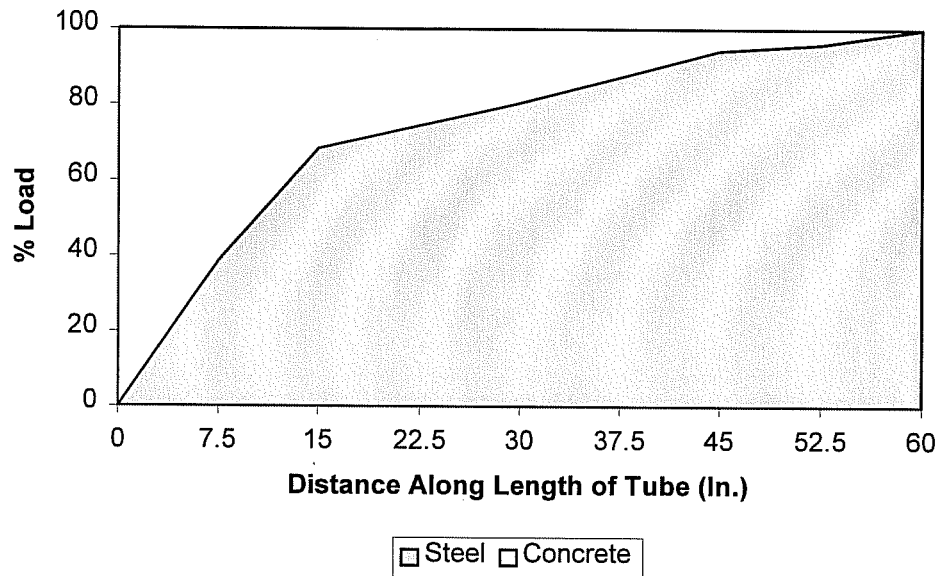


Figure 4.32. Percentage of applied axial load resisted by the steel tube and the concrete core along the length of CFT7 at $P = 0.99 P_{max}$.

After the peak load was reached, the load transfer became more evenly distributed along the length of interface. Figure 4.33 presents the distribution at an applied load of 42 kips. Portions of the interface located from zero to 52.5 inches relative to the concrete-loaded end transferred the load from the steel to the concrete in a nearly uniform manner. No significant load transfer occurred along the 7.5 inches nearest the steel-loaded end, which suggests a separation between the steel and the concrete had occurred there.

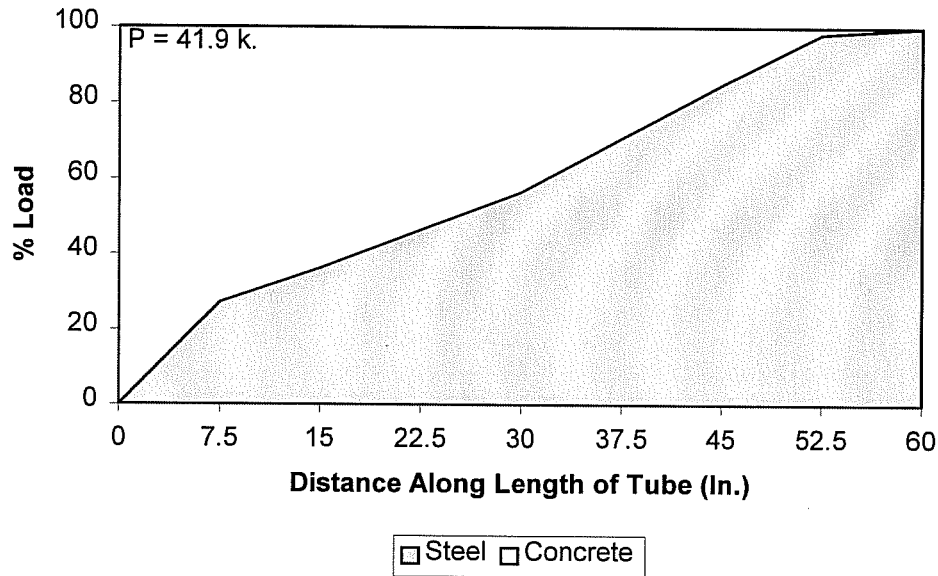


Figure 4.33. Percentage of applied axial load resisted by the steel tube and the concrete core along the length of CFT7 after the peak.

Distribution of Bond Slip

Before the distribution of bond slip could be determined for the 10-in. CFT's, the reference plane of zero slip had to be located. Separation of the steel tube from the concrete core that likely occurred near the steel-loaded end shifted the area of load transfer towards the concrete-loaded end, and, thus, would likely also move the transverse reference plane from the centerline towards the concrete-loaded end. Compatibility of steel and concrete strains at a cross-section located 15 inches from the concrete-loaded end confirmed that the bond remained intact at this plane prior to the peak load.

Figure 4.34 shows the elastic shortening of the steel and the concrete at an applied load of $0.26 P_{max}$. Little bond slip is apparent at this low load. In Figure 4.35, differential shortening of the steel and concrete is evident along a length of interface from 44 to 60 inches at an applied load of $0.52 P_{max}$. At $0.74 P_{max}$, bond slip occurred along an interface located 34 to 60 inches from the concrete-loaded end (Figure 4.36).

Immediately preceding the peak load, CFT7 experienced bond slip over the two thirds of the interface nearest the steel-loaded end (Figure 4.37).

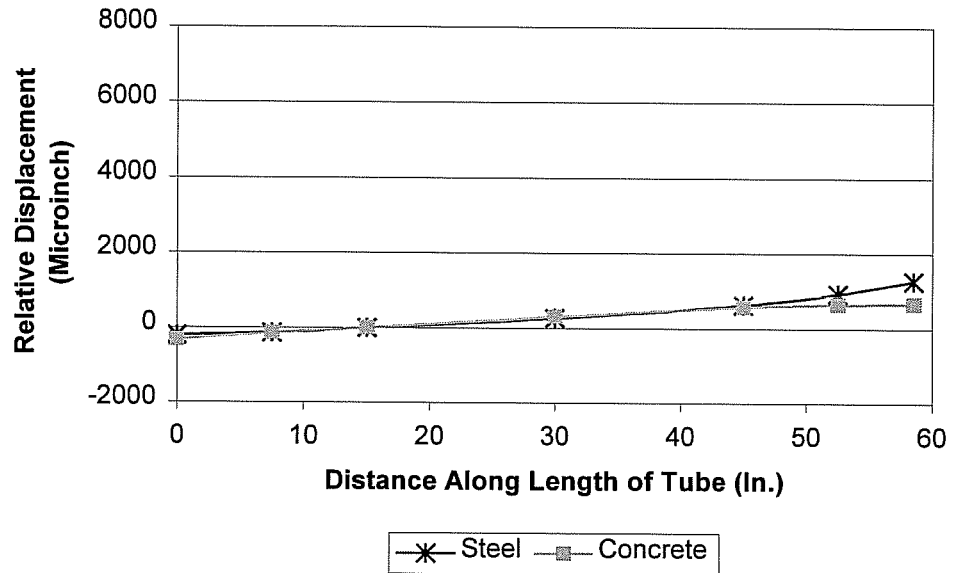


Figure 4.34. Elastic shortening of steel and concrete in CFT7 at $P = 0.26 P_{max}$.

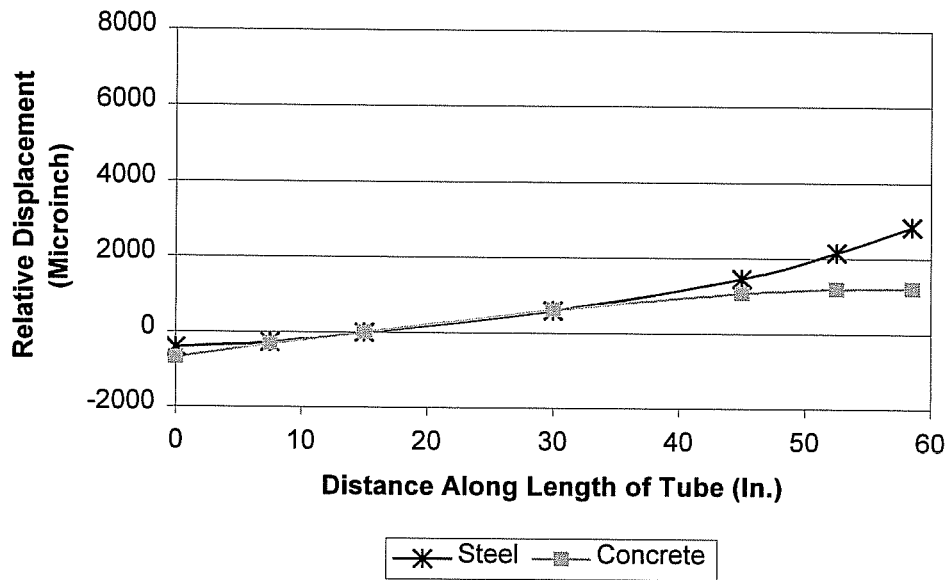


Figure 4.35. Elastic shortening of steel and concrete in CFT7 at $P = 0.52 P_{max}$.

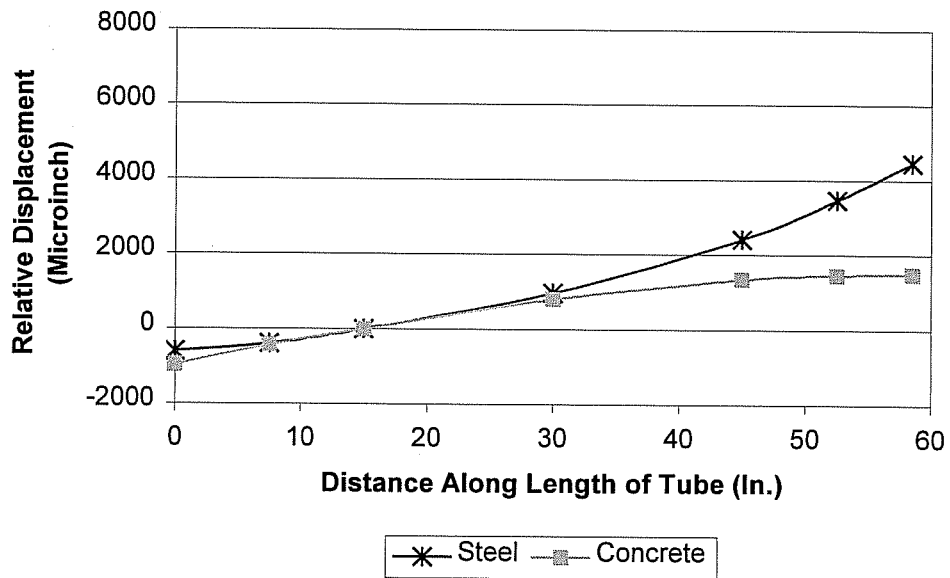


Figure 4.36. Elastic shortening of steel and concrete in CFT7 at $P = 0.74 P_{max}$.

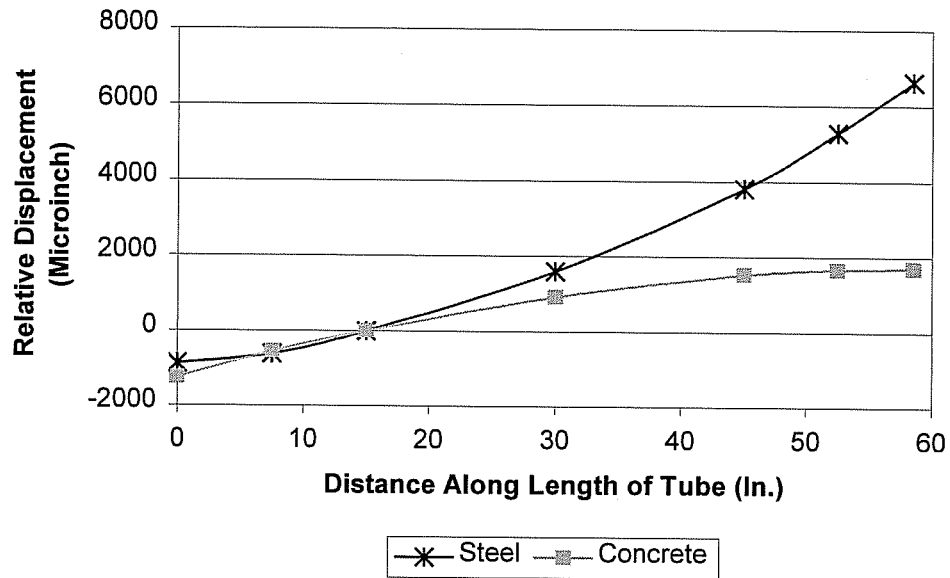


Figure 4.37. Elastic shortening of steel and concrete in CFT7 at $P = 0.99 P_{max}$.

EXPERIMENTAL BEHAVIOR OF 10-IN. CFT'S WITH SHEAR TABS

Load – Slip Response

The load-slip responses of CFT8 and CFT6 up to the peak load resembled those of specimens CFT7 and CFT1. Initial stiffnesses of 19,800 kips/inch for CFT8 and 12,900 kips/inch for CFT6 were consistent with those of the other 10-in. CFT's. For CFT8, after a peak load of 67 kips (P_{max}) was attained, the load dropped immediately to about 47 kips (Figure 4.38). Similarly, for CFT6, the load supported by the interface dropped sharply from a peak value of 70 kips (P_{max}) to about 56 kips. The post-peak load behavior distinguished these 10-in. specimens with shear tabs from the other specimens. From a minimum load after the peak, the load on each gradually increased until a plateau was reached. The load-slip curves show a distinct plateau of increasing displacements at a nearly constant load of 60 kips for CFT8 and 63 kips for CFT6.

The reloading cycles for CFT8 and CFT6 occurred on this plateau of constant load and increasing displacements. The reloading stiffnesses were calculated as 17,000 kips/inch and 27,900 kips/inch, respectively.

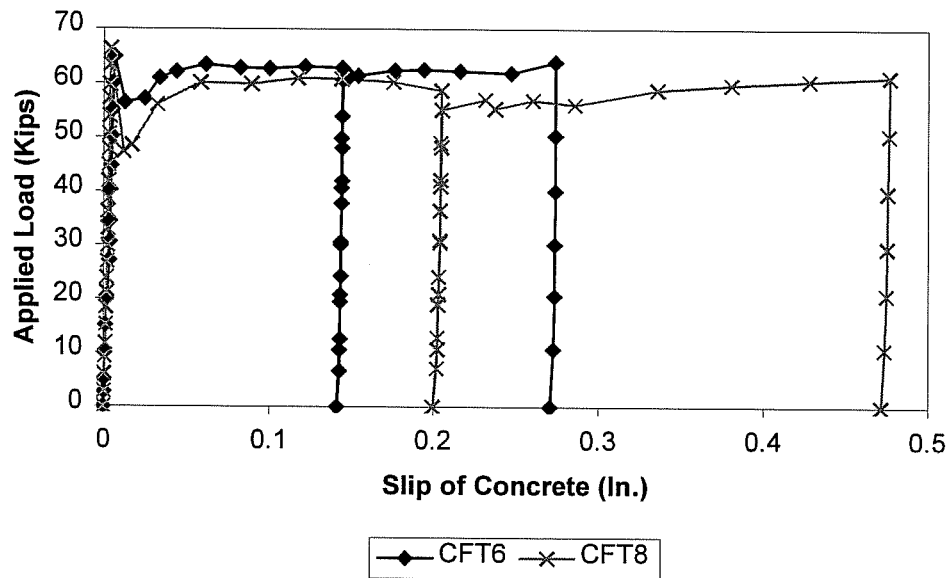


Figure 4.38. Applied axial load vs. slip of the infilled concrete for CFT8 and CFT6.

Distribution of Longitudinal Shearing Stresses

The results of CFT8 exclusively are discussed in the following sections, except where the results of CFT6 differ from those of CFT8.

The effect of the shear tabs is evident in the distribution of load along the length of the tube in CFT8. Figure 4.39 shows the load distribution at an applied load of $0.23 P_{max}$. The transfer of load occurred near the ends of the tube, at lengths of interface from zero to 7.5 inches and from 45 to 60 inches relative to the concrete-loaded end. In Figure 4.40, in which the applied load was $0.49 P_{max}$, nearly half of the load transfer occurred in the vicinity of the shear tabs. At $0.76 P_{max}$, the length of interface nearest the shear tabs still accounted for about 40% of the load transfer (Figure 4.41). The steel tube picked up load that the concrete core had previously supported in the interface area near the center of the tube, resulting in a load transfer which was more evenly distributed along that length of interface. Just prior to the peak, the load supported by the steel tube in the center portion of the interface continued to increase (Figure 4.42). In CFT6, however, the load transfer immediately preceding the peak load had become uniform along a length of interface from zero to 45 inches relative to the concrete-loaded end (Figure 4.43).

Regardless of the load distribution away from the shear tabs, for both CFT8 and CFT6 the length of interface from 45 to 60 inches, near the location of the shear tabs, was responsible for about 50% of the load transfer from the steel to the concrete.

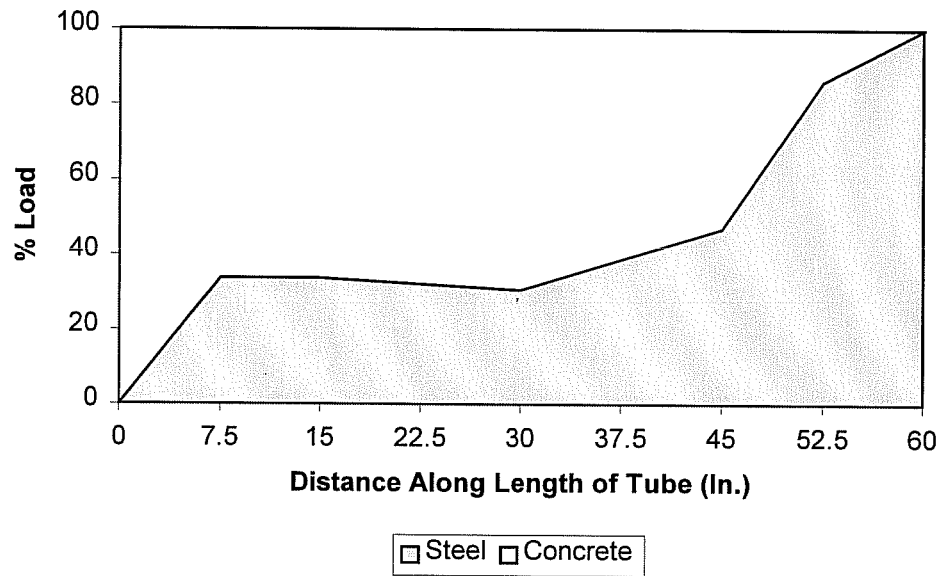


Figure 4.39. Percentage of applied axial load resisted by the steel tube and the concrete core along the length of CFT8 at $P = 0.23 P_{max}$.

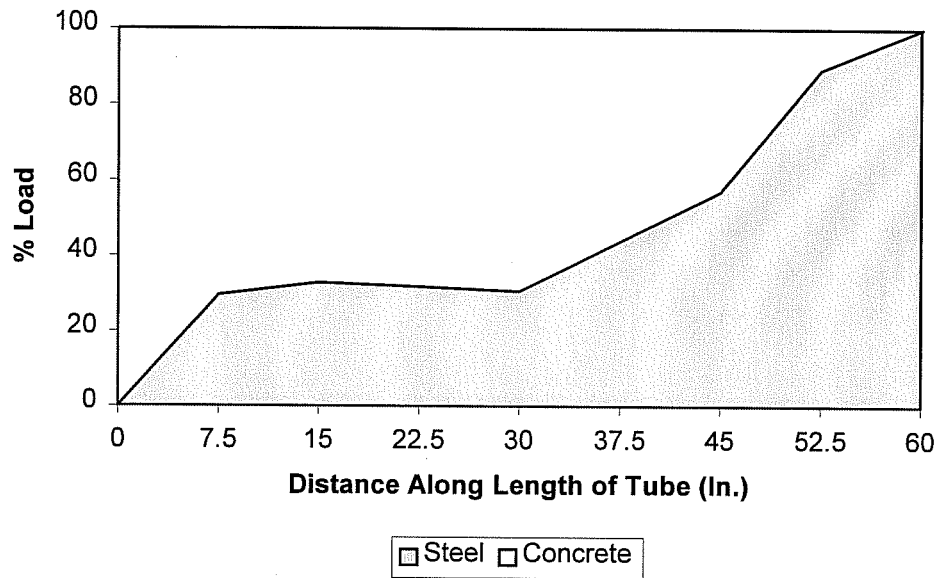


Figure 4.40. Percentage of applied axial load resisted by the steel tube and the concrete core along the length of CFT8 at $P = 0.49 P_{max}$.

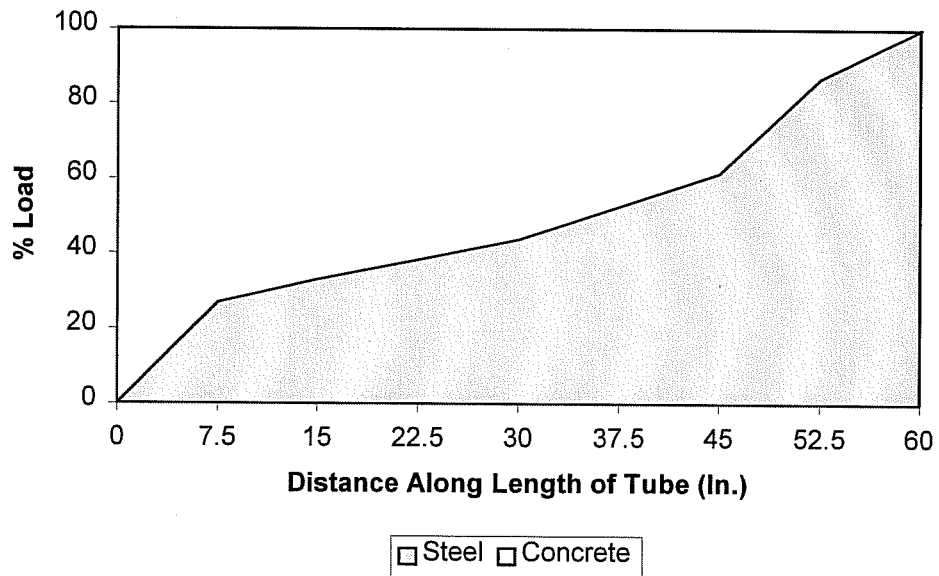


Figure 4.41. Percentage of applied axial load resisted by the steel tube and the concrete core along the length of CFT8 at $P = 0.76 P_{max}$.

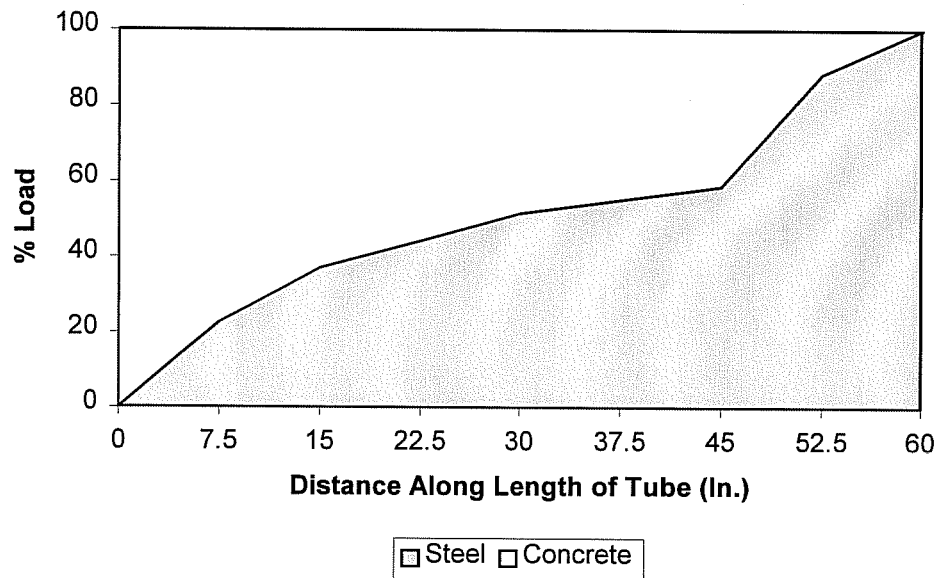


Figure 4.42. Percentage of applied axial load resisted by the steel tube and the concrete core along the length of CFT8 at $P = 0.99 P_{max}$.

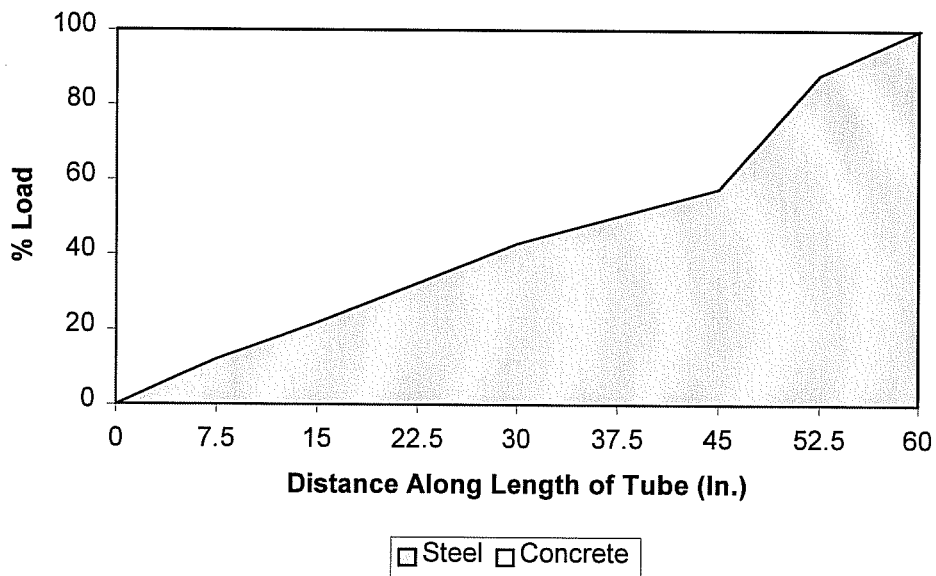


Figure 4.43. Percentage of applied axial load resisted by the steel tube and the concrete core along the length of CFT6 at $P = 0.93 P_{max}$.

After the peak load was reached, the shear tabs had little effect on the load transfer. In Figure 4.44, just after the load had dropped off from the peak value, the slope of the steel load distribution curve was approximately constant over the entire length of interface. Thus, the entire interface, including that portion nearest the shear tabs, was contributing equally to the load transfer. After the load on CFT8 had increased, Figure 4.45 shows that most of the load transfer occurred at a location just above the shear tabs, along a length of interface from 30 to 45 inches. The portion of the interface nearest the shear tabs contributed little to the transfer of load. This behavior contrasts to that of the 8-in. specimens with shear tabs, where the area near the shear tabs continued to transfer about half of the applied load after the peak.

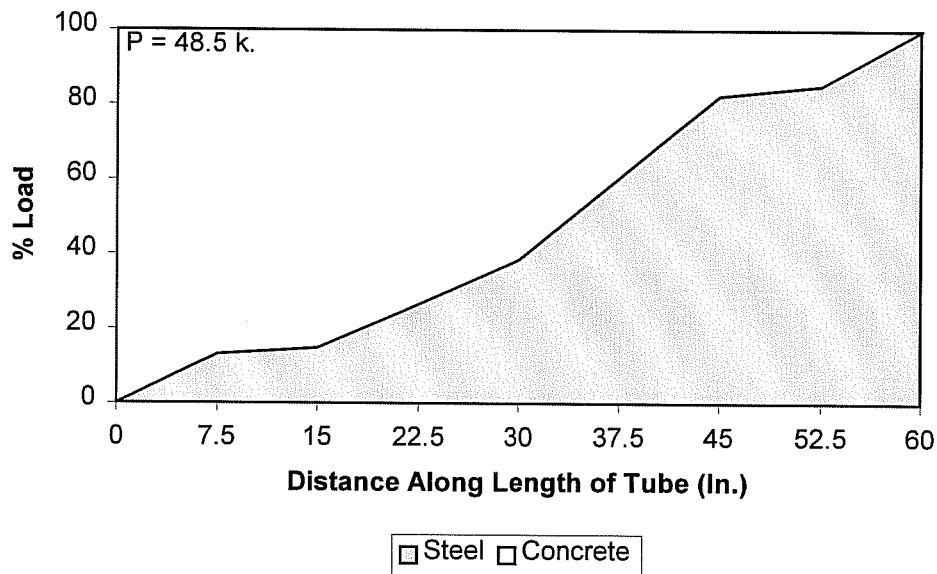


Figure 4.44. Percentage of applied axial load resisted by the steel tube and the concrete core along the length of CFT8 after the peak ($P = 49$ kips).

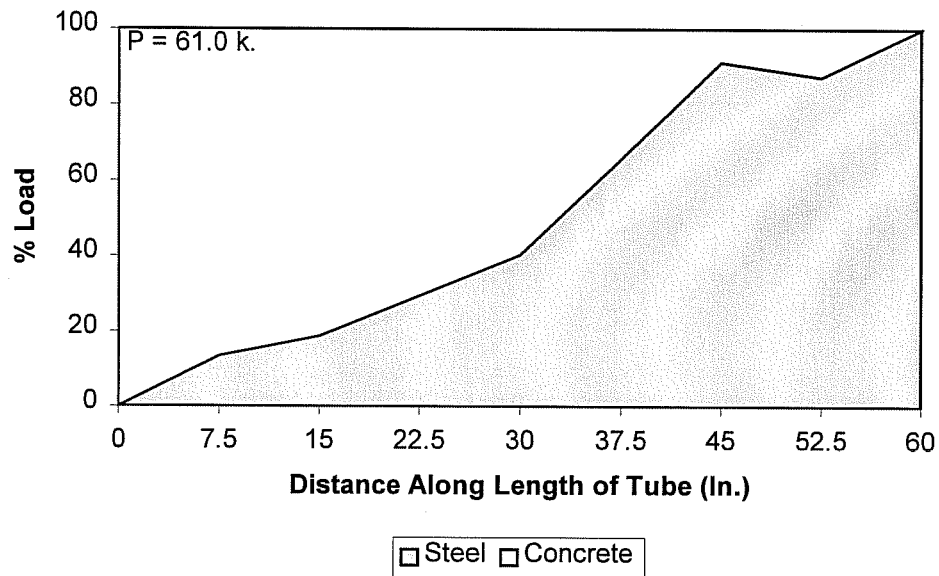


Figure 4.45. Percentage of applied axial load resisted by the steel tube and the concrete core along the length of CFT8 after the peak (P = 61 kips).

In contrast to its companion specimen, CFT6 relied on the portion of the interface nearest the shear tabs to transfer the load from the steel to the concrete after the peak load had been reached. Figure 4.46 indicates uniform transfer of load over the three quarters of interface located nearest the concrete-loaded end. At 62 kips, the load distribution curve shows that almost 50% of the load that was applied to the steel tube had been transferred to the concrete in the 15 inches of interface nearest the steel-loaded end.

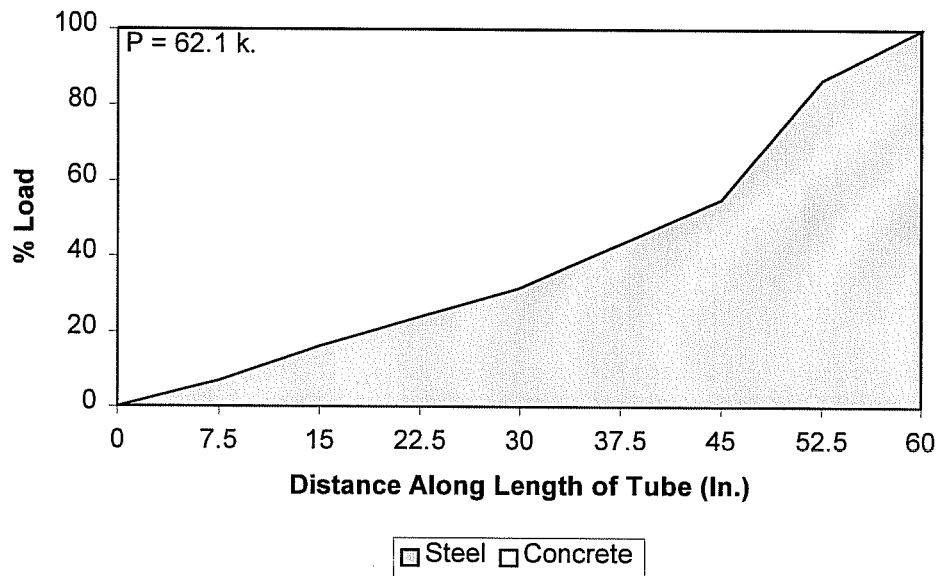


Figure 4.46. Percentage of applied axial load resisted by the steel tube and the concrete core along the length of CFT6 after the peak.

Distribution of Bond Slip

Figures 4.47 through 4.50 show the development of bond slip in CFT8, with a reference plane of zero slip at 15 inches from the concrete-loaded end. In Figure 4.47, at an applied load of $0.23 P_{max}$, no noticeable bond slip had accumulated along the interface. At $0.49 P_{max}$, differential shortening of the steel and the concrete occurred along a length of interface from 47 to 60 inches relative to the concrete-loaded end (Figure 4.48). At $0.76 P_{max}$, the area of bond slip extended two inches in the direction of the concrete-loaded end (Figure 4.49). When compared to the CFT7 and CFT1, CFT8, with the shear tabs, did not develop as much bond slip as the previous specimens without shear tabs. Just prior to the peak, Figure 4.50 shows bond slip along interface lengths from zero to 5 inches and from 33 to 60 inches.

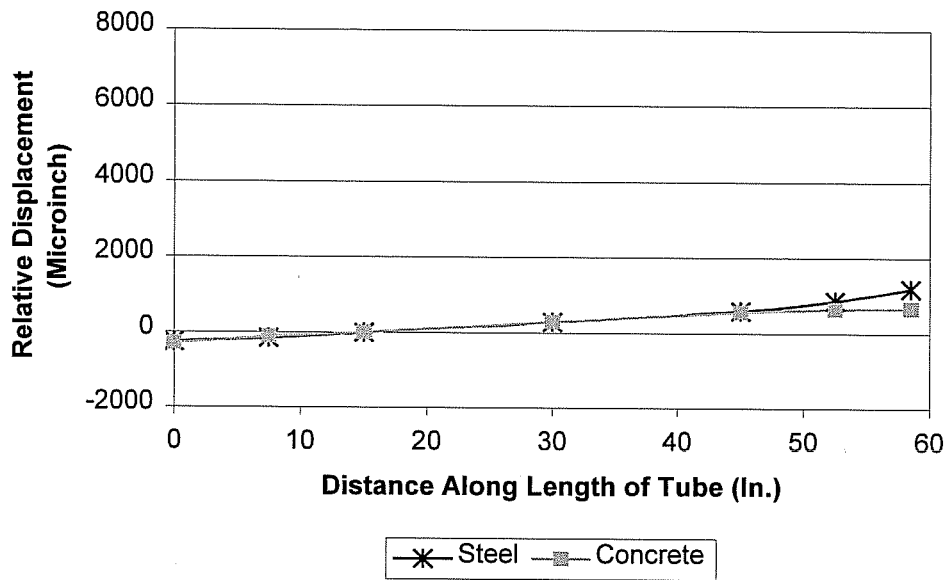


Figure 4.47. Elastic shortening of steel and concrete in CFT8 at $P = 0.23 P_{max}$.

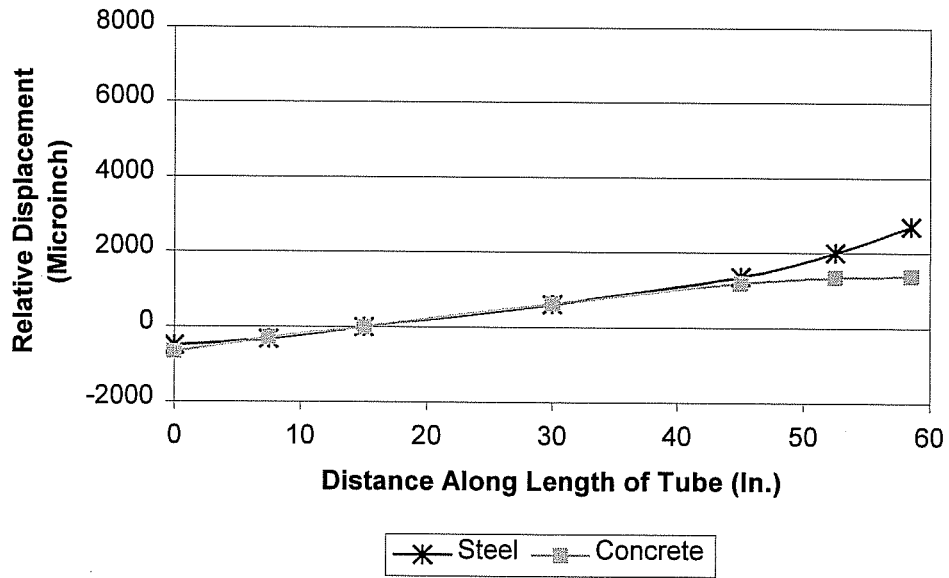


Figure 4.48. Elastic shortening of steel and concrete in CFT8 at $P = 0.49 P_{max}$.

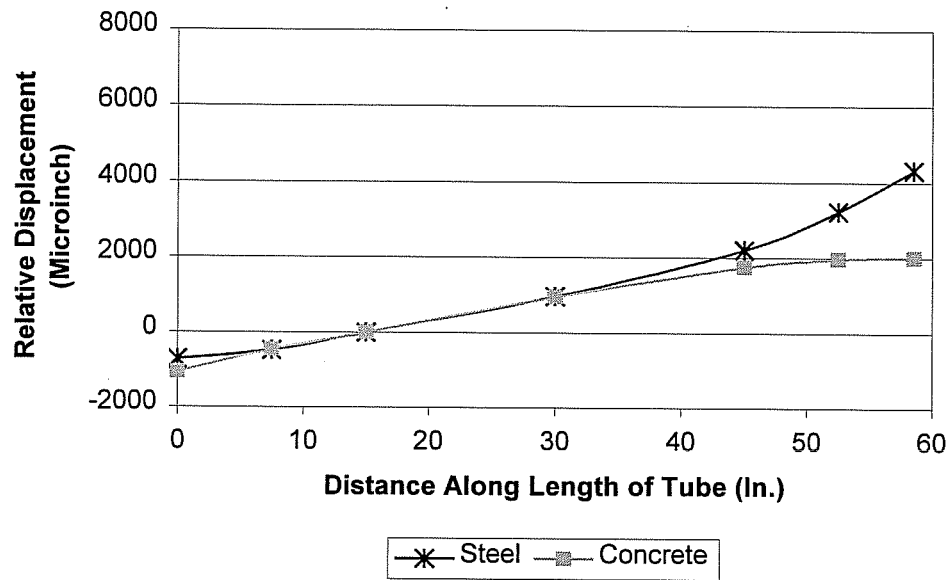


Figure 4.49. Elastic shortening of steel and concrete in CFT8 at $P = 0.76 P_{max}$.

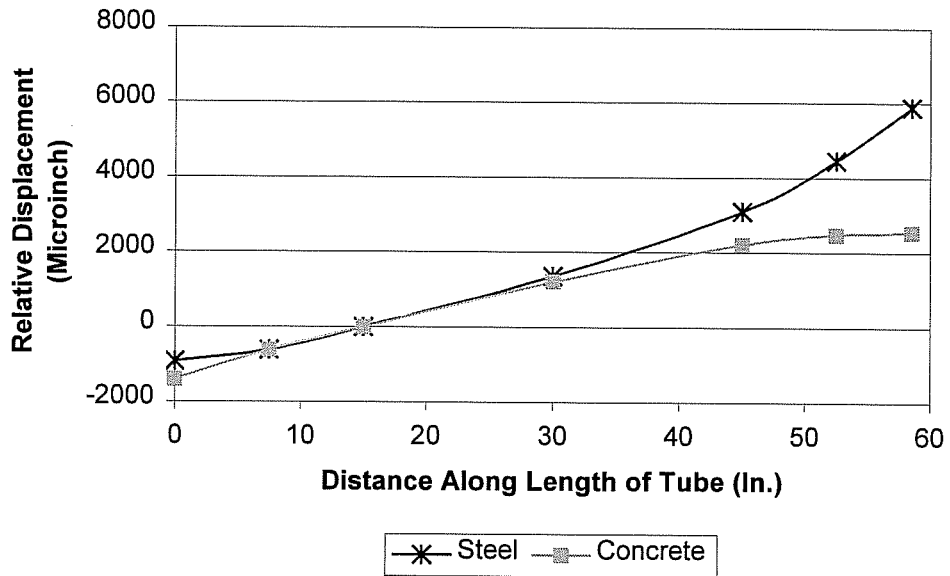


Figure 4.50. Elastic shortening of steel and concrete in CFT8 at $P = 0.99 P_{max}$.

Photographic Evidence of Shear Tab Deformation

In comparison with the 8"x8"x1/4" CFT with shear tabs, the larger specimens underwent smaller deformations at the steel-loaded end during testing. In Figure 4.51, the deformations due to shear tab rotation are clearly visible. In contrast to Figure 4.26 of the 8-in. CFT, the gap between the steel and the concrete at the steel-loaded end is narrower for the 10-in. CFT, indicating that the larger specimen experienced less wedging action than the 8-in. CFT.

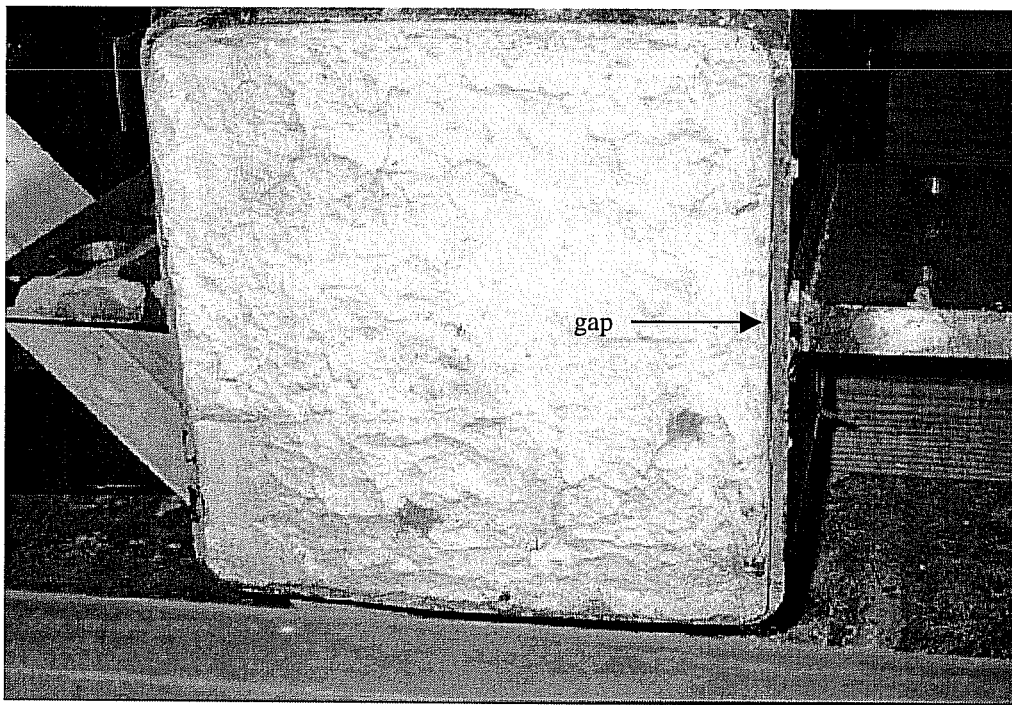


Figure 4.51. 10-in. CFT with shear tabs after testing.

CHAPTER 5

INTERPRETATION OF RESULTS

From the results presented in Chapter 4, similarities and differences in the behavior of the eight specimens are discussed. In addition, the experimental results are compared with those obtained by other researchers.

Throughout this chapter, three mechanisms of load transfer are used to characterize the push-out behavior of the CFT specimens. These mechanisms, which are defined in detail in Chapter 6, are steel-concrete adhesion, friction, and wedging of the concrete core. Adhesion refers to the chemical bond between the concrete paste and the surface of the steel. Friction is the shear stress that develops at the steel-concrete interface as a result of the surface roughness of the steel. Wedging of the concrete core occurs when the slip of the concrete core is resisted by indentations or geometric irregularities in the steel tube.

INTERPRETATION OF 8-IN. CFT'S WITHOUT SHEAR TABS

At small applied loads, the load transfer in CFT4 and CFT3 occurred at the ends of the specimen. As the applied loads approached the peak value, the entire length of interface participated. At loads of $0.80 P_{\max}$ (CFT3) and $0.88 P_{\max}$ (CFT4), the load transfer from the steel to the concrete was evenly distributed along the length of the interface. Uniform load transfer suggests that, at these loads, friction and adhesion contributed more to load transfer than wedging. Wedging on a large scale would have been revealed in variations in the load distribution curve at points of load transfer. However, the behavior of CFT3 at higher applied loads suggests that wedging was to become more important in the transfer of load.

At an applied load of $1.00 P_{\max}$, most of the load transfer in CFT3 had shifted to the 24 inches of interface nearest the concrete-loaded end. The steel tube carried an increased percentage of load relative to the concrete at most of the instrumented planes.

A jagged load distribution curve for the steel suggests that wedging may have been the predominant means of load transfer at this location. The likely explanation for the increase in the load carried by the steel is that the steel tube had become separated from the concrete core along the interface near the steel-loaded end, impeding the transfer of load there. As seen in Chapter 4, when the applied loads increased, differential shortening of the steel and the concrete created slip along the interface near the steel-loaded end. Bond slip along this portion of the interface resulted in a loss of adhesion that could not be regained. Additionally, steel-concrete separation may have occurred as a result of lateral expansion of the steel tube. At small strains, the Poisson's ratio of plain concrete is one half to two thirds as high as that of steel, causing the steel tube to expand laterally and separate from the concrete core (Furlong 1967). At the same time, near the end where the steel was loaded, the steel tube carried greater axial loads than the concrete at the same location. The combination of a greater axial load and a larger Poisson's ratio in the steel led to lateral expansion of the tube away from the concrete. For these reasons, separation of the steel-concrete interface near the steel-loaded end can be surmised.

The relationship of applied load to slip of the infilled concrete for CFT4 and CFT3 also offers evidence of wedging of the concrete core inside the steel tube. Just after the peak load is reached, measurable slip of the concrete core occurs, and adhesion along the steel-concrete interface is lost. That the load on these specimens did not drop off sharply after the peak was reached suggests that, although the adhesive steel-concrete bond was broken, another mechanism of load transfer allowed the CFT to sustain an applied load near the peak value. The gradual decrease in load after the peak can best be explained by wedging action.

If it is accepted that rectangular hollow steel tubes have some deviations from a true prismatic shape from one transverse plane to another, then the occurrence of wedging of the concrete core can be more easily understood. It is likely that while the CFT's were loaded, small localized slips occurred until the concrete core became favorably wedged against the wall of the steel tube, and load increased. As the concrete pushed through the steel tube after the peak, either the localized bulges of the concrete

core were eliminated by crushing of the concrete against the steel or the narrower sections of the steel tube expanded outward to accommodate the bulges in the infilled concrete. This process occurred gradually in CFT4 and CFT3, resulting in a decrease from the peak load to the load supported at the plateau of the load-slip curve. Once the variations in the shape of the steel and the concrete no longer affected the load transfer, a different mechanism developed.

Along the plateau of increasing displacements at a constant load, friction was the likely mechanism of load transfer. At this time, adhesion had been lost, and wedging was no longer effective. The nearly constant load indicates that load transfer was evenly distributed over the length of the interface. As the concrete core moved through the steel tube, the contact surfaces changed, but the capacity of the interface did not. Friction could be considered the source of this uniform load transfer since the surface characteristics of the steel tube were approximately the same over the length of interface. The load distribution curves after the peak load had been applied support a friction mechanism for load transfer along the plateau. After the peak, the load transfer in CFT3 and CFT4 was approximately uniform, except along the portion of CFT3 where separation of the steel tube from the concrete core had occurred.

A study of the initial and reloading stiffnesses determined for CFT4 also provides insight into the predominant load transfer mechanisms. The high initial stiffness offered by the interface (26,000 kips/inch) suggests that all three load transfer mechanisms were present: adhesion, friction, and wedging. At the time of the first reloading, before the peak had been reached, the stiffness was determined to be 18,200 kips/inch. The loss in stiffness upon reloading may be attributed to a permanent loss of adhesion along the approximately 18 inches of interface where bond slips had accumulated. The second reloading of CFT4 took place in the plateau of nearly constant load and increasing displacements. The stiffness of 14,600 kips/inch obtained for this loading indicates both a loss of adhesion as a mechanism of load transfer as well as a loss of wedging action once the plateau in the load-slip curve was reached.

INTERPRETATION OF 8-IN. CFT'S WITH SHEAR TABS

Like the specimens without shear tabs, CFT2 and CFT5 initially transferred the applied load at the ends of the interface. Just prior to the peak load, the load transfer along the interface away from the shear tabs was approximately uniform, while the area near the shear tabs accounted for about 50% of the load transfer. The approximately constant slope on the load distribution curves suggests that friction and adhesion were the primary mechanisms of load transfer away from the shear tabs, but the presence of wedging can not be ruled out since the load distribution curves were not entirely straight.

The relationship of the applied load to slip of the infilled concrete also indicates the effect of wedging in CFT2 and CFT5. Since these specimens were cut from the same length of tubing as CFT3 and CFT4, the cross-sections of CFT2 and CFT5 experienced similar deviations from a true prismatic shape as seen in the previous specimens. These deviations resulted in wedging that occurred along most of the interface. In addition, heat-related deformations from the welding of shear tabs may have contributed to wedging action near the steel-loaded end. Like those of CFT3 and CFT4, the load-slip plots corresponding to CFT2 and CFT5 reveal wedging after the peak was reached. The decrease in load from the peak value suggests that wedging in these specimens was present at the peak and was gradually being overcome.

In contrast to CFT3 and CFT4, wedging for CFT2 and CFT5 also occurred during the period of large slips of the concrete core. This wedging phenomenon can be explained by rotation of the shear tabs, which caused a pinching of the concrete core at the connection. At an increased load, localized crushing of concrete changed the shape of the wedged portion of the core and allowed it to pass through the narrower area. In a step fashion, other sections of the concrete core became wedged at the same location, repeating the cycle. With each recorded slip of the concrete core, the load supported by the CFT increased. Thus, the pinching near the shear tabs became more effective as the applied loads on the tabs increased. Indeed, the effectiveness of the shear tab connection as a load transfer mechanism can be seen in the load distribution plots, which indicate that 12 inches of interface nearest the shear tabs were responsible for about 50% of the load transfer throughout the loading.

INTERPRETATION OF 10-IN. CFT'S WITHOUT SHEAR TABS

Like the load transfer in previous specimens, load transfer in CFT7 and CFT1 began at the ends of the interface. Unlike previous specimens, however, CFT7 and CFT1 never developed uniform load transfer prior to the peak load. In fact, just before the peak, most of the load transfer took place in the quarter length of interface nearest the concrete-loaded end. These 10-in. CFT's likely experienced separation of the steel tube from the concrete core over a larger interface area than the 8-in. CFT's without shear tabs. The plots of elastic shortening of the steel and the concrete immediately before peak confirm that CFT7 and CFT1 experienced bond slip over at least 50% of the interface, while the smaller specimens only showed bond slip over one quarter to one third of the interface length.

The larger area of separation along the interfaces of CFT7 and CFT1 relative to those of the 8-in. CFT's may be attributed to differences in wall stiffness. The 10-in. CFT's have a smaller wall stiffness, which may have affected the rate of expansion of the steel tube or the shape it took as it expanded.

Along the 15 inches of interface nearest the concrete-loaded end that continued to transfer load, the primary mechanisms were adhesion and friction. The load-slip plots show no evidence of wedging prior to the peak, because the load dropped off sharply from the peak value. The small increase in load and subsequent decrease after the peak but prior to the plateau suggest an attempt at wedging was made but was unsuccessful in allowing larger loads to be supported. It is likely that the larger steel tubes had fewer deviations from the true cross-section than the 8-in. CFT's because the larger radius at the corners required less bending of the steel sheets during fabrication and because the flat surfaces of the 10-in. CFT's were wider and more prominent. Along the plateau of constant load and large displacements, the load transfer was evenly distributed along the entire length of interface, except where steel-concrete separation was irreversible, further supporting friction as the primary means of post-peak load transfer.

INTERPRETATION OF 10-IN. CFT'S WITH SHEAR TABS

The behavior of the 10-in. CFT's with shear tabs up to the peak load was similar to that of the 8-in. shear-tab specimens. Load transfer occurred initially at the ends of the interface. Generally, the lengths of interface near the shear tabs accounted for 50% of the load transfer for CFT8 and CFT6. At applied loads from $0.76 P_{max}$ to $0.93 P_{max}$, load transfer was evenly distributed along the remainder of the interface, suggesting that adhesion and friction were the primary contributors to load transfer away from the shear tabs.

Near the peak, the behaviors of CFT8 and CFT6 lost some of their similarities. CFT6 showed nearly uniform load transfer immediately before the peak over a length of interface from zero to 45 inches relative to the concrete-loaded end. In contrast, CFT8 provided evidence that the steel tube was taking on increased percentages of load at an applied load of $0.99 P_{max}$. Separation along the interface likely accounted for the inefficiency of load transfer at the steel-loaded end. In fact, the load distribution plot for CFT8 after the peak indicates that no load transfer was taking place along the 15 inches of interface nearest the shear tabs.

Although the post-peak behaviors of CFT8 and CFT6 were different, the mechanisms for the load transfer were the same. The bond contribution offered by adhesion had been lost, but friction still was effective. Wedging provided another likely mechanism for load transfer. Wedging action from the rotation of the shear tabs is evident on the plots relating load to slip of the infilled concrete. The load on the specimens dropped off after the peak, and then increased to a plateau value at which large displacements continued to occur. This incidence of load increase can be attributed to pinching of the concrete core associated with rotation of the shear tabs.

The location of the wedging action in CFT8 varied from the location seen in CFT6. After the peak, most of the load transfer in CFT8 occurred along the length of interface located from 30 to 45 inches relative to the concrete-loaded end. For specimen CFT6, the post-peak load transfer was located along 15 inches of interface nearest the steel-loaded end. Load transfer in both specimens can likely be attributed to both friction and wedging. Although the location of load transfer varied from specimen to specimen,

both specimens were able to support loads of similar magnitude, suggesting that the shear tab connection is effective in accomplishing load transfer from the steel to the concrete.

COMPARISON OF BOND STRENGTHS

The following definitions of bond strength have been adapted from Rabbat and Russell (1985). Peak bond strength is the peak applied load divided by the area of interface. An effective bond strength describes the shear stress at the plateau where large displacements occur under a nearly constant load. It is equal to the load at the plateau divided by the area of interface. The effective bond strengths for CFT2 and CFT5 must be calculated as ranges of values since there was no a distinct plateau of constant applied load for either specimen. Table 5.1 is a summary of bond strengths for the test specimens.

Table 5.1. Peak and effective bond strengths for test specimens.

Specimen	Width of Tube (In.)	Shear Tabs?	Peak Load (Kips)	Peak Bond Stress (Psi)	Effective Load During Slip (Kips)	Effective Bond Stress (Psi)
CFT4	8	n	61	43	32	23
CFT3	8	n	56	40	35	25
Average of CFT4 and CFT3	8	n	59	42	34	24
CFT2	8	y	98	70	67-73	47-52
CFT5	8	y	101	72	60-71	43-51
Average of CFT2 and CFT5	8	y	100	71	63-72	45-51
CFT7	10	n	61	27	41	19
CFT1	10	n	57	26	41	19
Average of CFT7 and CFT1	10	n	59	27	41	19
CFT8	10	y	67	29	60	26
CFT6	10	y	70	31	63	28
Average of CFT8 and CFT6	10	y	69	30	61	27

Four significant observations may be made regarding the experimentally obtained bond strengths:

1. The ratio of the average peak bond strength of the 8-in. CFT's *with* shear tabs to that of the 8-in. CFT's *without* shear tabs is 1.70. The ratio of the average peak bond strength of the 10-in. CFT's *with* shear tabs to that of the 10-in. CFT's *without* shear tabs is 1.14.

Shear tabs in the 8-in. CFT's significantly increased the peak bond strength. The increase in strength may be attributed to deformation of the steel tubes at the shear tabs as a result of both the welding process and the rotation of the connections during loading.

The larger CFT's did not experience as much heat-related deformation during welding and cooling of the shear tabs. In addition, rotation of the shear tab connection in a larger tube does not alter the shape of the cross-section as much as deformation in a smaller section would, so the pinching effect from the shear tabs is reduced. Therefore, the 10-in. CFT's did not show a significant increase in bond strength over those without the shear tabs.

2. The ratio of the average peak bond strength of the 10-in. CFT's *without* shear tabs to that of the 8-in. CFT's *without* shear tabs is 0.63. The ratio of the average peak bond strength of the 10-in. CFT's *with* shear tabs to that of the 8-in. CFT's *with* shear tabs is 0.43.

The peak bond strength is affected by the tube dimensions. In all cases, the 10-in. CFT's showed a decrease in peak bond strength relative to the corresponding 8-in. CFT's. The smaller wall stiffness of the 10-in. CFT's may have allowed for increased lateral expansion of the steel tubes relative to the concrete core.

3. The ratio of the average effective bond strength of the 8-in. CFT's *with* shear tabs to that of the 8-in. CFT's *without* shear tabs is 1.89-2.15. The ratio of the average effective bond strength of the 10-in. CFT's *with* shear tabs to that of the 10-in. CFT's *without* shear tabs is 1.44.

For the 8-in. CFT's, the presence of shear tabs resulted in a two-fold increase in effective bond strength. The 10-in. CFT's showed a smaller (44%) increase in effective bond strength in the specimens with shear tabs. The increased bond strengths may be attributed to the rotation of the shear tab connections. To compare this behavior to that associated with the first observation above, the presence of shear tabs in the 10-in. CFT's is shown to increase only the effective bond strength, but not the peak bond strength. This behavior supports the theory that wedging action in the 10-in. CFT's only occurred after the peak load had been reached.

4. The ratio of the average effective bond strength of the 10-in. CFT's *without* shear tabs to that of the 8-in. CFT's *without* shear tabs is 0.78. The ratio of the average effective bond strength of the 10-in. CFT's *with* shear tabs to that of the 8-in. CFT's *with* shear tabs is 0.53-0.60.

For all specimens, the larger CFT's showed lower values of effective bond strength than the 8-in. CFT's. However, the decrease in effective bond strength as a result of size of the steel tube is not as pronounced as that decrease seen in the peak bond strengths (the second observation, above). It is likely that the loss of adhesion due to separation along portions of the steel-concrete interface, which contributed to the decreased peak bond strengths of the 10-in. CFT's, was no longer a factor after the peak load of a specimen was reached.

COMPARISON OF INITIAL AND RELOADING STIFFNESSES

The initial stiffness of each specimen was difficult to define because the plot of applied load versus slip of the infilled concrete was never a straight line from zero load to the peak. Most specimens showed a stiffening effect as the infilled concrete experienced early initial slip, but with wedging, loads increased. Consequently, initial stiffness of each specimen was estimated as the best-fit line through the set of points including the peak that most resembled a straight line, i.e., the best-fit line that could be obtained once the specimen exhibited a relatively constant stiffness. Because of the errors inherent in calculating initial stiffness, the values obtained should be considered approximate, and comparison of relative stiffnesses is more accurate than any one calculated stiffness.

On the other hand, the stiffnesses determined during reloading of the specimens appear more accurate. Since the concrete core had already become wedged inside the tube, local slips were not evident. All of the data points used to calculate reloading stiffnesses fell on a straight line, and a best-fit line to represent the stiffness could be determined with confidence.

Table 5.2 shows the initial and reloading stiffnesses for all specimens. Due to inaccuracies in determining initial stiffnesses, only two observations can be made with

confidence. First, the 10-in. CFT's without shear tabs showed a loss in stiffness of about 23% upon reloading. The likely explanation for this decrease is the loss of adhesion after the peak and the irreversible separation of the steel tube from the concrete core that had occurred along portions of the interface. On the other hand, the 8-in. CFT's with shear tabs indicated a 93% increase in stiffness upon reloading. At the time these specimens were reloaded, the connections had experienced large rotations. Upon reloading, wedging action offered significant shear transfer that had not been available during the initial loading.

Table 5.2. Initial and reloading stiffnesses for test specimens.

Specimen	Width of Tube (In.)	Shear Tabs?	Initial Stiffness (Kips/In.)	Reloading Stiffness after Peak (Kips/In.)	RS / IS (%)
CFT4	8	n	26000	14600	56
CFT3	8	n	11100	14500	131
Average of CFT4 and CFT3	8	n	18600	14600	94
CFT2	8	y	5650	12500	220
CFT5	8	y	10000	16600	165
Average of CFT2 and CFT5	8	y	7800	14600	193
CFT7	10	n	13100	11100	85
CFT1	10	n	37000	22500	61
Average of CFT7 and CFT1	10	n	25100	16800	73
CFT8	10	y	19800	17000	86
CFT6	10	y	12900	27900	220
Average of CFT8 and CFT6	10	y	16400	22500	153

RELATION TO OTHERS' RESEARCH RESULTS

Load – Slip Behavior

To test the CFT behavioral observations developed in this chapter, the results of the experimental investigation are related to the results of previous researchers. In 1985, Rabbat and Russell published the results of an investigation of push-off tests of concrete blocks on steel plates. The plots of shear stress versus slip that were presented resemble the shape of the load-slip plots obtained for specimens CFT3 and CFT4. A high initial stiffness was observed, a peak bond stress was reached, and large displacements continued at a constant load. There was no sudden drop in load evident at the peak; any decreases in load after the peak were gradual. Unlike the results obtained for CFT4 and CFT3, the push-off tests do not always show a decrease in load from the peak to the plateau. Because the surfaces of steel plates are more truly flat than the surfaces of steel tubes, wedging or friction on a large scale is not possible during the push-off tests and the steel-concrete contact area is constant. Thus, the large decrease in load after the peak load in the load-slip response of CFT4 and CFT3, which has been attributed to wedging of the concrete core, is not apparent in the results of the push-off tests.

Shakir-Khalil (1993a) presents the results of push-out tests of rectangular CFT's. The curves of load versus slip for 150 x 150 x 5-mm CFT's (5.9 x 5.9 x 0.20-in. CFT's) look similar to those in the plots corresponding to CFT4 and CFT3. The load-slip plots of Shakir-Khalil show the typical high initial stiffness, followed by a plateau of large displacements at a nearly constant load. The results corresponding to Shakir-Khalil's shortest specimens, with a length to width ratio (l/b) between 1.7 and 3, do not show any decrease in load after the peak. Therefore, it can be assumed that these specimens did not experience any significant wedging action during testing. Shakir-Khalil's longer CFT's ($l/b = 4$), do indicate a drop in load after the peak, but not as large as the decrease seen in CFT4 or CFT3. Thus, with a length to width ratio of 6, CFT4 and CFT3 experienced more wedging than did the specimens of Shakir-Khalil with a length to width ratio of 4. Intuitively, longer specimens should have more deviations from the true cross-section along the length, and therefore wedging should be more prevalent in these specimens.

The results of push-out tests of rectangular CFT's with various surface characteristics presented in Shakir-Khalil (1993b) also support this theory about wedging in CFT's. With a length to width ratio of 2.7, a specimen without mechanical shear connectors likely would not have experienced significant wedging of the concrete core. In fact, the load-slip plot of this specimen indicates that no decrease in load occurred after the peak.

Virdi and Dowling (1980) conducted push-out tests on round CFT's. A typical load-slip plot included in their results showed an initially stiff region, followed by a reduction in stiffness associated with a relatively flat response. In contrast to the very flat plateaus of CFT4 and CFT3, the load-slip plots of Virdi and Dowling's round specimens showed a gradual increase in load during the period of increasing displacements.

Bond Strengths

Mains (1951) presents the experimental bond strengths obtained in pull-out tests of plain reinforcing bars embedded in concrete. The bond strengths Main reported ranged from 180 to 300 psi, much higher than even the 72 psi reached by CFT5. In contrast to the CFT's, the bars tested by Mains likely gained bond strength as a result of shrinkage of the concrete. Adhesion of the concrete to the bars was a greater contributor to bond strength in Mains' tests than in rectangular CFT's.

The push-off tests of Rabbat and Russell (1985) indicated peak bond strengths from 53 to 67 psi. These values fall within the range of values obtained for the rectangular CFT's and given in Table 5.1, and are reasonable for a steel-concrete interface.

Similarly, the peak bond strengths reported by Shakir-Khalil (1993a, 1993b) are consistent with the results presented in Table 5.1. Shakir-Khalil presents average values ranging from 29 to 85 psi for the peak bond strengths of 150 x 150 x 5-mm CFT's in push-out tests. The wide range in the bond strengths reported in this publication can be attributed to the varying interface lengths from 200 to 600 mm, which correspond to length-to-width ratios from 1.7 to 4.0.

CHAPTER 6

A MODEL FOR THE SHEAR TRANSFER MECHANISM

The results presented in previous chapters have shown that three mechanisms are responsible for the shear transfer along the steel-concrete interface in a CFT: adhesion of the concrete to the steel, friction, and wedging of the concrete core. In this chapter, a model for the shear transfer mechanism is developed based on these results.

ADHESION

Definitions Accepted by Previous Researchers

Adhesion is a chemical bond that occurs between the concrete paste and the surface of the steel. It is capable of transferring both shear and tensile stresses across the interface (Lamport 1988). Equal strains in the concrete and the steel at a point on the interface characterize an intact adhesive bond (Lamport 1988). In a discussion of the adhesive bond of concrete to steel reinforcing bars, ACI Committee 408 (1966) reported that the bond is easily broken by slip that occurs adjacent to a crack in reinforced concrete. It can be inferred that slips of the concrete core in a CFT can similarly lead to loss of adhesive bond. Once bond stresses exceed the capacity of adhesive bond, this load transfer mechanism is lost and can not be regained (Lamport 1988). In his study of grouted connections, Lamport proposed that the contribution of adhesion to load transfer be neglected for two reasons. First, the adhesive bond strength is small in comparison with the capacities of other shear transfer mechanisms. Second, loss of an adhesive bond is irreversible. Once broken, it can no longer contribute to the bond strength.

Application to Current Research Results

As mentioned in the previous chapter, adhesion is thought to contribute to the shear transfer related to the initially stiff portion of the load-slip plots. The 30% loss of stiffness associated with the first reloading of CFT4 relative to the initial value indicates

that a loss of adhesion occurred locally prior to the peak load. Evidence of the loss of adhesive steel-concrete bond can be seen where local slip near the ends of the specimens forced the load transfer toward central portions of the interface.

In general, adhesion was not seen as a primary contributor to load transfer, but rather as an aid to the other mechanisms. Even after the contributions of adhesion were partially or completely exhausted, the specimens continued to transfer shear through other mechanisms.

FRICITION

Definitions Accepted by Previous Researchers

Different researchers refer to the friction mechanism by various names. Lamport (1988) used “Coulomb friction” to describe the shear stress that develops at the interface and is equal to the normal compressive stress multiplied by a characteristic coefficient of friction. Viridi and Dowling (1980) and Shakir-Khalil (1993a) called the friction mechanism “microlocking.” Viridi and Dowling (1980) defined this mechanism as “the interlocking of concrete in the surface roughness of steel.” They suggested that the bond offered by friction is broken when the concrete interface reaches a local strain of 0.0035, the crushing strain of concrete in compression.

Application to Current Research Results

As explained in Chapter 5, the contribution of friction is indicated by uniform load transfer along the length of interface. Since friction is the only mechanism of load transfer directly related to the surface conditions of the interface, and the characteristics of an interface are assumed to be constant over its length, a rate of load transfer which is constant along the length of interface suggests friction as the primary mechanism. Many of the specimens provided evidence of the contribution of friction prior to the peak. CFT4 and CFT3, for example, displayed uniform load transfer at applied loads of $0.88 P_{\max}$ and $0.80 P_{\max}$, respectively. All four specimens with shear tabs indicated that load transfer was evenly distributed along portions of the interface away from the connections just before the peak loads. After the peak loads, the four specimens without shear tabs

showed uniformity in load transfer along the entire length of interface, except where irreversible separation of the steel tube from the concrete core had occurred. In general, the experimental results showed that the specimens relied on friction just before the peak applied load and after the peak when the contributions of wedging of the concrete core had deteriorated.

WEDGING OF THE CONCRETE CORE

Definitions Accepted by Previous Researchers

Virdi and Dowling (1980) described wedging of the concrete core inside the steel tube as “macrolocking.” They defined this mechanism as the “type of bond resistance [that] occurs due to the manufacturing tolerances associated with the internal diameter of the tube.” Shakir-Khalil (1993a) also refers to this mechanism as macrolocking and defines it as “the frictional resistance to movement along the steel-concrete interface [that] is dependent on the deviation of the internal section dimensions from the true surface shape.”

Application to Current Research Results

All of the specimens showed evidence of wedging of the concrete core at some point during their tests. For CFT4 and CFT3, the 8-in. CFT’s without shear tabs, wedging occurred along a length of interface near the concrete-loaded end just prior to and immediately after the peak, until the wedging mechanism was expended. For specimens CFT7 and CFT1, which were also without shear tabs, the interfaces supported a small increase in load which was attributed to wedging after the peak, but the specimens could not sustain the increased loads. Thus, in all CFT’s without shear tabs, the contributions of wedging to load transfer were eventually lost, as either the protruding portions of the concrete core were reduced or the indentations in the steel tube were pushed outward.

In contrast, once wedging in a CFT with shear tabs had been initiated by large rotations of the shear tab connections, the capacity for load transfer by this mechanism was not exhausted during the remainder of the test. Rotation of the shear tab connection

provided a location for wedging to occur in the pinched regions of the steel tube. For CFT2 and CFT5, the effects of wedging action were observed both before and after the peak loads. The shear tabs consistently provided at least 50% of the shear transfer in these CFT's. For CFT8 and CFT6, wedging was noticeable after the peak applied loads, as the length of interface just above the shear tabs accounted for most of the load transfer at that time. Suppose that the push-out specimens had been constructed with the shear tabs welded at mid-height of the steel tube instead of near an end. It is likely that the rotations of these stiffer shear tab connections would be smaller, and, consequently, the contributions offered by wedging would be less than those observed in the current series of tests. In the test specimens with the shear tabs, the contributions of wedging due to rotation of the connection were as important as friction.

MODEL FOR SHEAR TRANSFER IN CFT'S

Shear Transfer in CFT Push-Out Tests

A model for the transfer of shear in a CFT during a push-out test has been developed incorporating the three mechanisms of adhesion, friction, and wedging of the concrete core. When a specimen is first loaded, adhesion and friction provide for the initial load transfer. Small, localized movements of the concrete core within the steel tube help the core to become wedged, and loads increase. At low applied loads, the transfer of load occurs primarily at the ends of the interface. As the applied loads increase, the entire length of interface is mobilized to resist the shear forces. In CFT's without shear tabs, friction provides uniform load transfer along the interface just prior to the peak applied load. The CFT's with shear tabs also develop the maximum frictional capacity of the portions of interface located away from the shear tabs. Thus, all CFT specimens rely on the maximum contributions of friction near the peak applied load.

Wedging contributes to load transfer near the peak applied load in certain situations. In steel tubes, especially those with smaller widths, the fabrication of the tube results in deviations of the tube walls from plane surfaces. Indentations in the steel tube allow the concrete core to become wedged at these locations. Increased load transfer from the steel to the concrete can result from this wedging. In addition, shear tab

connections that are large relative to the width of the tube rotate and cause pinching of the concrete core. Wedging where the width of the tube has been reduced by pinching leads to an increase in the interface capacity of these specimens.

After the peak load is reached, the stiffness provided by the interface decreases sharply. Large displacements of the concrete core commence, and the adhesive steel-concrete bond is broken by these displacements. Friction, however, remains effective as a load transfer mechanism, and supports a load whose magnitude is typically somewhat less than the peak value. The wedging that resulted from manufacturing tolerances is exhausted as either the protruding concrete is reduced or the indentations in the steel tube expand outward to allow the concrete core to pass through. On the other hand, wedging that results from rotation of the shear tab connection continues to offer a local means of load transfer after the peak.

Effect of Shear Tabs on Shear Transfer

The experimental results offer some insight into the effect of shear tabs on load transfer in CFT's. In general, these connections transferred load through pinching of the concrete core as they rotated. For many specimens, this rotation increased the maximum load that an interface was able to support. For other specimens, those in which the width of the tube was large relative to the connection size, significant wedging action did not begin until large rotations had been developed, typically after the peak load had been reached. In other words, the presence of shear tabs in larger CFT's does not have an effect on the peak load that the interface can support.

Effect of Wall Stiffness on Shear Transfer

The effect of wall stiffness on load transfer can be inferred from the differences in shear capacity between the 8-in. and the 10-in. CFT's. Generally, in CFT's with less stiff steel tubes, the steel tube separates more easily from the infilled concrete as the steel is loaded. This separation of the interface can be attributed to the Poisson effect, and is not reversible. For this reason, the CFT's that are less stiff can support a smaller maximum interface stress than their stiffer counterparts. A reduction in the maximum

interface stress is expected when the width of the concrete core increases or when the tube wall stiffness decreases.

APPLICATION OF THE MODEL TO CFT COLUMN DESIGN

The basic question regarding shear transfer in a CFT column is whether or not the bond strength of the steel-concrete interface can adequately transfer the necessary proportion of the vertical reaction from the beams to the concrete core of the composite column. An effective solution to the design problem depends on an accurate, yet conservative, estimate of the maximum bond stresses that can be developed along the steel-concrete interface to accommodate this shear transfer.

Effect of Shear Tabs on Bond Strength

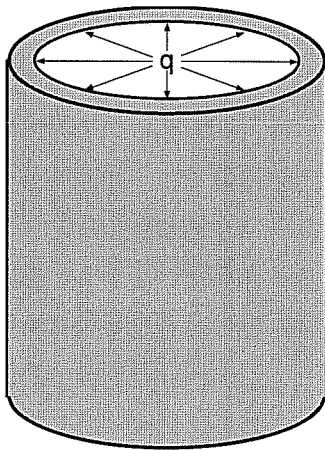
A conservative approach for accounting for the effect of shear tabs on bond strength is to neglect the connections altogether. Unless the connection is large relative to the width of the tube, wedging of the concrete core as the connection rotates can not be counted on prior to the development of the maximum shear stress on the interface. Since too few CFT push-out tests have been performed to define precisely a “large” shear tab connection, it is recommended that the designer neglect the effect of the shear tabs on the bond strength.

Effect of Wall Stiffness on Bond Strength

An understanding of the effect of wall stiffness of the steel tube on bond strength can be used to estimate the maximum bond strength for a CFT column. Because the results of this series of experiments have shown that bond strengths increase with larger wall stiffnesses, a relationship between bond strength, the width of the tube (b), and the tube wall thickness (t) can be established. Two formulations of this relationship are proposed in this section.

When an axial load is applied to the concrete core, a pressure perpendicular to the face of the tube occurs at the steel-concrete interface. In circular CFT's, this is referred to as radial pressure. As noted in Chapter 3, this pressure develops a hoop

tension in the steel tube that restrains the concrete core. Another beneficial effect of this pressure is an increase in the bond capacity provided by friction. As long as the steel and concrete surfaces remain intact, the maximum frictional force is proportional to the normal force at the interface due to the pressure. Thus, wall stiffness enhances the steel-concrete bond strength insofar as the steel tube is able to resist deformations perpendicular to its face, which would distort the shape of the tube.



R = internal radius of cylinder

t = thickness of cylinder wall

D = diameter of cylinder

Figure 6.1. Thin-walled pressure vessel model for a round CFT subjected to internal pressure.

Supposing that concrete behaves like a fluid when subjected to a pressure, a cylindrical steel tube may be considered as a thin-walled pressure vessel, with the concrete applying a uniform pressure to the steel tube. When a unit pressure, q , is applied radially to the interior of the pressure vessel (Figure 6.1), a radial deformation, ΔR , is effected. Equation 6-1 gives the relationship between q and ΔR , which can be found in many strength of materials reference books.

$$\Delta R = \frac{q \cdot R^2}{E \cdot t} \quad (6-1)$$

where

ΔR is the change in the internal radius of the steel tube

E is the modulus of elasticity of the steel tube

t is the thickness of the cylinder wall

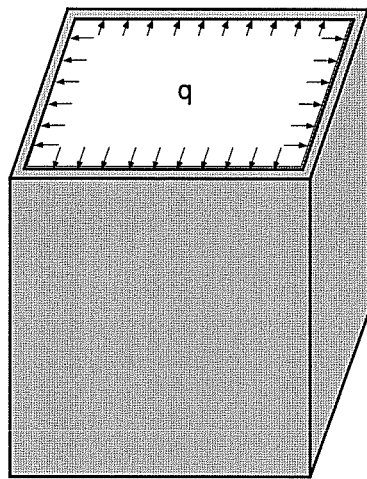
Solving for q gives Equation 6-2, a stiffness equation, in which the radial pressure is shown to be equal to the tube wall stiffness multiplied by the change in radius.

$$q = \left(\frac{E \cdot t}{R^2} \right) \cdot \Delta R \quad (6-2)$$

Using the notation $R = \frac{D}{2}$, where D is the diameter of the cylinder, we have

$$\begin{aligned} q &= \left[\frac{E \cdot t}{\left(\frac{D}{2} \right)^2} \right] \cdot \Delta R \\ &= (4 \cdot E) \cdot \left(\frac{t}{D^2} \right) \cdot \Delta R \end{aligned} \quad (6-3)$$

After the constants, 4 and E , are factored out, it can be seen in Equation 6-3 that the radial stiffness of a thin-walled cylindrical pressure vessel is proportional to (t/D^2) .



b = width of square tube

t = thickness of tube

Figure 6.2. A square CFT subjected to an internal pressure.

A similar analysis may be performed on square CFT's to investigate the influence of tube geometry on wall stiffness. Again, it is assumed that the concrete applies a pressure that is distributed over each face (Figure 6.2). Due to symmetry, it is necessary to investigate the stiffness of only one face of the steel tube. A unit length of the face may be treated as a fixed-end beam with a span length equal to the width of the tube. For a uniformly distributed load, w , the beam model appears as shown in Figure 6.3.

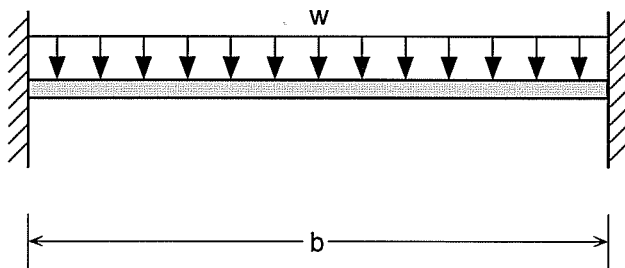


Figure 6.3. Elastic beam model of a length of square CFT subjected to a uniformly distributed pressure.

Equation 6-4 relates the midspan displacement due to the applied loads, Δ , to the material and geometric properties of the beam.

$$\Delta = \frac{w \cdot b^4}{384 \cdot E \cdot I} \quad (6-4)$$

where

b is the span length of the beam model

I is the moment of inertia of the beam model

The moment of inertia of the unit length of steel tube is given by

$$I = \frac{t^3}{12} \quad (6-5)$$

Combining Equations 6-4 and 6-5,

$$\Delta = \frac{w \cdot b^4}{384 \cdot E \cdot \left(\frac{t^3}{12}\right)} \quad (6-6)$$

By rearranging the terms of Equation 6-6, the wall stiffness (w/Δ) at the center of the square face is obtained.

$$\frac{w}{\Delta} = (32 \cdot E) \cdot \left(\frac{t^3}{b^4}\right) \quad (6-7)$$

The wall stiffness is a linear function of the quantity (t^3/b^4) .

Because the stiffness of the tube wall increases near the corners of the square tube, a load distribution such as that shown in Figure 6.4 is a possible representation of conditions inside a CFT.

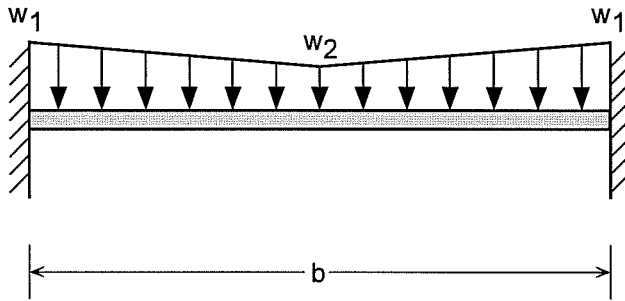


Figure 6.4. Elastic beam model of a length of square CFT subjected to a linearly varying distributed pressure.

For the loading condition shown, any indeterminate structural analysis method may be used to derive the relationship between Δ , w_1 , and w_2 , given in Equation 6-8. In this equation, w_1 and w_2 are magnitudes of the distributed load as shown in Figure 6.4

$$\Delta = \frac{\left(\frac{7 \cdot w_1}{10} + \frac{3 \cdot w_2}{10} \right) \cdot b^4}{384 \cdot E \cdot I} \quad (6-8)$$

Substituting the expression for the moment of inertia given in Equation 6-5, we have

$$\begin{aligned} \Delta &= \frac{\left(\frac{7 \cdot w_1}{10} + \frac{3 \cdot w_2}{10} \right) \cdot b^4}{384 \cdot E \cdot \left(\frac{t^3}{12} \right)} \\ &= \frac{\left(\frac{7 \cdot w_1}{10} + \frac{3 \cdot w_2}{10} \right) \cdot b^4}{32 \cdot E \cdot t^3} \end{aligned} \quad (6-9)$$

Rearranging the expression and factoring out the constants show that the wall stiffness of the square tube can again be linearly related to the quantity (t^3/b^4) .

$$\left(\frac{7 \cdot w_1}{10} + \frac{3 \cdot w_2}{10} \right) \cdot \frac{1}{\Delta} = (32 \cdot E) \cdot \left(\frac{t^3}{b^4} \right) \quad (6-10)$$

Bond strength equations are formulated for rectangular CFT columns that are functions of either of the two proposed stiffness parameters, the parameter indicated by the cylindrical tube model or that indicated by the square tube model. In the cylindrical

tube model, the radial stiffness is proportional to the parameter (t/D^2) . So that the cylindrical model can be applied to the square CFT specimens, D is approximated by b , the tube width. In the square tube model, under either loading distribution, the wall stiffness is proportional to the parameter (t^3/b^4) . Figure 6.5 shows a plot of the experimental peak bond strengths as a function of the stiffness parameter (t/b^2) . In Figure 6.6, a plot of the experimental peak bond strengths as a function of the stiffness parameter (t^3/b^4) is shown.

Data points from push-out tests conducted by Shakir-Khalil (1993a) have also been included in Figures 6.5 and 6.6. Of the rectangular specimens tested by Shakir-Khalil, the peak bond strengths for the 150 x 150 x 5-mm CFT's with a 600-mm interface length have been selected for inclusion in these figures. These specimens had a length-to-width ratio of 4, the largest (l/b) ratio of all of the specimens tested by Shakir-Khalil, while the (l/b) ratio of all specimens in the current test series was still somewhat larger, at 6. In all, results of two specimens tested by Shakir-Khalil and four results from the current series of tests were included in these figures, for a total of six data points.

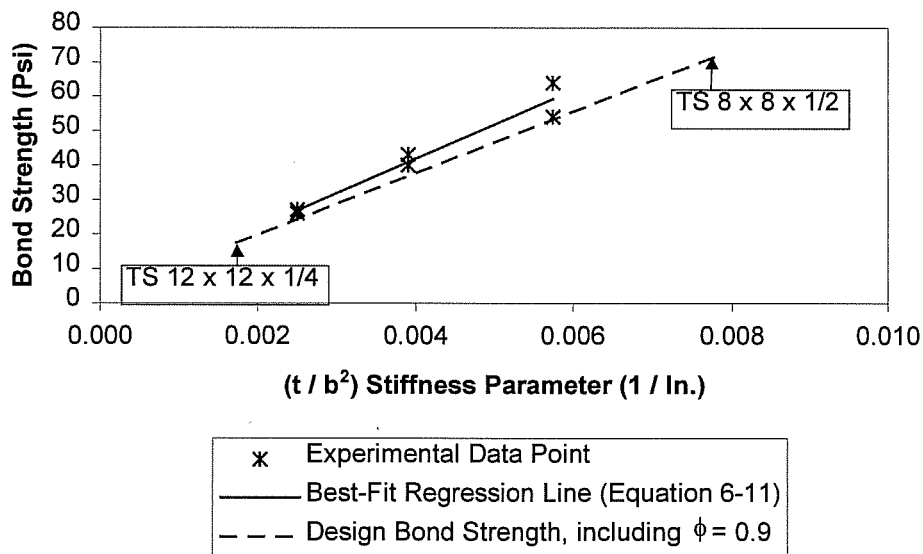


Figure 6.5. Bond strength of rectangular CFT's as a function of the stiffness parameter (t/b^2) . In addition to results from the current series of tests, the results of two specimens tested by Shakir-Khalil (1993a) have been included in this figure.

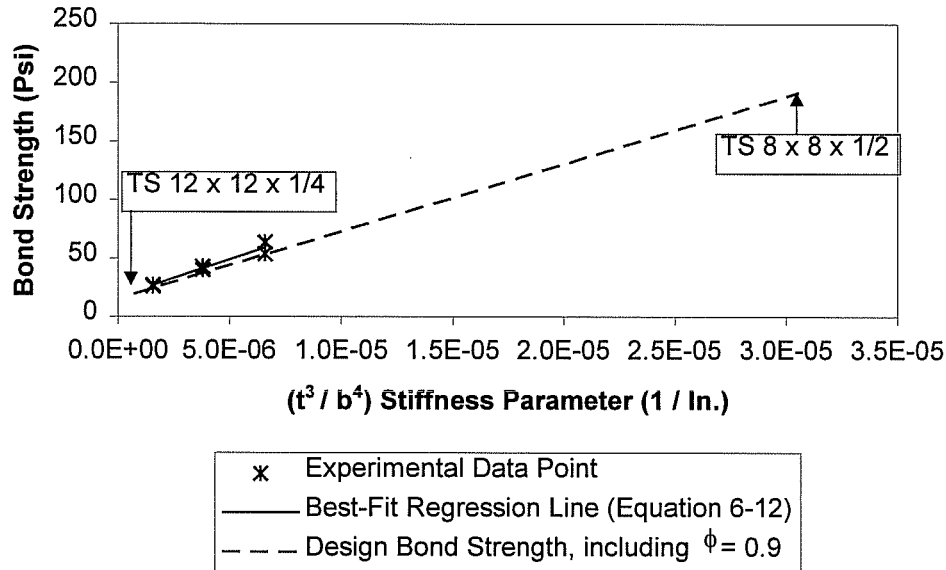


Figure 6.6. Bond strength of rectangular CFT's as a function of the stiffness parameter (t^3/b^4). In addition to results from the current series of tests, the results of two specimens tested by Shakir-Khalil (1993a) have been included in this figure.

From Figures 6.5 and 6.6, a linear relationship between the experimental data and the respective stiffness parameters can be postulated. An equation to predict bond strength is proposed for each model that is determined by the best-fit line drawn through the experimental data. Equation 6-11 gives the bond strength equation that is a function of the parameter (t/b^2), which corresponds to the cylindrical tube model. This equation is shown in Figure 6.5.

$$F_b = 1.9 + 10000 \left(\frac{t}{b^2} \right) \quad (6-11)$$

where

F_b is the bond strength, in psi

t is the tube wall thickness, in inches

b is the tube width, in inches

Alternatively, Equation 6-12, expresses bond strength as a function of the parameter (t^3/b^4) , corresponding to the square tube model. Figure 6.6 shows this equation as the best-fit regression line through the experimental data points.

$$F_b = 16.6 + 6.44 \times 10^6 \left(\frac{t^3}{b^4} \right) \quad (6-12)$$

where

F_b is the bond strength, in psi

t is the tube wall thickness, in inches

b is the tube width, in inches

Both Equations 6-11 and 6-12 predict reasonable and similar bond strengths for the six specimens represented in Figures 6.5 and 6.6.

Design Bond Strength and Associated Strength Reduction Factor

Associated with the maximum bond stress that can be developed along an interface is the reduction factor, ϕ , representing the probability of variations in the bond strength. Neither the LRFD Manual (AISC 1993), nor the ACI Building Code (1995) suggests a ϕ -factor for bond in a CFT. Although the sample size of the current series of push-out tests is too small to indicate a statistically reliable value for the ϕ -factor, some guidance is offered here for selecting a ϕ -factor for bond capacity in CFT columns.

Figures 6.5 and 6.6 also show the design bond strengths obtained when the Equations 6-11 and 6-12, respectively, are multiplied by a ϕ -factor of 0.9. Each of the test specimens indicated a higher experimental bond strength than the proposed design value for a specimen of the same size. Therefore, the design bond strengths suggested are fair estimates of a lower bound to the test data over the range of stiffness parameters represented by the data, when a ϕ -factor of 0.9 is used.

To determine which of the two proposed bond strength equations should be generally applied to the design of CFT columns, design bond strengths were compared over a large range of wall stiffness parameters. Two prototype columns were analyzed using Equations 6-11 and 6-12, multiplied by a ϕ -factor of 0.9. Design bond strengths were calculated for a TS 12 x 12 x 1/4, which has a small wall stiffness, and for a TS 8 x 8

x ¼, with a high wall stiffness. Common sections of steel tubes used in CFT columns have wall stiffness parameters that fall in between these two bounds. The design bond strengths for these example columns are also indicated on Figures 6.5 and 6.6.

As shown in Figure 6.5, the proposed design bond strengths as a function of (t/b^2) for the prototype columns require small extrapolations from the range of stiffness parameters (t/b^2) associated with the experimental results. On the other hand, in Figure 6.6, extremely large extrapolations are necessary to determine the design bond strength of the stiffer 8 x 8 x ¼ section as a function of (t^3/b^4) . It would be unwise and potentially unconservative to use design bond strengths that require such large extrapolations from the experimental data. Therefore, Equation 6-11, as shown in Figure 6.5, is recommended for the design of CFT columns, along with a corresponding ϕ -factor of 0.9.

DESIGN EXAMPLE

A 10 x 10 x ¼-in. CFT column has been selected for use in a multi-story building, based upon LRFD strength requirements for column members (AISC 1993). The vertical load reactions from the beams are applied to the steel tube by simple shear connections at each story. The uniformly distributed dead load on each floor, w_d , is 50 psf, and the uniformly distributed live load, w_l , is 60 psf. The center-to-center spacing of the columns in this structure is 25 ft. In this design example, the CFT section's capacity to transfer factored shear loads from the steel tube to the composite section is analyzed.

For a vertical length of column that spans two adjacent stories, the factored loads applied to the steel tube by the beams at the upper story are assumed to be completely transferred to the concrete core over a length of the steel-concrete interface equal to the story height. This design assumption is conservative because it suggests that the entire shear force due to the upper story must be transferred from the steel tube to the concrete core before additional shear is applied due to the story below. However, in an actual structure, the shear force applied to the steel tube is transferred to the composite section, which implies that some of the load is still resisted by the steel.

The factored floor load, P_u , applied to one column is given by Equation 6-13, where a is the center-to-center spacing of the columns.

$$\begin{aligned} P_u &= (1.2 \cdot w_d + 1.6 \cdot w_l) \cdot (a)^2 & (6-13) \\ &= (1.2 \cdot 50 + 1.6 \cdot 60)(25)^2 \left(\frac{1}{1000} \right) \\ &= 98 \text{ kips} \end{aligned}$$

Equation 6-14 gives an expression for the bond design strength, $\phi_b P_b$, in kips.

$$\phi_b \cdot P_b = \phi_b \cdot A_c \cdot F_b \quad (6-14)$$

where

ϕ_b is the strength reduction factor = 0.9 (selected in a previous section)

A_c is the contact area of the interface, in inches²

F_b is the bond stress predicted by Equation 6-11, converted to ksi

Because the full story height is available to provide shear transfer, the contact area is equal to the story height multiplied by the surface area inside the CFT column.

$$\begin{aligned} A_c &= 13(12)(9.5)(4) & (6-15) \\ &= 5928 \text{ in}^2 \end{aligned}$$

From equation 6-11, F_b , the bond strength of the interface, is

$$\begin{aligned} F_b &= 1.9 + 10000 \left(\frac{t}{b^2} \right) & (6-11) \\ &= 1.9 + 10000 \left(\frac{0.25}{10^2} \right) \\ &= 27 \text{ psi} \end{aligned}$$

Combining Equations 6-14, 6-15, and 6-11, we have

$$\begin{aligned} \phi_b \cdot P_b &= 0.90(5928)(27) \left(\frac{1}{1000} \right) & (6-16) \\ &= 144 > P_u = 98 \text{ kips} \end{aligned}$$

Therefore, the design is satisfactory.

CHAPTER 7

SUMMARY AND CONCLUSIONS

RESEARCH APPROACH

The experimental results of this series of push-out tests were unique when compared to previous research in this area. For example, most previous research involving push-out tests of CFT's was conducted on circular sections, and only short columns were studied. The tests in this study were the first to be performed on rectangular CFT's with a length-to-width ratio greater than 4. In addition, the tests on shear-tab specimens were the first documented push-out tests involving shear tab connections in which all failures occurred along the interface instead of at the connection. The instrumentation scheme of this series of tests was also unique in that concrete embedment gages were used to establish the percentage of applied load resisted by the steel and by the concrete at a transverse plane.

The instrumentation of the specimens and the method for determining the modulus of elasticity of the contained concrete (E_c) contribute to the validity of the experimental results. The construction technique resulted in few voids in the concrete, and the concrete embedment gages were vertically aligned and centered within a cross-section. The strain gages attached to the steel tube were located at the corners of the tube because the increased stiffness there resulted in smaller local bending strains of the tube wall. Therefore, longitudinal strains due to the applied axial load could be more accurately measured. Finally, the method of determining E_c for the contained concrete reduced the errors associated with converting longitudinal strains in the concrete to stresses. When the values of E_c that were determined in the stub column tests were used to calculate the axial load resisted at a cross-section, the average error between the calculated and measured loads was 6%.

BOND STRENGTH

In Table 7.1, the average peak bond strengths of each of four CFT designs are presented.

Table 7.1. Average peak bond strengths for test specimens.

CFT Section	Wall Slenderness Ratio (b/t)	Shear Tabs?	Mean Peak Bond Stress (Psi)
TS 8 x 8 x 1/4	32	n	42
TS 8 x 8 x 1/4	32	y	71
TS 10 x 10 x 1/4	40	n	27
TS 10 x 10 x 1/4	40	y	30

The ratio of the average peak bond strength of the 8-in. CFT's *with* shear tabs to that of the 8-in. CFT's *without* shear tabs was 1.70. The ratio of the average peak bond strength of the 10-in. CFT's *with* shear tabs to that of the 10-in. CFT's *without* shear tabs was 1.14. Thus, it can be inferred that rotation of the tube wall as the shear tab connection was loaded increased the maximum load that the interface could support. For the 10-in. specimens, in which the width of the tube was larger relative to the connection size, wedging at the connections did not have a significant effect on the peak bond strength.

The ratio of the average peak bond strength of the 10-in. CFT's *without* shear tabs to that of the 8-in. CFT's *without* shear tabs was 0.63. The ratio of the average peak bond strength of the 10-in. CFT's *with* shear tabs to that of the 8-in. CFT's *with* shear tabs was 0.43. With a smaller wall stiffness (t/b), the maximum interface stress was less than in the stiffer tube.

LOAD - SLIP BEHAVIOR

In the early stages of loading of a CFT specimen, prior to gross slip of the infilled concrete, the stiffness shown by the load-displacement curve was high. After a peak axial load was reached, large slips were observed at decreased loads. Displacements

increased under nearly constant loads until the concrete core had completely pushed through the steel tube.

An initial stiffness prior to the peak load and a reloading stiffness after large slip of the concrete core were determined for each test specimen. The 10-in. CFT's without shear tabs showed a loss in stiffness of about 23% upon reloading. This loss in stiffness can be attributed to the loss of adhesion after the peak was reached and the irreversible separation of the steel tube from the concrete core that had occurred along portions of the interface.

In contrast, the 8-in. CFT's with shear tabs indicated a 93% increase in stiffness upon reloading. At the time these specimens were reloaded, the connections had already experienced large rotations. Wedging action at the shear tab connections offered a means of shear transfer that had not been available during the initial loading.

DISTRIBUTION OF LONGITUDINAL SHEARING STRESSES

The distribution of longitudinal shearing stresses during testing was used to indicate which portions of the steel tube contributed to the transfer of load from the steel to the concrete for a particular magnitude of applied load. Small applied loads were resisted by the portions of the interface located at the ends of the CFT specimens. As the loads approached peak values, the entire length of the interface away from the shear tabs contributed evenly to the shear transfer. In the 8-in. specimens with shear tabs, the portion of the interface nearest the shear tab connections accounted for about 50% of the load transfer throughout the duration of loading. As the applied loads increased, in several specimens, especially the 10-in. CFT's, the steel tube supported an increased percentage of load relative to the concrete. The increased loads supported by the steel tube can be attributed to separation of the steel from the concrete that had occurred along the interface near the steel-loaded end, which impeded the transfer of load there.

SHEAR TRANSFER MECHANISMS

The experimental results indicated that three mechanisms are responsible for the shear transfer along the steel-concrete interface in a CFT: adhesion of the concrete to the steel, friction, and wedging of the concrete core. Adhesion contributes to shear transfer under initial loading up to the peak. In general, adhesion was not seen as a primary contributor to load transfer, but rather as aid to the other mechanisms. Even after the contributions of adhesion were partially or completely exhausted, the specimens continued to transfer shear through other mechanisms.

Friction as a load transfer mechanism was revealed by uniform load transfer along a length of interface. The experimental results showed that the specimens relied on friction just before the peak applied load and also after the peak when the contributions of wedging of the concrete core had deteriorated.

Wedging of the concrete core resulted in local variations in the load distribution curve. All of the specimens showed evidence of wedging of the concrete core at some point during the tests. In CFT's without shear tabs, the contributions of wedging to load transfer were eventually lost, as the protruding portions of the concrete core were reduced or the indentations in the steel tube were pushed outward. In contrast, once wedging in a CFT with shear tabs had been initiated by large rotations of the shear tab connections, the capacity for load transfer by this mechanism was not exhausted during the remainder of the test. In specimens with shear tabs, the contributions of wedging due to rotation of the connections were as important as friction.

MODEL FOR SHEAR TRANSFER IN CFT PUSH-OUT SPECIMENS

When a specimen is first loaded, adhesion and friction provide the initial load transfer. At low applied loads, the transfer of load primarily occurs at the ends of the interface. As the applied loads increase, the entire interface is mobilized to resist the shear forces. Wedging contributes to the load transfer near the peak applied load in two types of CFT specimens: those of smaller widths and those with shear tab connections that are large relative to the width of the tube.

APPLICATION TO CFT COLUMN DESIGN

The basic question regarding shear transfer in a CFT column is whether or not the bond strength of the steel-concrete interface can adequately transfer the necessary proportion of the vertical reaction from the beams to the concrete core of the composite column. An effective solution to the design problem depends on an accurate, yet conservative, estimate of the maximum bond stresses that can be developed along the steel-concrete interface to accommodate this shear transfer. A conservative approach to accounting for the effect of shear tabs on bond strength is to neglect the connections altogether. To determine the design bond strength for a rectangular CFT column, Equation 6-11 is recommended, in which the design strength is a function of the wall stiffness parameter (t/b^2).

$$F_b = 1.9 + 10000 \left(\frac{t}{b^2} \right) \quad (6-11)$$

where

F_b is the bond strength, in psi

t is the tube wall thickness, in inches

b is the tube width, in inches

A strength reduction factor, ϕ , of 0.9 is recommended for use with the design bond strength as given by Equation 6-11.

RECOMMENDATIONS FOR FUTURE RESEARCH

Before comprehensive provisions for the design of CFT columns including bond strength can be developed, more push-out tests of CFT's should be performed. Testing a wide range of specimen sizes, of both round and rectangular sections, would increase the data base for bond strength and would enable the determination of a statistically reliable strength reduction factor, ϕ , to be used in design. In addition, further tests could be designed to investigate the quantitative relationship between the tube width (b), the tube thickness (t), and bond strength that has been suggested in this study.

A better understanding of wedging action in CFT's is desired so that allowances may be made for its contributions to bond strength in the design of CFT columns. The

current design recommendations in this study are to neglect the contributions of wedging due to the rotation of the shear tab connections and due to the variations in the cross-section geometries along the length of the tube. Testing various sizes of the shear tab connections to the same size of CFT would establish a relationship between connection size and the amount of wedging provided by the rotation of the connection. Also, measurement of the variation in the cross-section geometry along the length of the CFT could establish a relationship between geometrical deviations and the contributions of wedging to bond strength.

APPENDIX

This appendix comprises the figures cited in the section of Chapter 3 entitled “Validation of the Constitutive Relationships Used in the Analysis of Data.” These figures show the axial loads predicted from the strain gage data for each instrumented cross-section of all eight CFT push-out specimens. In each figure, the calculated load in the steel, the calculated load in the concrete, and the combined calculated load in both the steel and concrete are plotted against the applied load for a particular cross-section. A best-fit line, calculated using linear regression techniques, is also shown for the combined calculated load in the steel and concrete. In an ideal test, the calculated combined load would be equal to the applied load. The difference between the slope of the experimental best-fit line and the slope of the line representing ideal conditions, which is given as a percentage on each figure, indicates the amount of error in the strain gage data analysis at a cross-section.

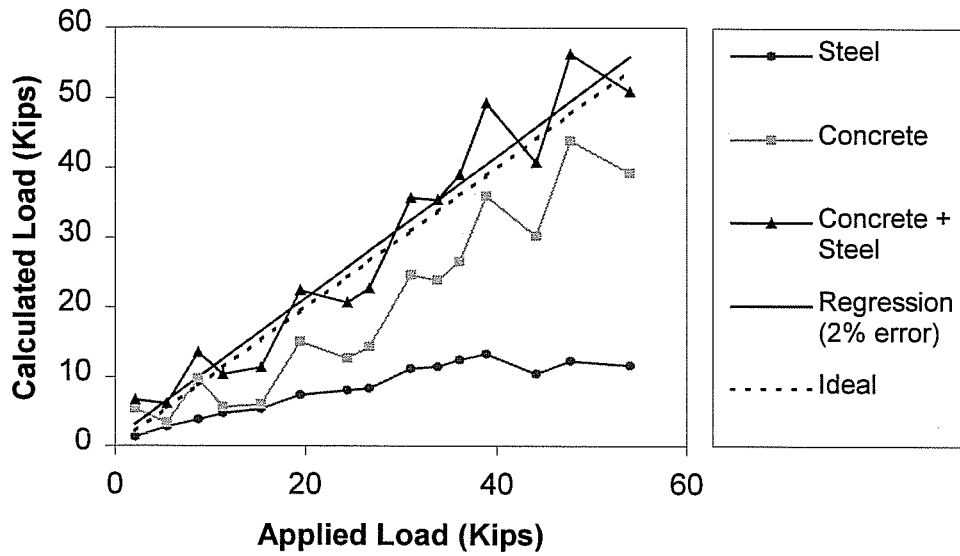


Figure A1. Axial load as calculated in CFT4 from strains at a cross-section located 6 inches from the concrete-loaded end. (This figure is a reprint of Figure 3.5).

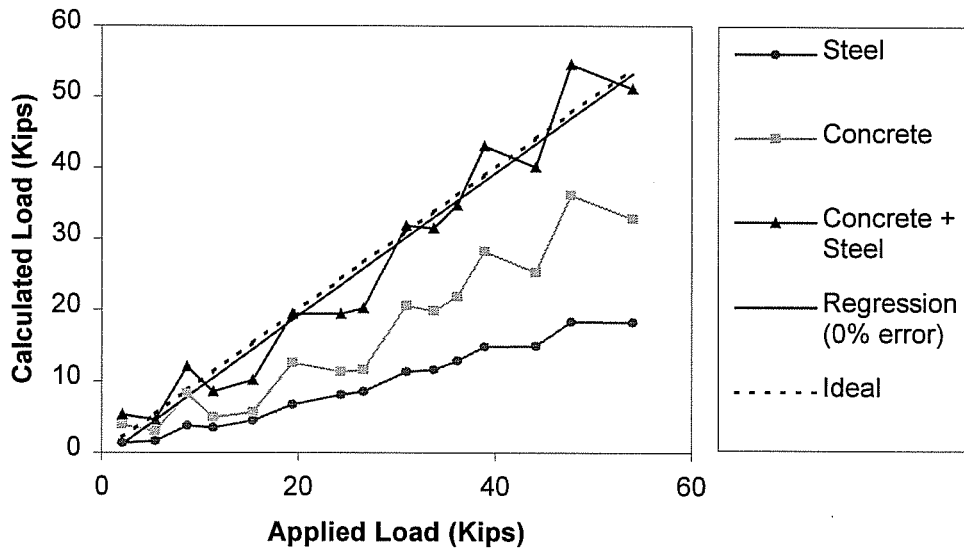


Figure A2. Axial load as calculated in CFT4 from strains at a cross-section located 12 inches from the concrete-loaded end.

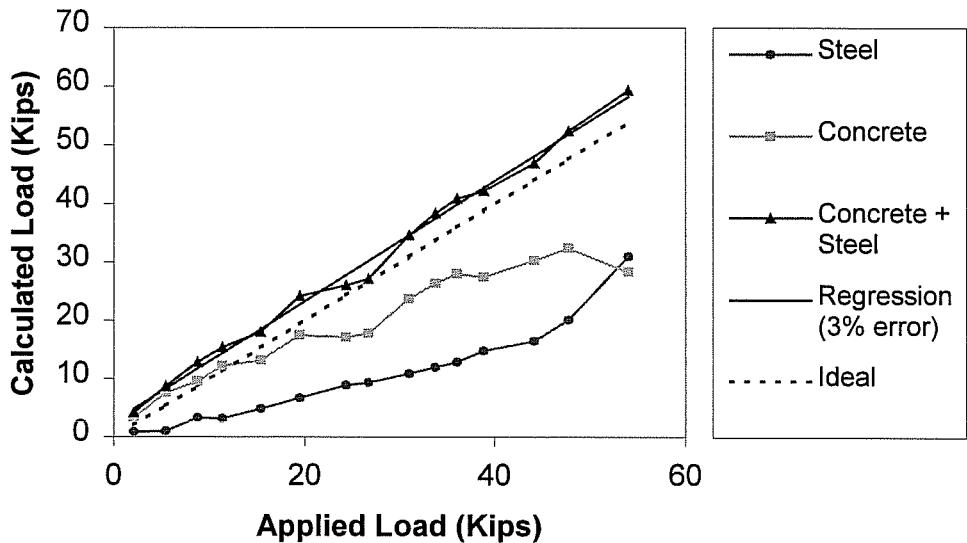


Figure A3. Axial load as calculated in CFT4 from strains at a cross-section located 24 inches from the concrete-loaded end.

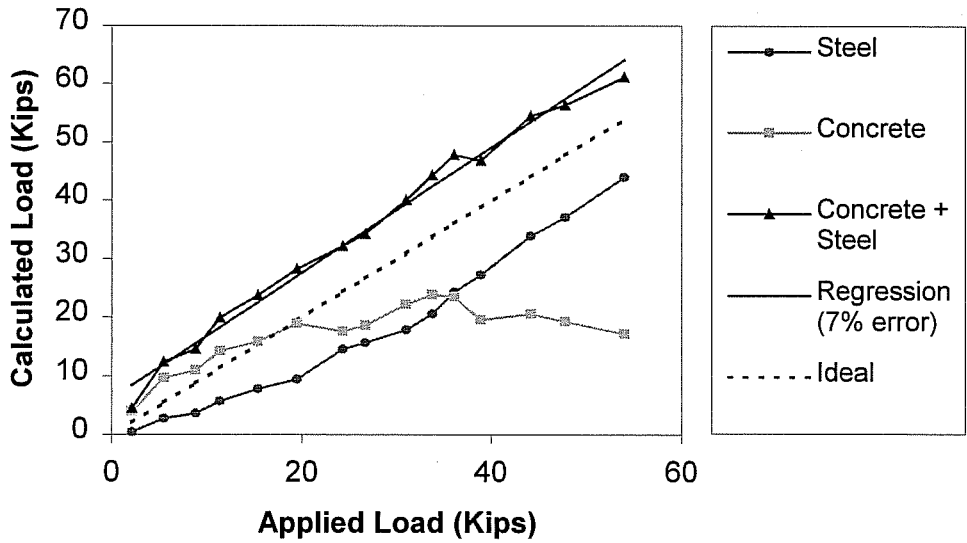


Figure A4. Axial load as calculated in CFT4 from strains at a cross-section located 36 inches from the concrete-loaded end.

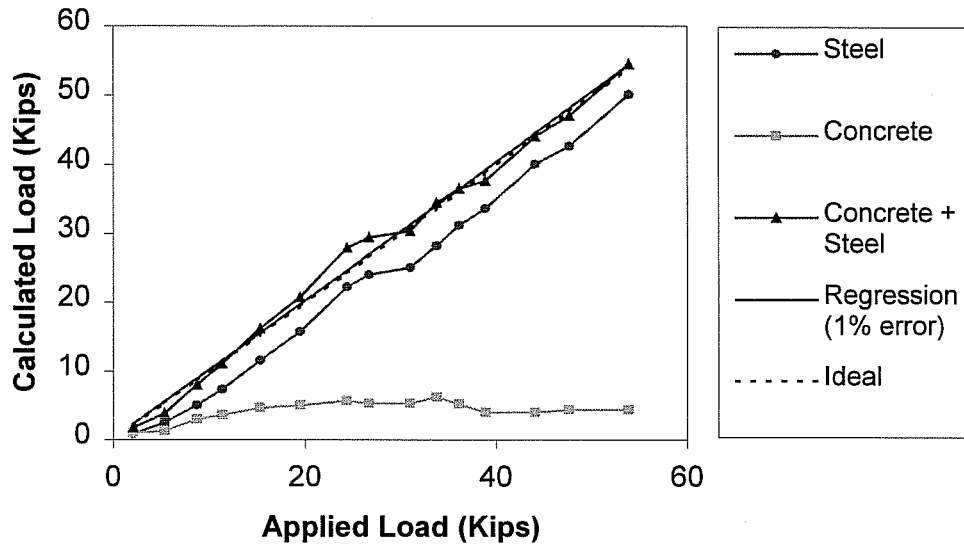


Figure A5. Axial load as calculated in CFT4 from strains at a cross-section located 42 inches from the concrete-loaded end.

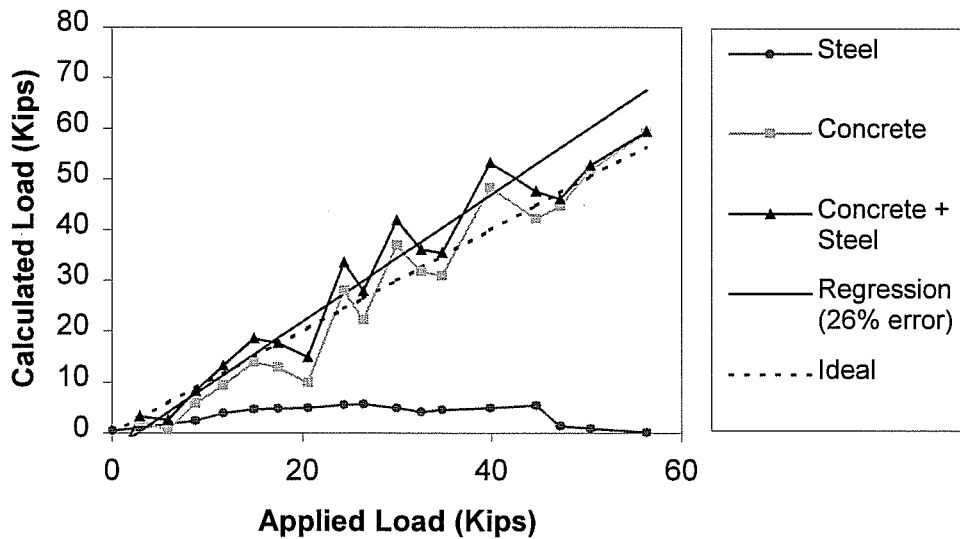


Figure A6. Axial load as calculated in CFT3 from strains at a cross-section located 6 inches from the concrete-loaded end.

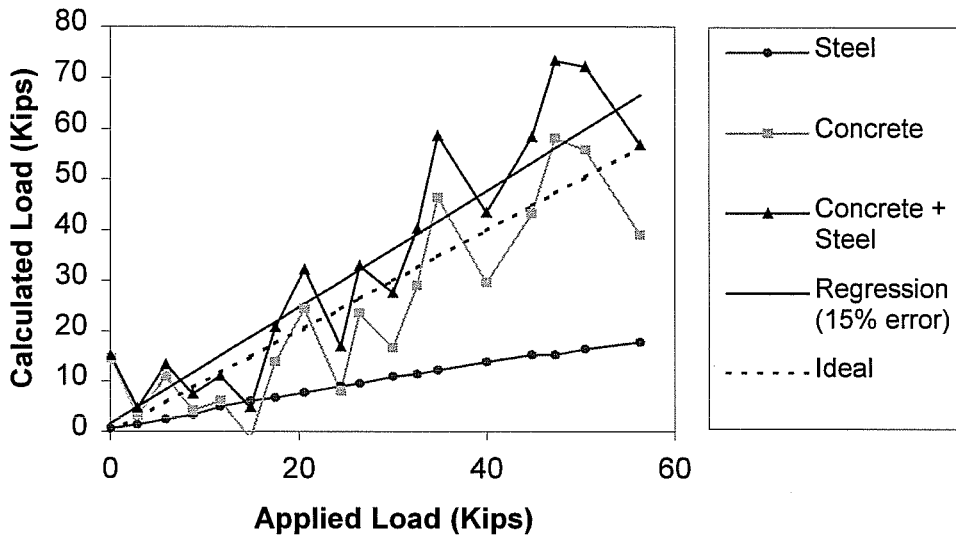


Figure A7. Axial load as calculated in CFT3 from strains at a cross-section located 12 inches from the concrete-loaded end.

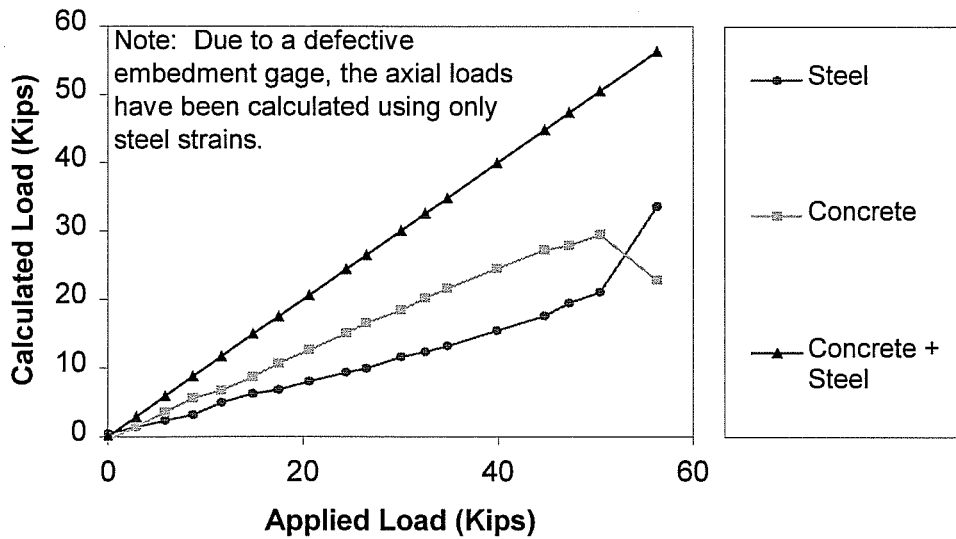


Figure A8. Axial load as calculated in CFT3 from strains at a cross-section located 24 inches from the concrete-loaded end.

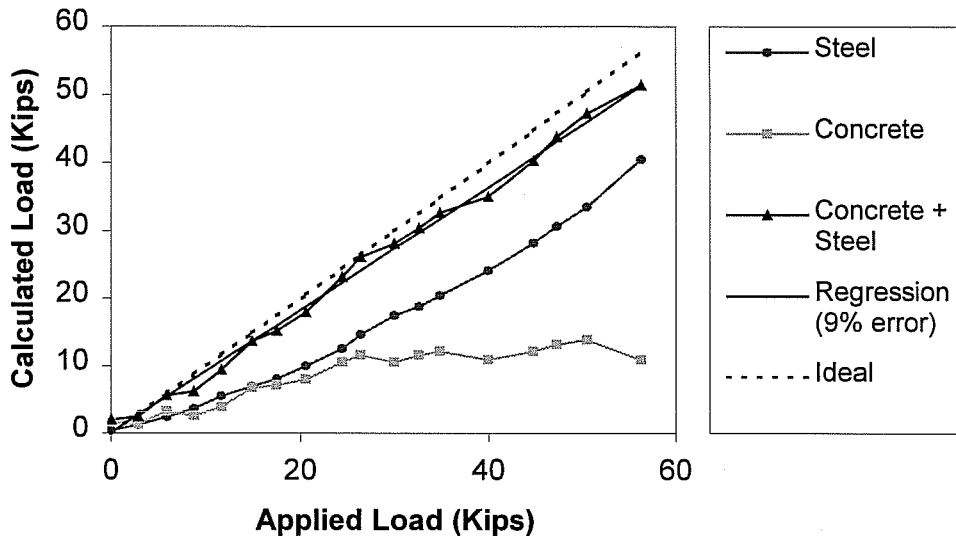


Figure A9. Axial load as calculated in CFT3 from strains at a cross-section located 36 inches from the concrete-loaded end.

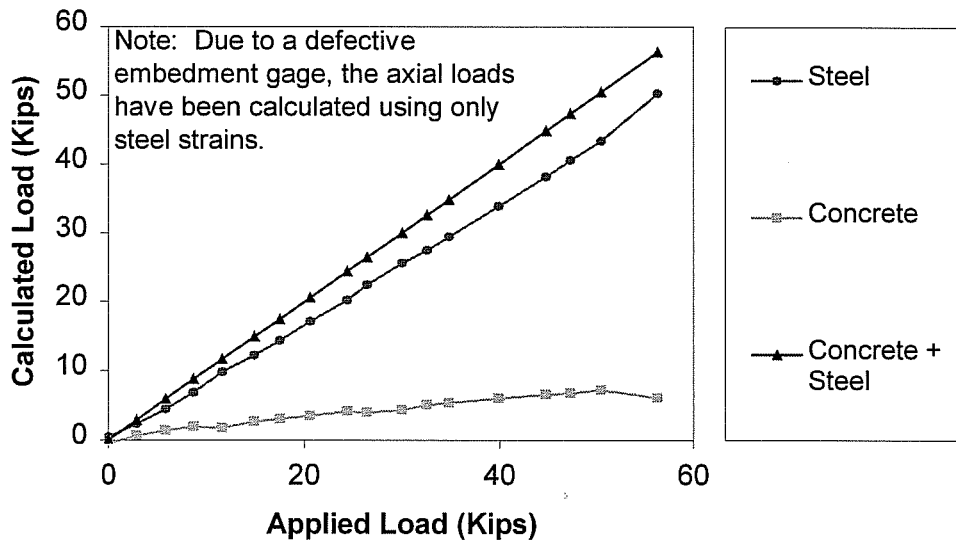


Figure A10. Axial load as calculated in CFT3 from strains at a cross-section located 42 inches from the concrete-loaded end.

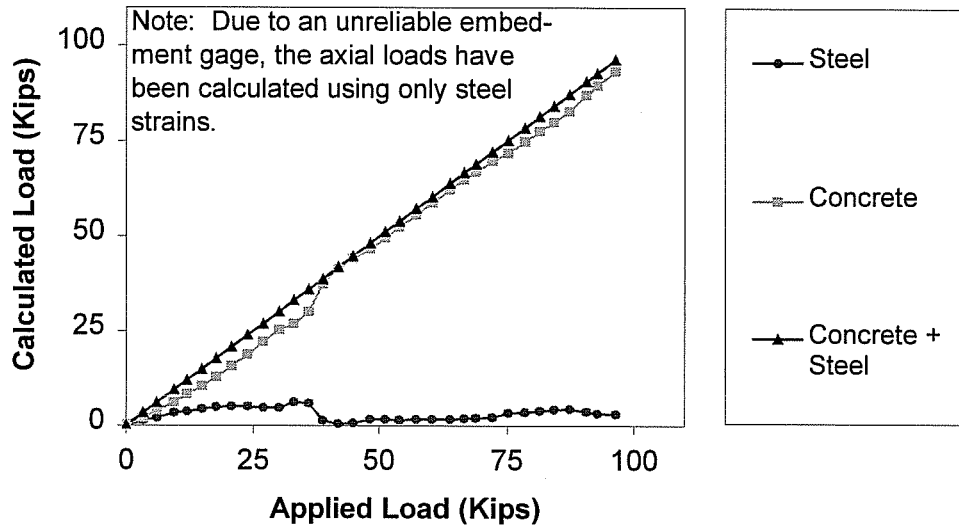


Figure A11. Axial load as calculated in CFT2 from strains at a cross-section located 6 inches from the concrete-loaded end.

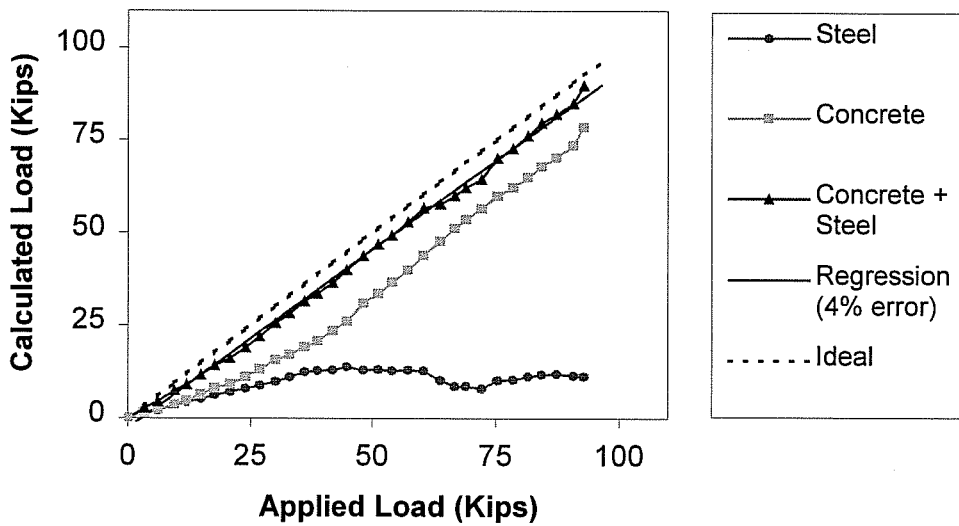


Figure A12. Axial load as calculated in CFT2 from strains at a cross-section located 12 inches from the concrete-loaded end.

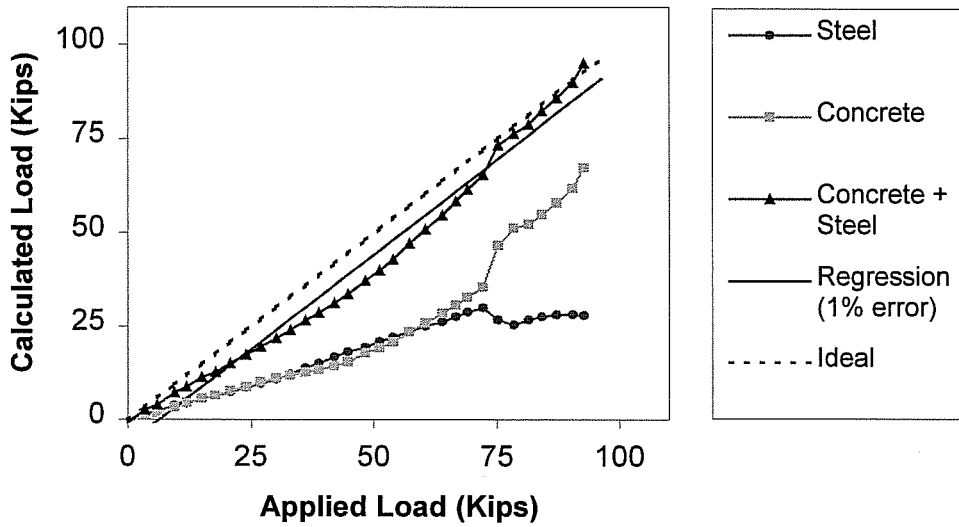


Figure A13. Axial load as calculated in CFT2 from strains at a cross-section located 24 inches from the concrete-loaded end.

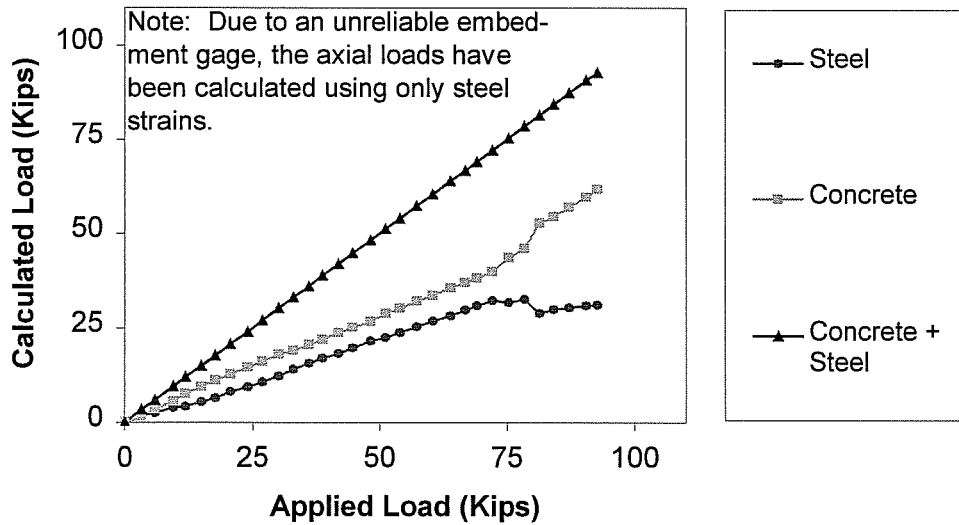


Figure A14. Axial load as calculated in CFT2 from strains at a cross-section located 36 inches from the concrete-loaded end.

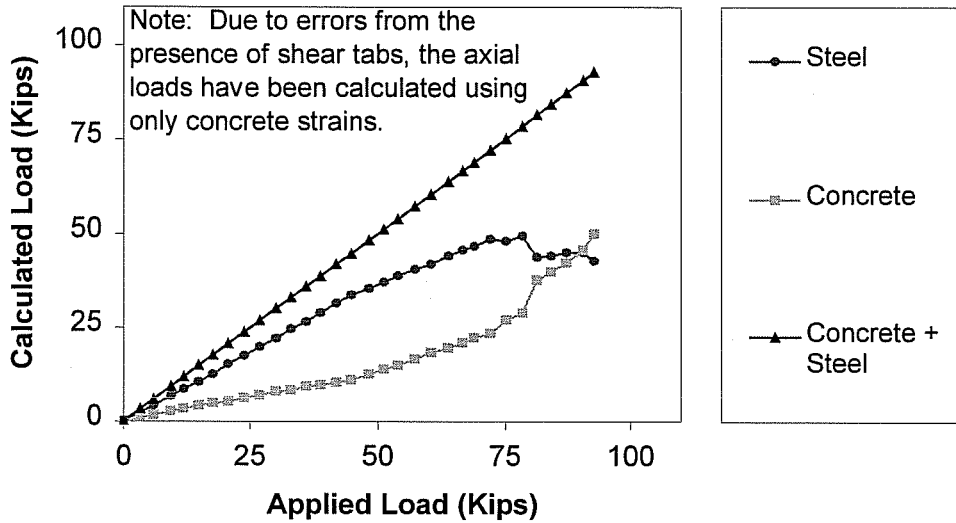


Figure A15. Axial load as calculated in CFT2 from strains at a cross-section located 42 inches from the concrete-loaded end.

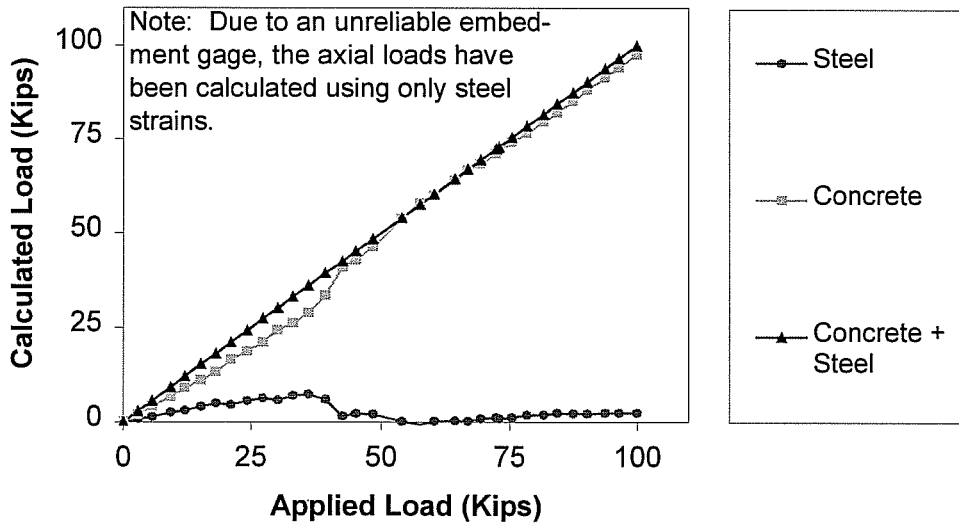


Figure A16. Axial load as calculated in CFT5 from strains at a cross-section located 6 inches from the concrete-loaded end.

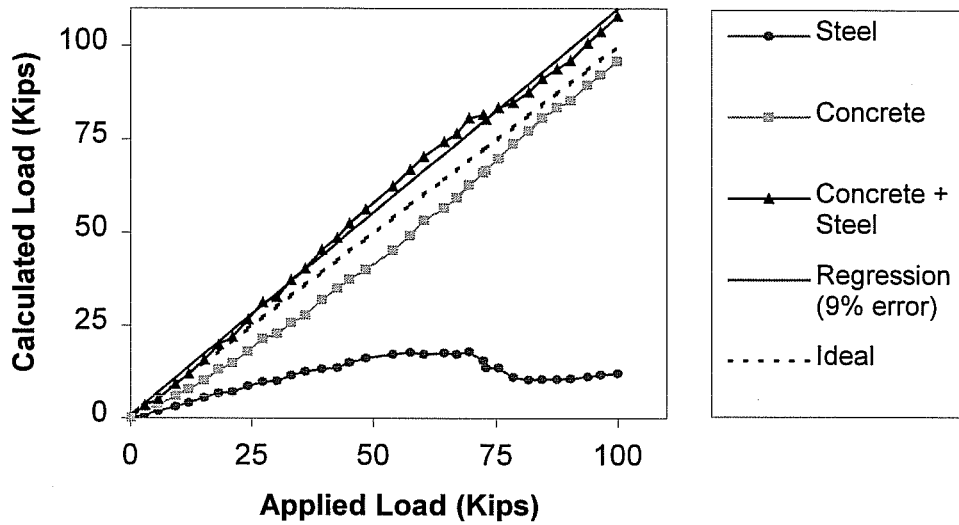


Figure A17. Axial load as calculated in CFT5 from strains at a cross-section located 12 inches from the concrete-loaded end.

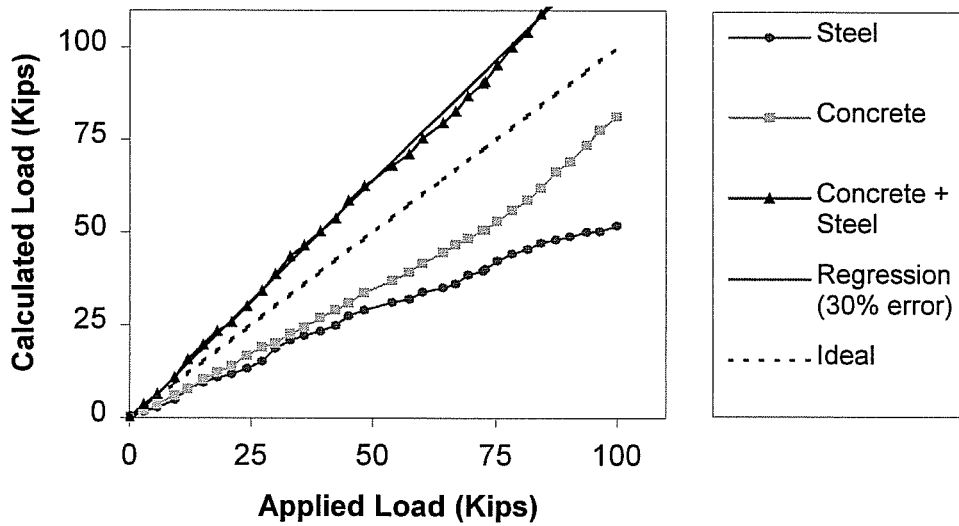


Figure A18. Axial load as calculated in CFT5 from strains at a cross-section located 24 inches from the concrete-loaded end.

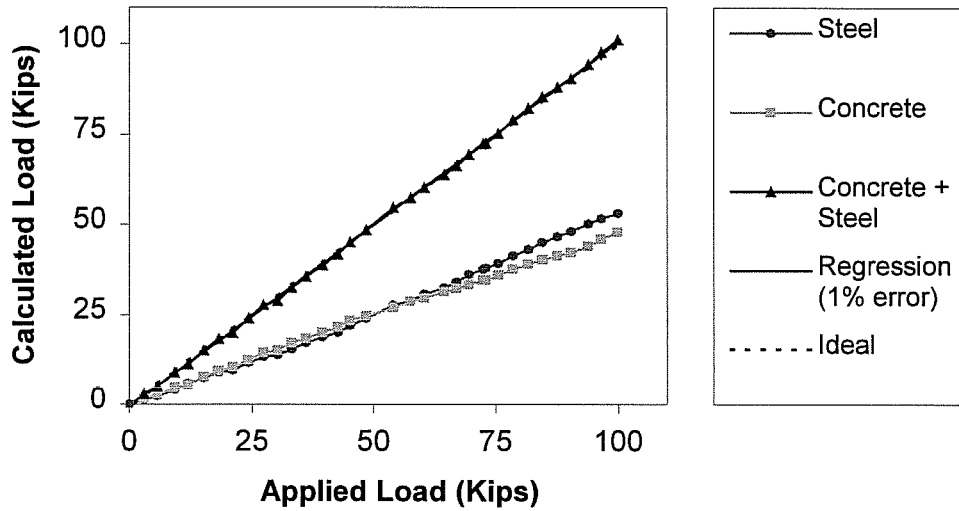


Figure A19. Axial load as calculated in CFT5 from strains at a cross-section located 36 inches from the concrete-loaded end.

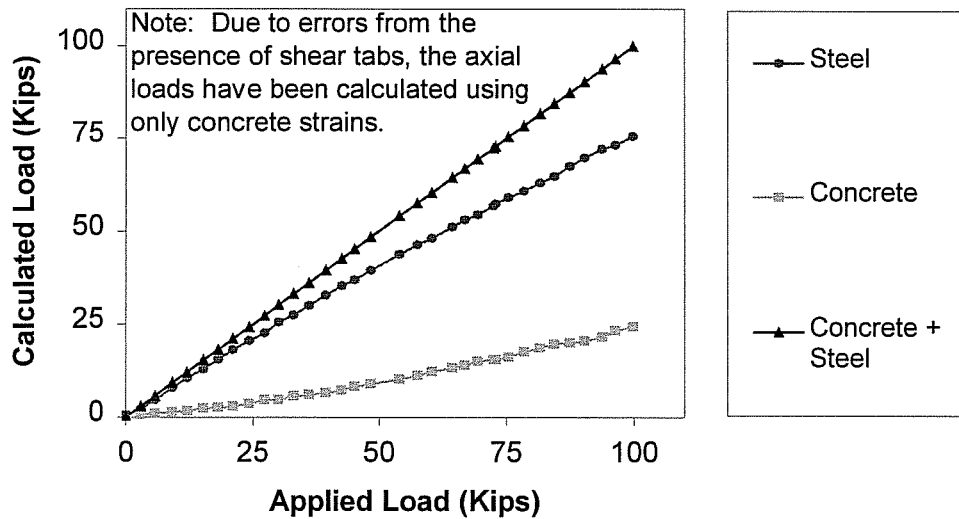


Figure A20. Axial load as calculated in CFT5 from strains at a cross-section located 42 inches from the concrete-loaded end.

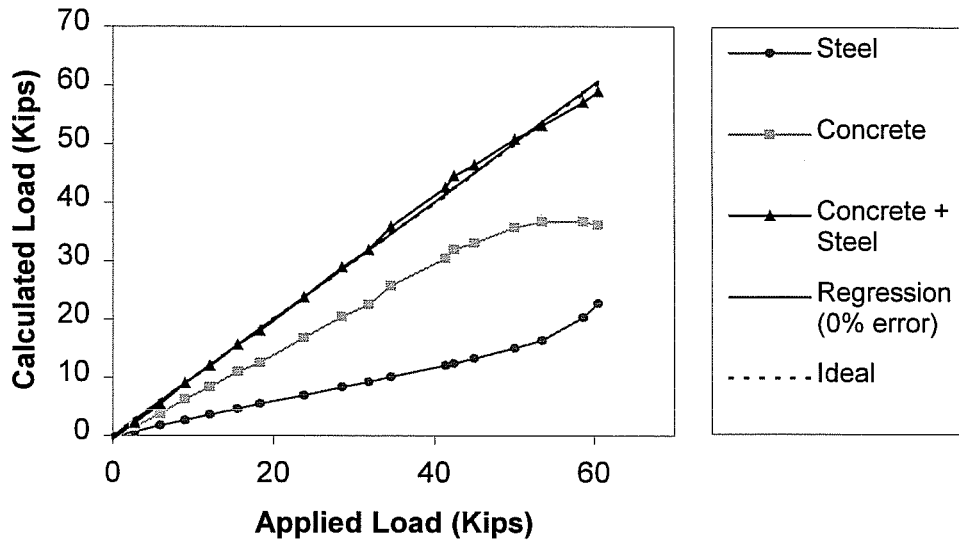


Figure A21. Axial load as calculated in CFT7 from strains at a cross-section located 7.5 inches from the concrete-loaded end.

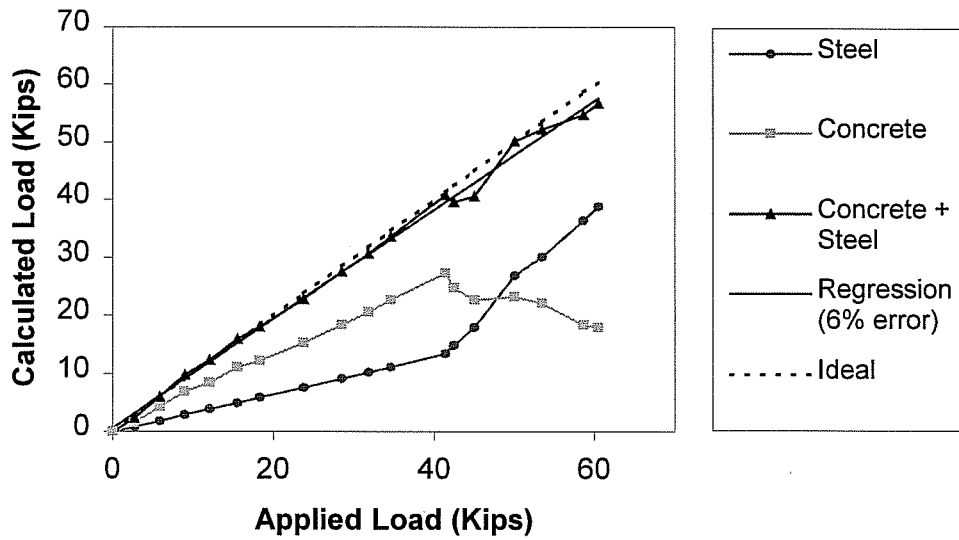


Figure A22. Axial load as calculated in CFT7 from strains at a cross-section located 15 inches from the concrete-loaded end.

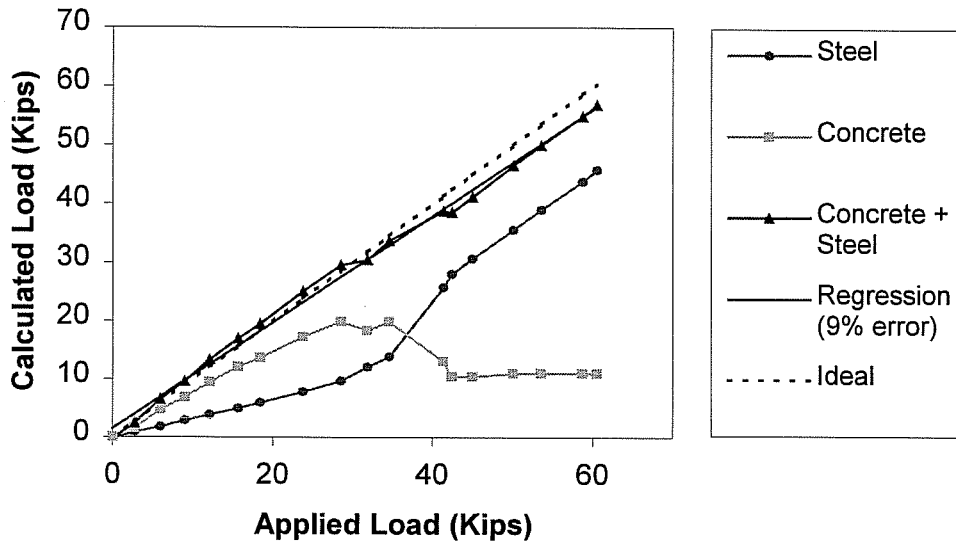


Figure A23. Axial load as calculated in CFT7 from strains at a cross-section located 30 inches from the concrete-loaded end.

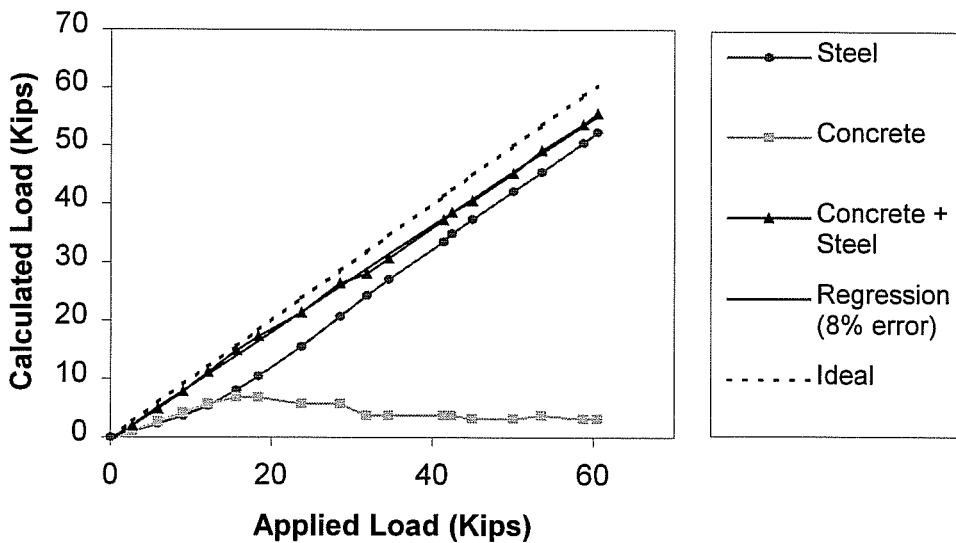


Figure A24. Axial load as calculated in CFT7 from strains at a cross-section located 45 inches from the concrete-loaded end.

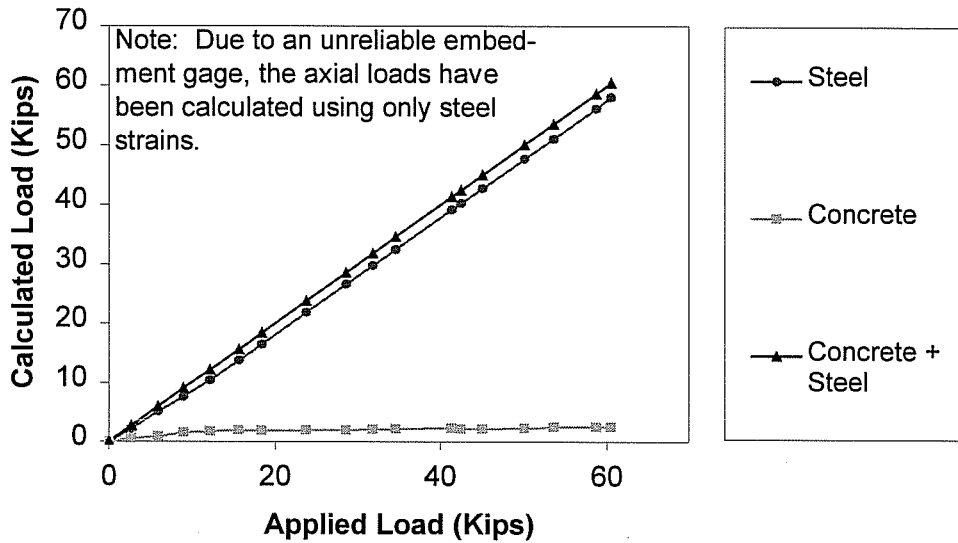


Figure A25. Axial load as calculated in CFT7 from strains at a cross-section located 52.5 inches from the concrete-loaded end.

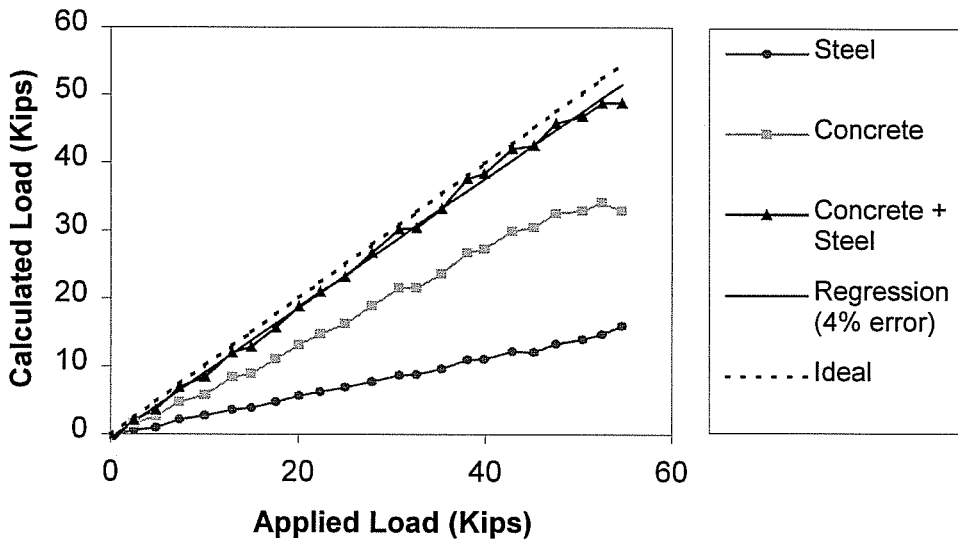


Figure A26. Axial load as calculated in CFT1 from strains at a cross-section located 7.5 inches from the concrete-loaded end.

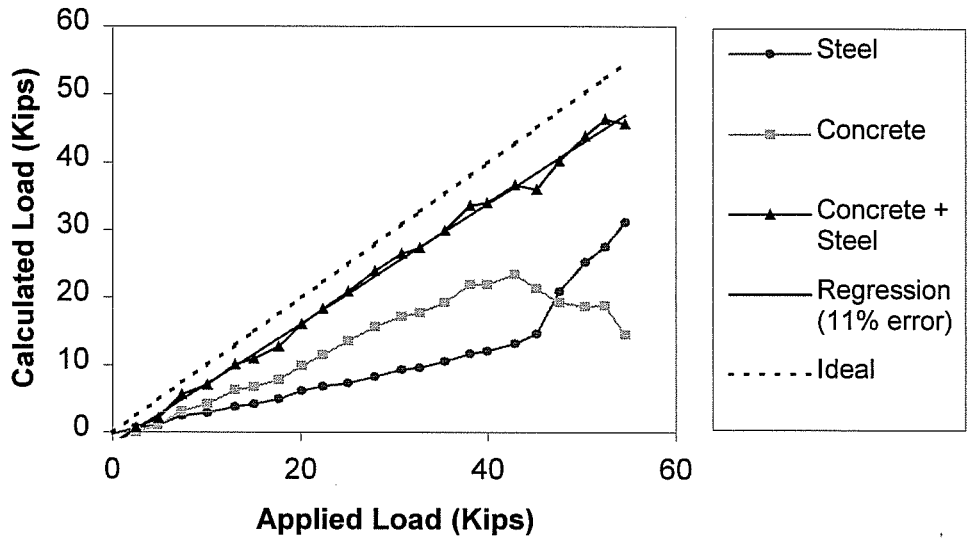


Figure A27. Axial load as calculated in CFT1 from strains at a cross-section located 15 inches from the concrete-loaded end.

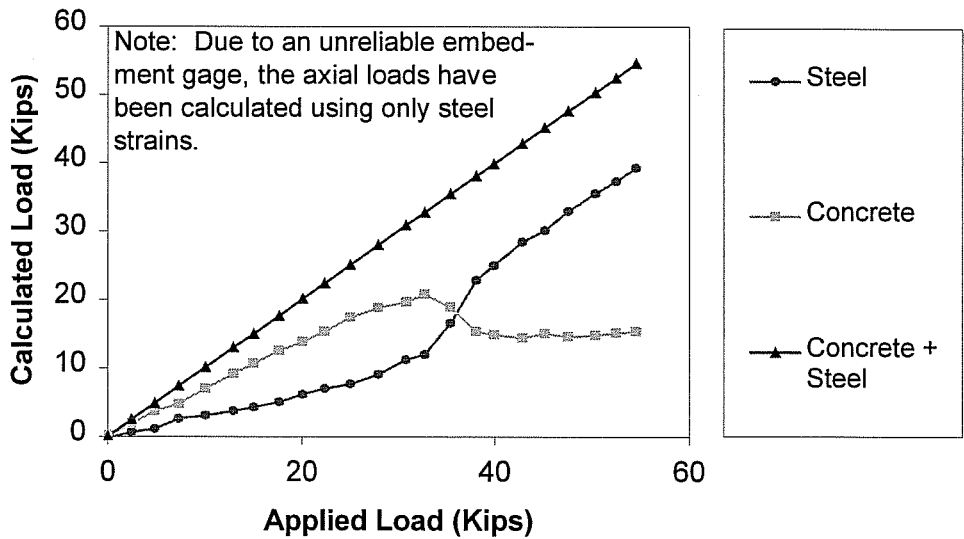


Figure A28. Axial load as calculated in CFT1 from strains at a cross-section located 30 inches from the concrete-loaded end.

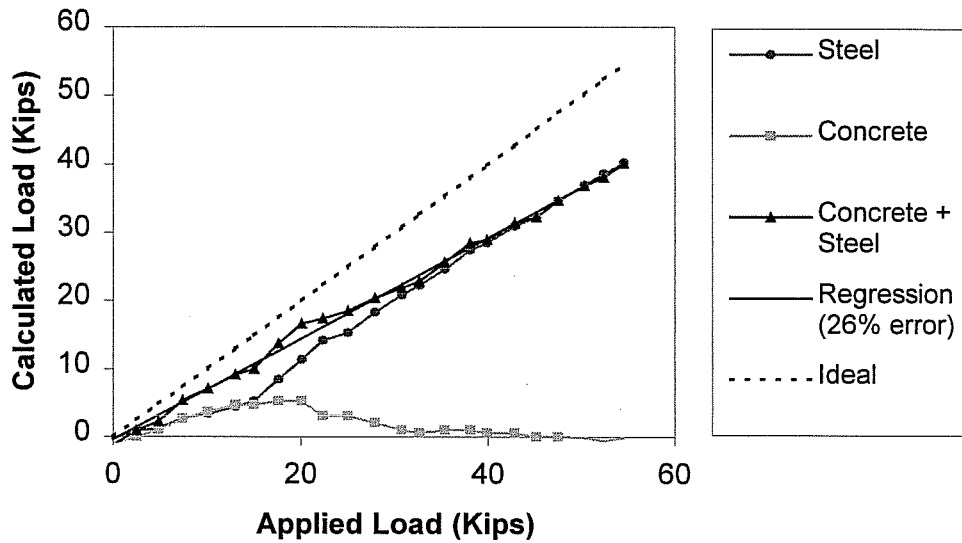


Figure A29. Axial load as calculated in CFT1 from strains at a cross-section located 45 inches from the concrete-loaded end.

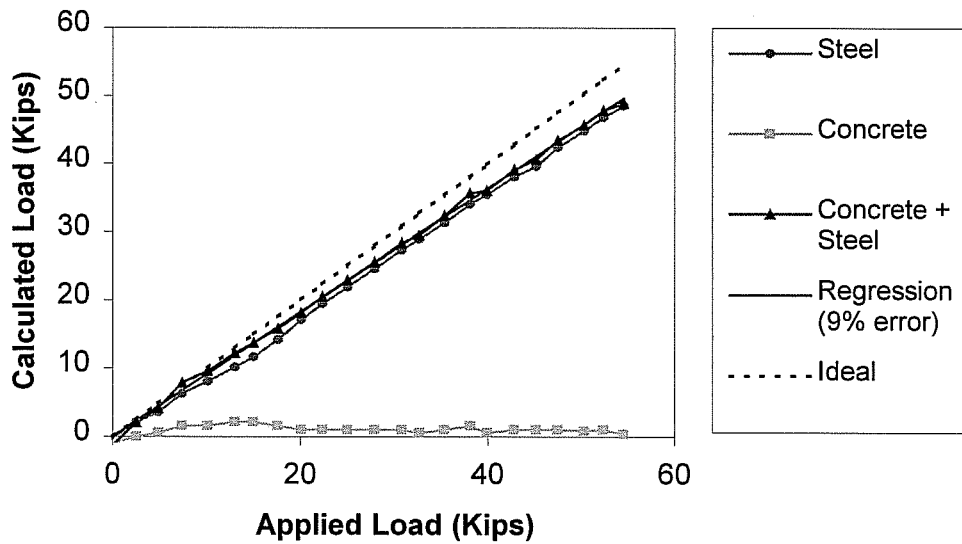


Figure A30. Axial load as calculated in CFT1 from strains at a cross-section located 52.5 inches from the concrete-loaded end.

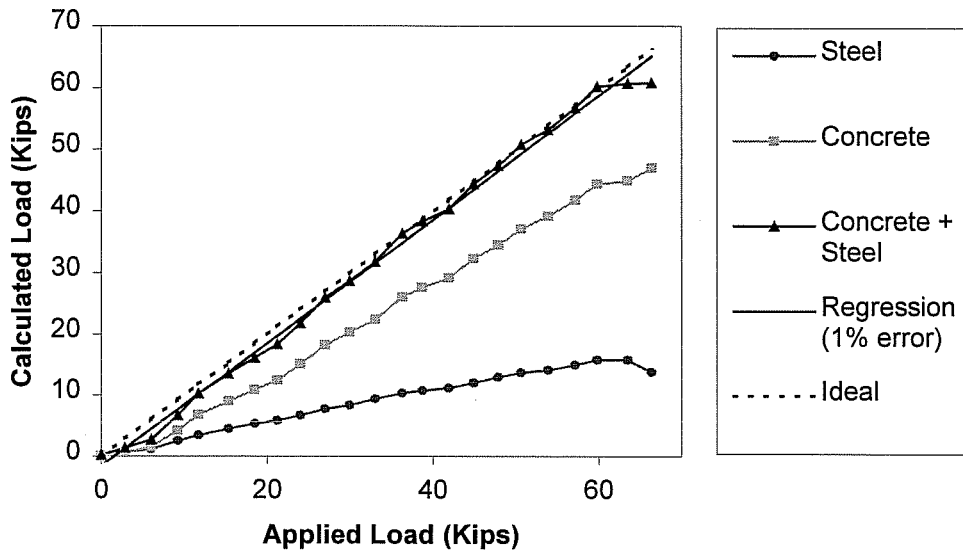


Figure A31. Axial load as calculated in CFT8 from strains at a cross-section located 7.5 inches from the concrete-loaded end.

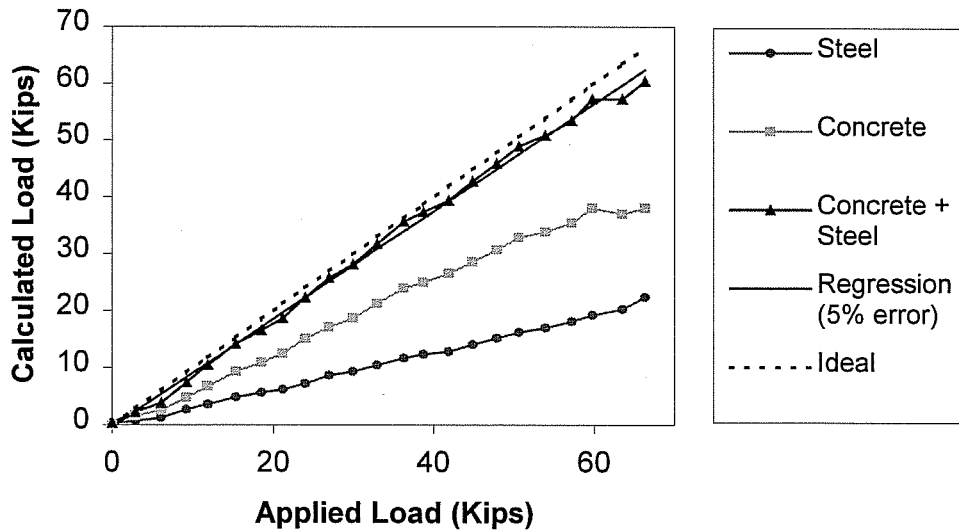


Figure A32. Axial load as calculated in CFT8 from strains at a cross-section located 15 inches from the concrete-loaded end.

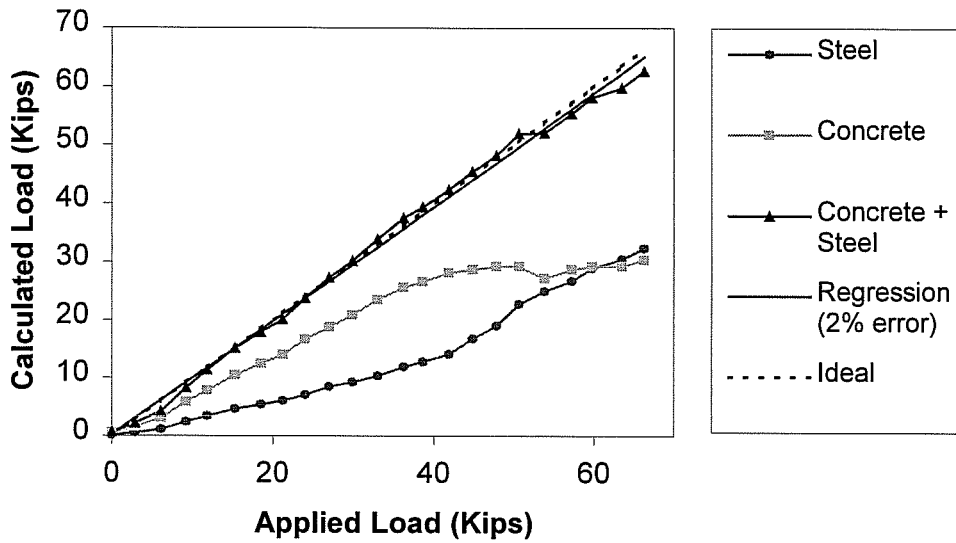


Figure A33. Axial load as calculated in CFT8 from strains at a cross-section located 30 inches from the concrete-loaded end.

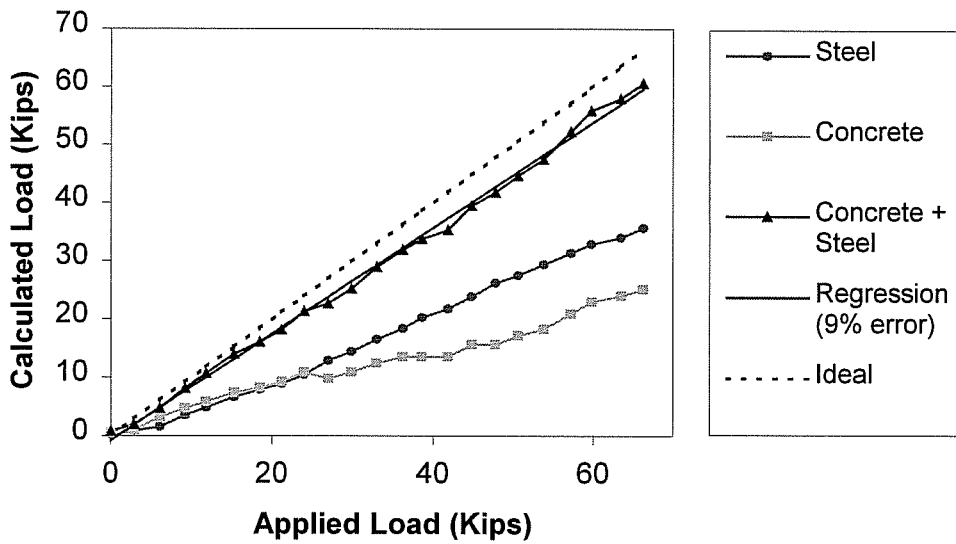


Figure A34. Axial load as calculated in CFT8 from strains at a cross-section located 45 inches from the concrete-loaded end.

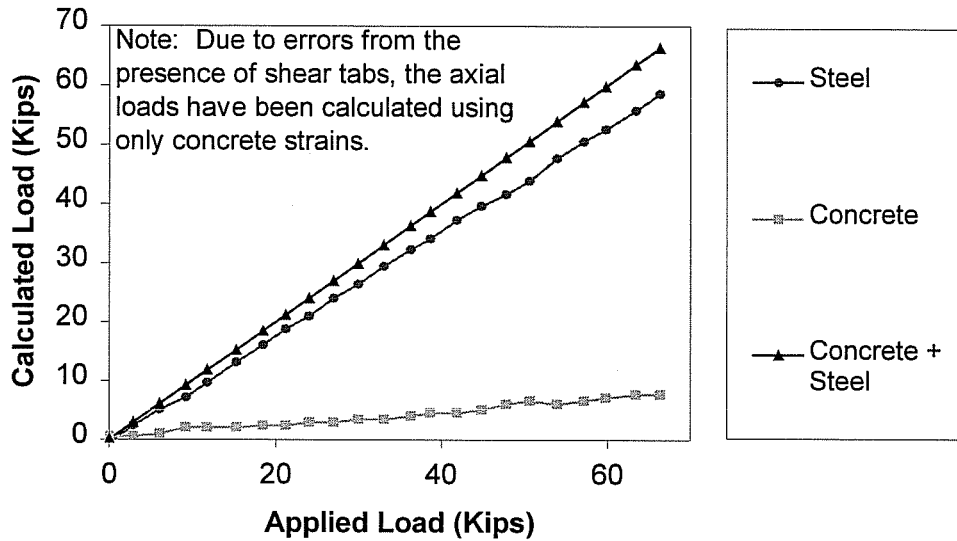


Figure A35. Axial load as calculated in CFT8 from strains at a cross-section located 52.5 inches from the concrete-loaded end.

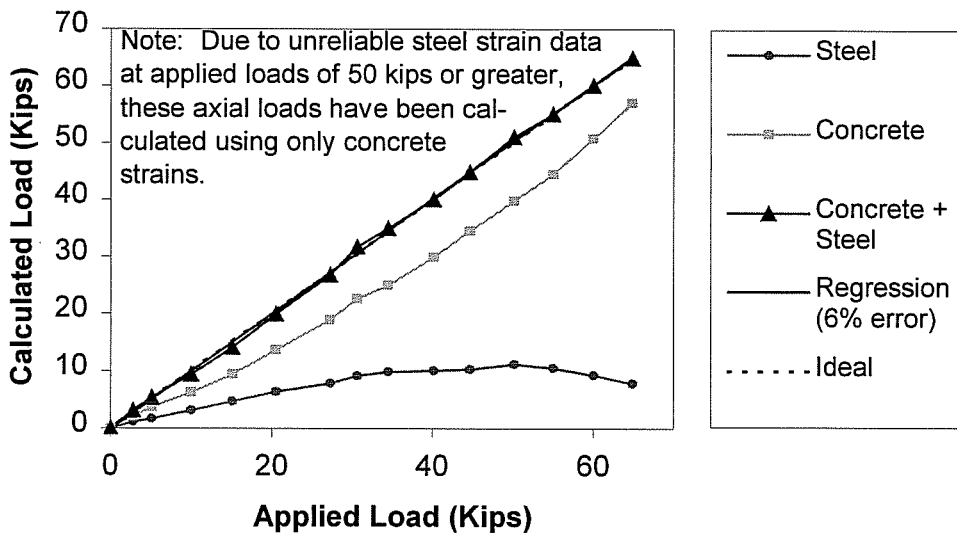


Figure A36. Axial load as calculated in CFT6 from strains at a cross-section located 7.5 inches from the concrete-loaded end.

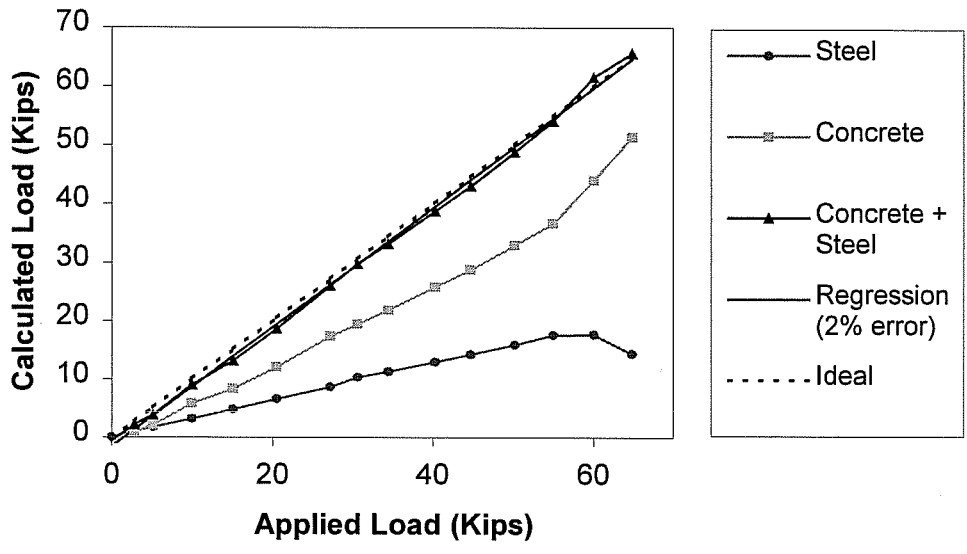


Figure A37. Axial load as calculated in CFT6 from strains at a cross-section located 15 inches from the concrete-loaded end.

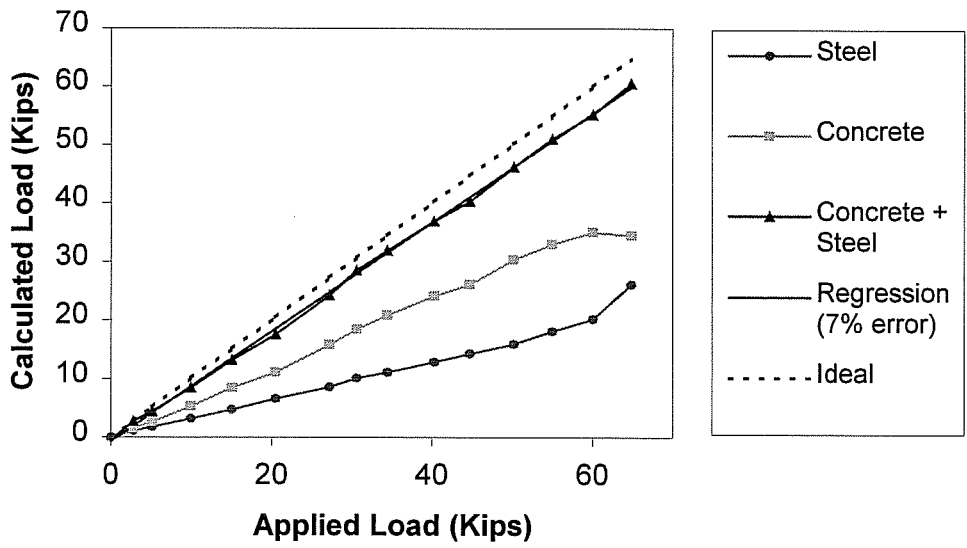


Figure A38. Axial load as calculated in CFT6 from strains at a cross-section located 30 inches from the concrete-loaded end.

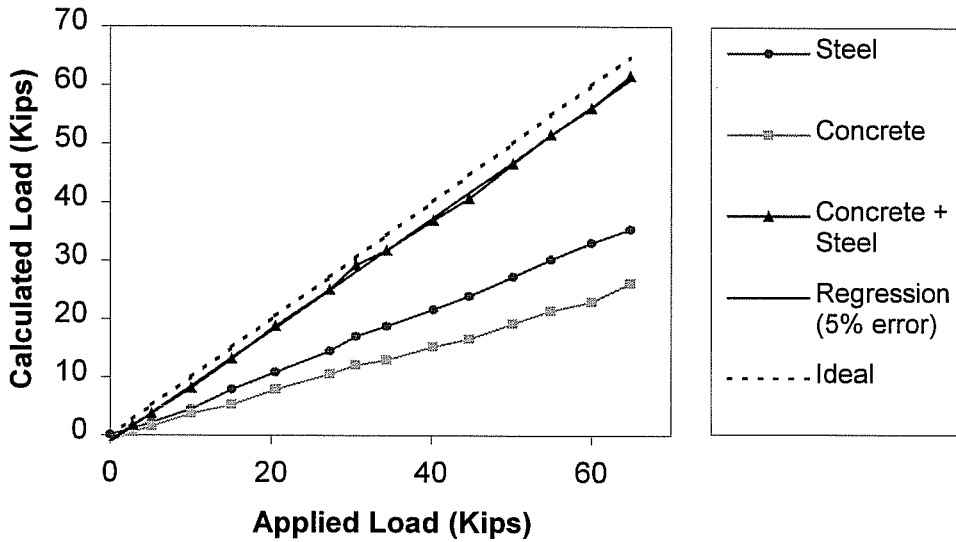


Figure A39. Axial load as calculated in CFT6 from strains at a cross-section located 45 inches from the concrete-loaded end.

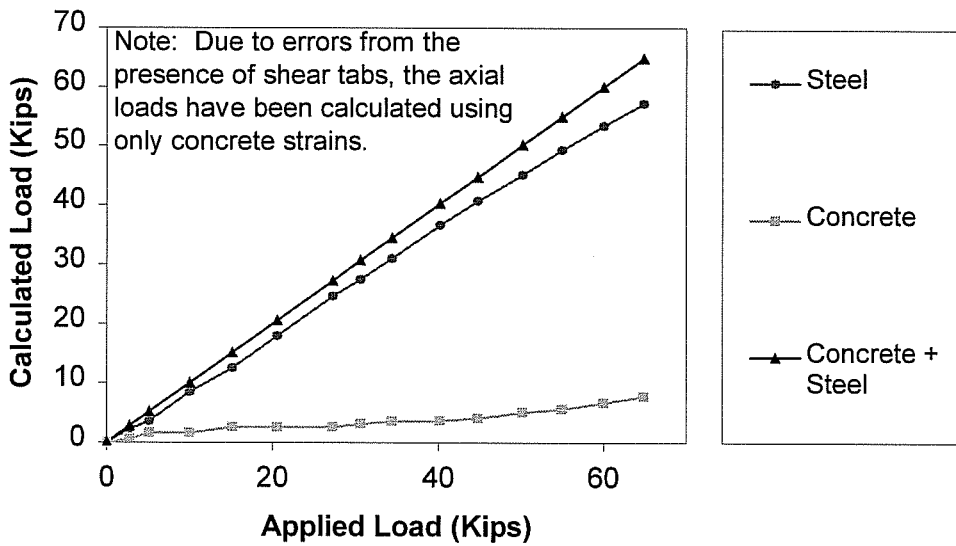


Figure A40. Axial load as calculated in CFT6 from strains at a cross-section located 52.5 inches from the concrete-loaded end.

BIBLIOGRAPHY

- ACI Committee 318. 1995. *Building code requirements for structural concrete and commentary*. Farmington Hills, Mich.: ACI.
- ACI Committee 408. 1966. Bond stress – The state of the art. *ACI J, Proceedings* 63 (11): 1161-88.
- AISC. 1993. *Load and Resistance Factor Design Specification for Structural Steel Buildings*. Chicago: AISC.
- Astaneh, Abolhassan, Steven M. Call, and Kurt M. McMullin. 1989. Design of single plate shear connections. *AISC Engineering Journal*, First Quarter: 21-32.
- Billington, Colin J., and Gael H. G. Lewis. 1978. The strength of large diameter grouted connections. *Proceedings of the Tenth Annual Offshore Technology Conference*. Houston, TX.
- Cai, Shao-Huai. 1988. Ultimate strength of concrete-filled tube columns. In *Composite construction in steel and concrete: Proceedings of an Engineering Foundation conference*, edited by C. Dale Buckner and Ivan M. Viest. New York: ASCE.
- Furlong, Richard W. 1967. Strength of steel-encased concrete beam columns. *J. Struct. Div.*, ASCE, 93 (ST5): 113-24.
- Gardner, Noel J., and E. Ronald Jacobson. 1967. Structural behavior of concrete filled steel tubes. *ACI J, Proceedings* 64 (7): 404-13.
- Goel, S. C., and H. Yamanouchi, eds. 1993. Proceedings of the 1992 U.S.-Japan Workshop on composite and hybrid structures. *Research Report*. Dept. of Civil and Envir. Engrg., Univ. of Michigan, Ann Arbor, Mich.
- Hajjar, Jerome F., and Brett C. Gourley. 1996. Representations of concrete-filled steel tube cross-section strength. *J. Struct. Engrg.*, ASCE, 122 (11): 1327-36.
- Iyengar, H. S. 1977. State-of-the-art report on composite or mixed steel-concrete construction for buildings. New York: ASCE.

- Klöppel, Von K., and W. Goder. 1957. Collapse load tests on concrete-filled steel tubes and establishment of a design formula. *Der Stahlbau* (Berlin) 26 (1): 1-10.
Quoted in Noel J. Gardner and E. Ronald Jacobson, 1967, Structural behavior of concrete filled steel tubes, *ACI J., Proceedings* 64 (7): 404-13.
- Knowles, Robert B., and Robert Park. 1969. Strength of concrete filled steel tubular columns. *J. Struct. Div., ASCE*, 95 (ST12): 2565-87.
- Lamport, William Bruce. 1988. Ultimate strength of grouted pile-to-sleeve connections. Ph.D. diss., Univ. of Texas, Austin.
- Mains, R. M. 1951. Measurement of the distribution of tensile and bond stresses along reinforcing bars. *J. ACI, Proceedings* 48 (3): 225-52.
- Neogi, P. K., H. K. Sen, and J. C. Chapman. 1969. Concrete-filled tubular steel columns under eccentric loading. *The Struct. Engr.* 47 (5): 187-95.
- Rabbat, B. G., and H. G. Russell. 1985. Friction coefficient of steel on concrete or grout. *J. Struct. Engrg* 111 (3): 505-15.
- Shakir-Khalil, H. 1993a. Pushout strength of concrete-filled steel hollow sections. *The Struct. Engr.* 71 (13): 230-33, 243.
- Shakir-Khalil, H. 1993b. Resistance of concrete-filled steel tubes to pushout forces. *The Struct. Engr.* 71 (13): 234-43.
- Viest, Ivan M., Joseph P. Colaco, Richard W. Furlong, Lawrence G. Griffis, Roberto T. Leon, and Loring A. Wyllie, Jr., eds. 1997. *Composite construction design for buildings*. New York: McGraw-Hill.
- Virdi, K. S., and P. J. Dowling. 1980. Bond strength in concrete filled steel tubes. *IABSE Periodica* 3/1980, *Proceedings P-33/80* 125-39.
- Zhong Shan-Tong and Miao Ruo-Yu. 1988. Stress-strain relationship and strength of concrete filled tubes. In *Composite construction in steel and concrete: Proceedings of an Engineering Foundation conference*, edited by C. Dale Buckner and Ivan M. Viest. New York: ASCE.

VITA

Michelle A. Parsley was born in Louisville, Kentucky, on April 2, 1973. She is the daughter of Archie Edward Parsley, Jr., and Mary Kathleen Yates Parsley. Michelle graduated from Sacred Heart Academy, Louisville, Kentucky, in 1991, and was a 1990 Kentucky Governor's Scholar. In 1991, she entered Washington University in St. Louis, Missouri. During the summers of 1994 and 1995, she was employed by Mobil Technology Company in Dallas, Texas. Michelle graduated summa cum laude with a Bachelor of Science degree in Civil Engineering from Washington University in May, 1995. In the fall of 1995, she entered The Graduate School at The University of Texas with support from a fellowship sponsored by the U. S. Department of Defense.

Permanent Address: 7012 Breakwater Place
Prospect, Kentucky 40059

This thesis was typed by the author.